Design of a stress-dependent deep-level transient spectroscopy instrument for the study of the structural properties of defects in semiconductors

by

Kian Ostvar

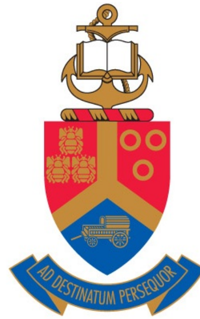

Submitted in partial fulfilment of the requirements for the degree

Master of Science

in

FACULTY OF NATURAL AND AGRICULTURAL SCIENCES

UNIVERSITY OF PRETORIA

February 2019

Supervisor : Professor W E Meyer
Co-Supervisor : Professor F D Auret

Declaration of Authorship

I, Kian Ostvar, declare that this thesis titled, 'Design of a stress-dependent deep-level transient spectroscopy instrument for the study of the structural properties of defects in semiconductors' and the work presented in it are my own. I confirm that:

- This work was done wholly or mainly while in candidature for a research degree at this University.
- Where any part of this thesis has previously been submitted for a degree or any other qualification at this University or any other institution, this has been clearly stated.
- Where I have consulted the published work of others, this is always clearly attributed.
- Where I have quoted from the work of others, the source is always given. With the exception of such quotations, this thesis is entirely my own work.
- I have acknowledged all main sources of help.
- Where the thesis is based on work done by myself jointly with others, I have made clear exactly what was done by others and what I have contributed myself.

Signed: ________________________________

Date: ________________________________

"It is paradoxical, yet true, to say, that the more we know, the more ignorant we become in the absolute sense, for it is only through enlightenment that we become conscious of our limitations. Precisely one of the most gratifying results of intellectual evolution is the continuous opening up of new and greater prospects. "

Nikola Tesla

Design of a stress-dependent deep-level transient spectroscopy instrument for the study of the structural properties of defects in semiconductors

By

Kian Ostvar

submitted in partial fulfilment of the requirements for the degree

Master of Science

in

FACULTY OF NATURAL AND AGRICULTURAL SCIENCES

UNIVERSITY OF PRETORIA

Abstract

Defects in semiconductors have been studied extensively over the past few decades. The advent of highly sensitive techniques such as deep-level transient spectroscopy (DLTS) and Laplace DLTS (LDLTS) has resulted in more accurate measurements of the electrical properties of defects, as well as contributed towards identification of new ones. However, the bulk of the research efforts on this topic is concentrated on the electrical properties and not the physical structure of defects. While numerous characterization techniques, such as EPR and IR spectroscopy can be used to study the structure of defects, application of uniaxial stress with DLTS has been shown to be a superior technique with regards to determining the symmetry of defects observed by DLTS. However, in practice, it is a difficult and time consuming technique to perform, and therefore is not a popular research tool. There are

only a few such systems that are operational in the world. The difficulties arise from preparation and mounting of the samples as well as stability of the system and survival of the samples during and after each measurement.

The aim of this work is to undertake the design of a stress-dependent LDLTS system that is user friendly and can provide reproducible results. The speed with which samples can be mounted and dismounted was another point of interest during the design process and the higher resolution of LDLTS compared to conventional DLTS makes it possible to perform measurements with lower amounts of pressure, thus increasing the survive ability of the samples.

Furthermore, proper functioning of the system was investigated by attempting to reproduce a stress-dependent study on the E2 defect in GaAs that was done using a similar instrument that utilized a conventional DLTS system. The results clearly confirm the superiority of LDLTS for this type of measurements. Where in the previous study only a broadening of the DLTS peak is observed under 0.4 GPa, in our measurements there is a clear splitting of the emission rate spectrum from one into two separate components when stressed along the (110) axis at only 0.18 GPa and the results numerically agree with the aforementioned study. The most important shortcoming of the system is temperature stability at low temperatures.

Acknowledgements

I would like to acknowledge my indebtedness and render my warmest thanks to my supervisor, Professor Walter E. Meyer, who made this work possible. His friendly guidance, constant encouragement and expert advice have been invaluable throughout all stages of the work.

I would also wish to express my gratitude to my co-supervisor, Professor F. Danie Auret for patiently sharing his knowledge and extensive experience with me through discussions and valuable suggestions which have contributed greatly to the completion and improvement of the thesis.

My heartfelt gratitude goes to Dr. Matshisa Legodi and Mr. Johan Janse van Rensburg for their contributions towards design, building and improvements of the principal instrument presented in this thesis, as well as their role in providing technical expertise with regards to sourcing and familiarizing me with lab equipment and proper procedures.

I am grateful to Mr. Danie Joubert for his expert craftsmanship and advice during the design and build portion of this thesis.

I would also like to give thanks to my dear colleagues, Ms. Helga danga, Mr. Shandirai Tunhuma, Dr. Phuti Ngoepe, Dr. Ezekiel Omotoso, Mr. Louwrens van Schalkwyk, Dr. Sergio Coelho, Mr. Meehleketo Mayimele, Dr. Emmanuel Igumbor, Dr. Damilola Momodu, Dr. Abdulhakeem Bello and especially, Mr. Abraham Willem Barnard for their invaluable scientific advice and support as well as their radiant motivation and enthusiasm in research which has taught me a lot.

Special thanks are due to my lovely fiance, Fatemeh (Mina) Taghizadeh for her continuous support, love, encouragement and understanding as well as her patience! My thanks are extended to her father, Hadi, her mother, Rana and her sister Sepi whose kindness knows no bounds.

I would like to specially thank my friends: Dr. Farshad Barzegar, Dr. Mohammad Moghimi Ardekani, Miss Sharifeh Vatannia and Miss Mahboubeh Fathi Kenari for their continuous support and encouragements.

Last but not least, my humblest gratitude goes to my dear parents, Golrokh and Nader and my brother, Sassan who supported and believed in me in endless ways.

Contents

Declaration of Authorship i

Abstract iii

Acknowledgements v

Contents vii

List of Figures ix

List of Tables xiii

Abbreviations xiv

Physical Constants xv

Symbols xvi

1 Introduction 1

2 Semiconductors 7
- 2.1 Theory of solids . . . 8
  - 2.1.1 Semiconductors . . . 16
  - 2.1.2 Semiconductor defects . . . 19
  - 2.1.3 Gallium arsenide . . . 24
  - 2.1.4 The E2 defect in GaAs . . . 25
- 2.2 Electronic devices . . . 28
  - 2.2.1 Metal-semiconductor junction . . . 29
- 2.3 Deep level transient spectroscopy (DLTS) . . . 34
  - 2.3.1 Laplace DLTS . . . 38
- 2.4 Integration of uniaxial stress into Laplace DLTS . . . 40
  - 2.4.1 Determination of symmetry . . . 44

3 Design of the stress-dependent DLTS system 50
3.1 Laplace DLTS setup . . . 53
3.1.1 Hardware . . . 53
3.1.2 Software . . . 60
3.2 Apparatus and setup . . . 61
3.2.1 The probe . . . 61
3.2.2 Stress applying module . . . 68

4 Experimental methods 77
4.1 Metal-semiconductor device fabrication . . . 77
4.1.1 Preparing the substrate . . . 78
4.1.2 Cleaning procedure . . . 79
4.1.3 Schottky and ohmic contacts . . . 80
4.2 Defect introduction by beta particles . . . 82
4.3 Characterization techniques . . . 82
4.3.1 IV/CV measurements . . . 82
4.3.2 DLTS measurements . . . 83
4.3.2.1 Determining the presence of the E2 defect using conventional DLTS . . . 84
4.3.2.2 Electrical characterization of the E2 defect using Laplace DLTS . . . 85
4.4 Uniaxial-stress dependent DLTS . . . 87

5 Results and discussions 90
5.1 I-V and C-V . . . 91
5.2 Activation energy . . . 93
5.3 Electric field dependence . . . 96
5.4 Uniaxial-stress measurements . . . 97
5.4.1 Arrhenius plots . . . 102
5.4.2 Discussion . . . 106
5.4.3 Activation energies and capture cross sections . . . 107
5.5 Shortcomings and sources of error . . . 112
5.5.1 Sources of error . . . 112
5.5.2 Shortcomings . . . 116

6 Summary and conclusions 118
6.1 Future work . . . 120

Bibliography 122

List of Figures

2.1 The Difference between the atomic structure of two arbitrary crystalline (a) and amorphous (b) solids. 9
2.2 A 2D illustration of a crystal lattice. 10
2.3 Various Bravais lattices. Image reproduced under the GNU Free Documentation License from Wikipedia.org 11
2.4 Diamond and Zinc blende lattices 12
2.5 Crystal planes and their associated Miller indices. 13
2.6 Plot of potential energy as a function of wave vector k for an arbitrary crystal lattice (After Kittel (2004)) 15
2.7 Energy band configuration of Insulators, Semiconductors, and conductors at 0 K 16
2.8 Temperature dependence of intrinsic carrier concentration in Si, Ge and GaAs. After Streetman (1994). 17
2.9 Carrier concentration dependence on temperature for n-type and p-type GaAs. After Grove (1967) 18
2.10 Direct and indirect carrier transport between the conduction and the valence bands 20
2.11 Shallow-level and deep level defects in n-type GaAs 21
2.12 Generation-Recombination and Trapping events in semiconductors. In the figure: n refers to electrons while P refers to holes. C_n and C_P refer to capture events, e_n and e_p are emission events and P_T and n_T refer to trapped charged carriers. 22
2.13 A GaAs unit cell. It consists of two inter-penetrating FCC structures that form a zinc-blende lattice. Image used under the Public domain license from Wikipedia.org 24
2.14 Conventional DLTS sccan showing broadening of the E2 peak under uniaxial stress along (110) orientation (Hartnett and Palmer, 1997). The Image was reproduced from hard copy version. 27
2.15 Metal-Semiconductor Contacts. After Schroder (2006). 30
2.16 Schematic illustration of the DLTS cycle. After Miller et al. (1977). 37
2.17 LDLTS spectra of VOH(2/0) defect at 160 K measured both at zero stress and under uniaxial stress along the three major crystallographic directions. From the splitting pattern, symmetry of the defect was determined to be orthorhombic-I, C-2v. After Coutinho et al. (2003). 44

3.1 The OptistatDN from Oxford Instruments Inc. 54

3.2 Boonton 7200 capacitance meter 55
3.3 Lakeshore 336 temperature controller 56
3.4 Model DP25B-S DIN process meter controller (left) and Model LMC302-2K force meter (right). Images taken from Omega Engineering Inc. (LMC320 and DP25B-S) 58
3.5 Various parts of the DAQ system: a) the NI PCI 6251, b) the GPIB-USB and c) the connector block. 59
3.6 Various components of the stress probe: a) Force sensor housing. b) Bellows. c) Connector block. d) Body of the probe. e) sample holder housing. f) Anvil. g) Hammer (electrical components are not shown). 62
3.7 Sample holder. a) Nuts. b) Hammer. c) guide rods. d) Sample. e) Anvil. 63
3.8 Sample holder enclosure. a) Body of the enclosure. b) heater wires. c) Thermocouple wires. d) Coaxial wires. e) Heater strip. 64
3.9 A demonstration of how samples are mounted into the sample holder and electrical connections are made. 65
3.10 neck of the probe. a) Stainless steel rod. b) Hollow tube. c) Grooves where wires are fitted. d) Hammer. e) Sample. f) Anvil. 66
3.11 Connector housing. a) BNC connector. b) Blank QF flange converted to house the BNC connectors. c-d) O-ring. e) circular MIL-DTL-5015 connector. 67
3.12 a) Force sensor housing. b)Bellows. c) Stainless steel rod. d) O-ring. e) connector block. 68
3.13 Stress module components. a) steel disk. b) Spring. c) Pusher. d) Spring enclosure. e) QF flange. f) Hydraulic cylinder. 70
3.14 A representaiton of how a sample looks after the wire bonding process. 71
3.15 QF or KF clamp. 73
3.16 The special clamp that connects the probe to the stress module. . . 74
3.17 Stand. a) Threaded rod and nuts for adjusting the height of the hydraulic cylinder. b) special holder for holding both the hydraulic cylinder and the spring housing. c) Steel rod for holding liquid nitrogen reservoir. d) steel block for attaching the threaded rod to the frame. e) steel rod for attaching extra utilities. f) steel beams forming the frame. 75
3.18 Complete mechanical components of the system. a) liquid nitrogen reservoir. b) Hydraulic hand pump. 76

4.1 A wafer with (100) surface orientation. The lines in the figure indicate cleavage lines a), cross sectional view of the wafer showing the (100) and (110) planes b). 79
4.2 Cross sectional view of the Schottky and ohmic contacts on a GaAs substrate. The thicknesses of the contacts are exaggerated. 81

4.3 Representation of the sample and how it is set up in the I-V/C-V station, showing the the probes (a), the Schottky contact (b), the substrate (c), the ohmic contact (d), conductive surface (e), the Vacuum pump intake (f). The purpose of the vacuum pump is to secure the sample in place while the probe is being connected to the Schottky contact. 83
4.4 Schematic diagram of a DLTS system. 84
4.5 Electric field dependence of the E2 defect in GaAs. The rightwards shift and the broadening of the peaks as a function of the magnitude of the electric field. Measurement conditions: T = 270 K, second pulse bias = −0.2 V, first and second pulse widths = 1 ms, sampling rate = 91 kHz, number of samples = 4000, number of scans = 6000. 86
4.6 Demonstration of the wire bonding process. 88

5.1 The C-V graphs of the SBD. 92
5.2 The I-V graphs of the SBD. 93
5.3 A conventional DLTS scan showing the dominant electron traps in the sample. The sample was irradiated for 3.5 hours with MeV electrons. Measurements were performed in the reference DLTS system that utilizes a helium-cooled cryostat. Measurement conditions: $V_R = -2$ V. First pulse bias = −0.5 V. Rate window = 80 s^{-1}. First and second pulse width = 1 ms. The inset graph illustrates the spectrum prior to irradiation. Note that the scale for the amplitude of the inset graph is selected to be between -0.01 pF and 0.01 pF. 94
5.4 Arrhenius plot for the E2 defect. These measurements were performed in the reference DLTS system. LDLTS measurement conditions: $T = 77 \pm 1$ K, $V_R = -2$ V, first pulse bias = −0.5 V, second pulse bias = −0.2 V, first and second pulse widths = 1 ms, sampling rate = 90 kHz, number of samples = 5000, number of scans = 4000. 95
5.5 Broadening of the emission rate peak of the E2 defect due to electric field effect. LDLTS measurement conditions: T = 78 K, $V_R = -2$ V, filling pulse = +2 V, second pulse bias = −0.2 V, first and second pulse widths = 1 ms, sampling rate = 77 kHz, number of samples = 4000, number of scans = 4000. 96
5.6 Splitting of the emission rate of E2 under uniaxial-stress along the [110] orientation. LDLTS measurement conditions: $T = 77 \pm 1$ K, $V_R = -0.5$ V, filling pulse = +0.5 V, second pulse bias = −0.3 V, first and second pulse widths = 1 ms, sampling rate = 96 kHz, number of samples = 10000, number of scans = 3000. The regularization parameters for resolving the inverse Laplace transform were automatically chosen by the Laplace transient Processor. 98
5.7 Individual curves from Figure 5.6, Showing the progression of the emission rate peak splitting under uniaxial stress. The horizontal axes determines the emission rate (s^-1), while the vertical axes is the DLTS signal (a.u.). 99

5.8 Plot of emission rate as a function of applied pressure at $T = 77$ K. The data in green is obtained from the data in Figure 5.6, however, for the blue and red plots the regularization parameters were manually set in order to better separate the peaks corresponding to each component (the blue and red points). 100
5.9 Plot of ΔE as a function of pressure. Similar to Figure 5.8, the green data points correspond to the data presented in Figure 5.6. The blue and red data points correspond to the effects of the applied pressure on individual components. 101
5.10 Arrhenius plot of the two components of the E2 defect under 0.18 GPa uniaxial stress along the [110] orientation. LDLTS measurement conditions: $V_R = -0.5$ V, filling pulse = +0.5 V, second pulse bias = −0.3 V, first and second pulse widths = 1 ms, sampling rate = 96 kHz, number of samples = 10000, number of scans = 3000. Emission rates under zero-stress conditions were measured using both the reference DLTS system (pink) and the stress DLTS system (cyan). 103
5.11 Arrhenius plot of the E2 defect under 0.18 GPa uniaxial stress along the [110] orientation. The plot shows the two components, $E2_a$ and $E2_b$, as well as measurements under zero stress from two different systems. LDLTS measurement conditions: $V_R = -0.5$ V, second pulse bias = −0.3 V, first and second pulse widths = 1 ms, sampling rate = 96 kHz, number of samples = 10000, number of scans = 3000. 104
5.12 Arrhenius plot of the two components of the E2 defect under 0.18 GPa uniaxial stress along the [110] orientation. The capture cross sections were predetermined to be 1.7×10^{-13} cm^2. LDLTS measurement conditions: $V_R = -0.5$ V, second pulse bias = −0.3 V, first and second pulse widths = 1 ms, sampling rate = 96 kHz, number of samples = 10000, number of scans = 3000. 105
5.13 Schematic illustration of an optimized sample holder. The design incorporates a stainless steel outer shell to ensure stability under high pressure while a copper core and contact surface is used to improve heat transfer to the sample. 115

List of Tables

2.1 Stress potential for non-cubic centers. After McGuigan et al. (2000) 48
2.2 Number of split components expected from application of uniaxial stress for the three major crystallographic orientations. After Kaplyanskii (1967) 49

3.1 Features and specifications of the compression load cell and the Process meter controller. Information taken from Omega Engineering Inc. (LMC320 and DP25B-S) 58

5.1 Important I-V characteristics of the SBD. 92
5.2 C-V characteristics of the SBD. 92
5.3 Summary of the results obtained by our stress DLTS system for the E2 defect. 109
5.4 Summary of the results obtained by Hartnett and Palmer (1997) for the E2 defect. 110
5.5 justify=left 111

Abbreviations

SBD	**S**hottky **b**arrier **d**iode
DLTS	**D**eep-**l**evel **t**ransient **s**pectroscopy
LDLTS	**L**aplace **d**eep-**l**evel **t**ransient **s**pectroscopy
MBE	**M**olecular **b**eam **e**pitaxy
RED	**R**esitive **e**vaporation **d**eposition
MS	**M**etal-**s**emiconductor

Physical Constants

Boltzmann constant	k	$=$	$1.380\ 658 \times 10^{-23}$ JK^{-1}
Elementary charge	e	$=$	$1.602\ 177 \times 10^{-19}$ C
Electron rest mass	m_e	$=$	$9.109\ 390 \times 10^{-31}$ K
Plank's constant	h	$=$	$6.626\ 076 \times 10^{-34}$ Js
Electron-volt	eV	$=$	$1.602\ 177 \times 10^{-19}$ J

Symbols

α	Temperature coefficient
$I-V$	Current-voltage
$C-V$	Capacitance-voltage
ϕ_{Bn}	Schottky barrier height
ϵ_s	permittivity of a semiconductor
ϕ_{IV}	I-V barrier height
ϕ_{CV}	C-V barrier height
$\rho(x)$	Charge density
$\phi(x)$	Electrostatic potential
$e\phi_m$	Metal work function
$e\chi_s$	Electronic affinity of a semiconductor

Dedicated to my Parents

Chapter 1

Introduction

One of the interesting topics in the field of solid state physics is the study of semiconductor materials. The semi-conducting phenomenon was first observed by M. Faraday in 1833 when he observed that unlike metals, the electrical conductivity of Ag_2S was increased as the temperature was raised. Later on, in 1851 J. Hittorf presented a more conclusive study of the temperature dependence of electrical conductivity for Ag_2S and Cu_2S (Łukasiak and Jakubowski, 2010). Further studies by K. F. Braun and A. E. Becquerel led to the discovery and analysis of the current rectification and photovoltaic effect associated with these materials (Sarkar et al., 2006) (Smith and Taylor, 2008).

There is no doubt that semiconductors are one of the pillars of modern technology. Various electronic and electromechanical components that are in use today are partially or entirely made out of semiconducting materials. Considering the significant impact that these devices have had on the advancement of technology,

it is only logical to assume that better understanding of the properties of semi-conducting materials, would ultimately contribute towards further advancements.

One method to describe the electrical properties of a solid is to utilize what is known as *energy band* model. According to this model, solids can be categorized into three different types, namely, conductors, insulators and semiconductors depending on the properties of the two prominent energy bands (Conduction and Valence) and the *band gap*. The band gap is the difference in energy of the lowest conduction state and the highest valence state is a region within the electronic energy structure of a solid where no energy states are available for charge carriers to occupy. This band gap is one of the main contributing factors towards electrical properties of materials. In general, the band structure of a solid is the result of quantum interactions among electron levels of individual atoms with one another and therefore it is a byproduct of the atomic structure of the solid. Hence, if this atomic structure is perturbed in any way, the effects might be observed in the band structure.

Even though semiconductors can be manufactured with very high purity, there are often still some detectable imperfections contained within their crystalline structure. These imperfections, whether structural or impurity related, are mostly created unintentionally during crystal growth and device processing procedures and are called *defects*. Defects come in a variety of different types and they perturb the atomic structure of the solid. There are *extended* and *point* defects, each with their own unique characteristics and effects. Some defects cause discrete energy levels within the band gap where no expected states exist. Furthermore,

depending on their respective energy levels within the band gap, defects can be categorized into *shallow-levels* and *deep-levels*. Shallow-levels produce *bound states* close to either the conduction band or the valence band whereas bound states corresponding to deep-levels are usually closer to the center of the band gap.

Defects play a significant role in device performance as they might act to alter the electrical properties of the material. While in most cases, the presence of defects has negative consequences regarding performance (through a variety of different dynamics such as decreasing carrier mobility and lifetime), there are cases where these defects are beneficial and therefore are intentionally introduced into semiconductors.

To elaborate on the previous statements, one can consider the case of semiconductor doping. Dopant atoms belong to the category of shallow-level defects. When specific elements such as phosphorous or boron are diffused into a semiconductor substrate such as Si, in precise concentrations, they introduce one electron more, or one electron less than a semiconductor atom would, and are referred to as donors or acceptors respectively (note: there is no charge imbalance!). Depending on whether they add or remove electrons from the semiconductor, dopants create n-type or p-type semiconductors required for almost all of the modern electronic components. However, merely adding any foreign atoms into the semiconductor lattice would not result in such beneficial creations. More often than not the existence of foreign atoms in high concentrations leads to suppression, alteration or degradation of some of the essential properties of the host semiconductor and therefore can render a device unsuitable for its intended application. Another

beneficial use for deep-level defects is gold implantation to produce recombination centers that increase the switching speed of p-n diodes.

Contamination with transition metals such as iron, nickel, gold and so forth during device processing, is one of the unintentional methods of introducing deep-levels in semiconductors. This type of defect can also be introduced if the semiconductor is subjected to nuclear radiation. These deep-level defects create what is known as generation and recombination centers that act as traps for charge carriers. By creating discrete energy levels within the band gap, these defects influence the movement of charge carriers that can potentially interfere with proper operation of various semiconductor-based devices such as transistors, solar cells and light emitting diodes.

Since some of the most important properties of semiconductors are dependent on the existence of defects or lack thereof, any research that leads to improvements in our understanding of the underlying dynamics involved with these imperfections would be immensely valuable and worthwhile. Such efforts can lead to design and construction of more efficient, faster and optimized devices, hence positively affecting properties such as efficiency and speed of a device.

To study semiconductor defects, one can make use of methods such as electron paramagnetic resonance (EPR), infrared absorption spectroscopy (IR) and deep-level transient spectroscopy (DLTS). Each technique provides a unique insight into the electrical and structural characteristics of a defect. However, each one also has its limitations. Difficulties arise when the sensitivity of a technique cannot be improved beyond an absolute limit or when, due to the primary mechanism

of operation of a technique, specific information cannot be derived from measurements.

As an example, a possible method to obtain structural information about a deep-level defect is by comparing the data acquired from generation and annealing processes of a defect and those obtained from either IR or EPR measurements. However, in practice, for the latter technique to yield accurate results, the net density of the defects within the substrate has to be so high that it interferes with the accuracy of the former technique. On the other hand, the highly sensitive DLTS technique operates based on the interactions between defects and charge carriers to identify and characterize these bound states and their ionization enthalpy E_T. However, since these interactions are purely electronic, they fail to provide any information regarding the physical structure and composition of the defects in the lattice. Therefore, DLTS as the sole characterization technique can only be used as an electrical characterization method (Dobaczewski et al., 2004).

In a semiconductor with a crystalline structure, energy bands occur due to overlapping of all the discrete atomic orbitals of all the individual atoms which result in the formation of a large number of closely spaced orbitals which when viewed together can be seen as a band. The rest of the range of energies that electrons are not allowed to occupy leads to the formation of the band gap. For an ideal crystal, energy bands are uniform and the band gap is devoid of any permissible atomic orbitals for electrons to occupy. This uniformity is due to the periodicity and identicality of the constituent atoms. However, in the presence of defects, possible permissible orbitals might exist that does not belong to any energy bands,

thus creating discrete energy levels within the band gap. The position of these discrete levels within the band gap depends on the electronic nature as well as the position and composition of the defect within the crystal lattice. Therefore, if an external influence were to perturb the positioning or the geometry of a defect, the corresponding energy level E_T of the defect's bound state would change. This external influence can be an applied uniaxial stress. By determining the correlation between the applied stress and the change in a defect's ionization enthalpy, it is possible to derive information regarding its structure and positioning (Sze and Ng, 2006).

Another interesting property of deep-level defects is the orientational degeneracy of their bound states. DLTS measurements reveal that under constant and controlled circumstances, the bound state corresponding to a defect always occupies the same energy level E_T regardless of its orientational positioning within the crystal structure. However, as uniaxial stress is applied to the sample this degeneracy may be lifted and identical defects positioned at different crystal orientations be perturbed differently, thus splitting the E_T into multiple components, thereby revealing the density of the defect in different orientations.

The objective of this study is to use the concepts and theories above to design and build a device capable of performing stress-dependent LDLTS measurements.

Chapter 2

Semiconductors

This chapter aims to briefly discuss topics which lay the foundation of semiconductor science. This chapter includes:

- An overview of crystallography and energy band configurations.
- A general description of semiconductor defects, their properties and how they are categorized.
- The physics of metal-semiconductor contacts and Schottky barrier diodes.
- Principles of DLTS measurements and the integration of uniaxial stress into the technique.
- The methodology for determining the structure of a defect based on uniaxial-stress studies.

2.1 Theory of solids

Solids are a group of materials commonly identified by their rigidity and tendency to keep their form under stress. However, to scientifically define the term "solid" one must shift one's attention to the atomic structures and not to the macroscopic behaviors and properties. Ordinary glass, for instance, demonstrates nearly all the properties expected from a solid material, but in reality, glass is a liquid with very high viscosity.

Different solids have different atomic structures in terms of geometry, which can be defined as the order with which their atoms are positioned relative to each other. In this regard, solids can be categorized into crystalline and non-crystalline types. Figure 2.1 is an illustration of two arbitrary solids. Non-crystalline solids, also called amorphous Solids, are made up of atoms or molecules arranged in a random patterned without any order or periodicity to their placements.(Zallen, 2008). In contrast, crystalline solids are solids with regular geometrical atomic structures. As it is evident from Figure 2.1 (b), crystals are made up of identical building blocks that are positioned in a highly ordered and periodic pattern.

Crystal structure

The periodic nature of a crystalline structure provides a suitable basis for application of mathematical descriptions (Kittel, 2004). Here a brief introduction to these mathematical descriptions are presented to familiarize the reader with some of the basic and essential concepts in crystallography such as cell geometry, crystal plains and crystal orientations which are central to this study. Should the reader

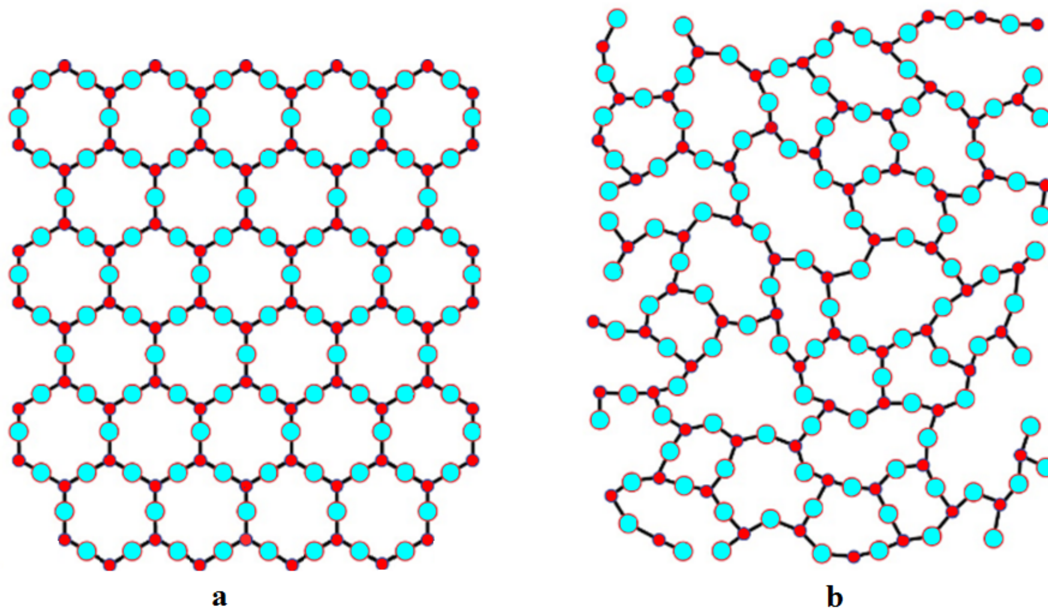

FIGURE 2.1: The Difference between the atomic structure of two arbitrary crystalline (a) and amorphous (b) solids.

require a more detailed view, they are encouraged to refer to respected textbooks such as *Solid State Physics* by *Neil W. Ashcroft and N. David Mermin* or the internationally recognized *Introduction to Solid State Physics* by *Charles Kittel 2004*.

In general, crystalline structures can be defined in terms of a lattice where every lattice point is occupied by a building block. In this case, a building block may be a single atom or a group of atoms. A simplistic, two dimensional representation is illustrated in Figure 2.2.

A three dimensional crystal lattice can be described mathematically by three translational vectors; $\vec{a}_1, \vec{a}_2, \vec{a}_3$ so that:

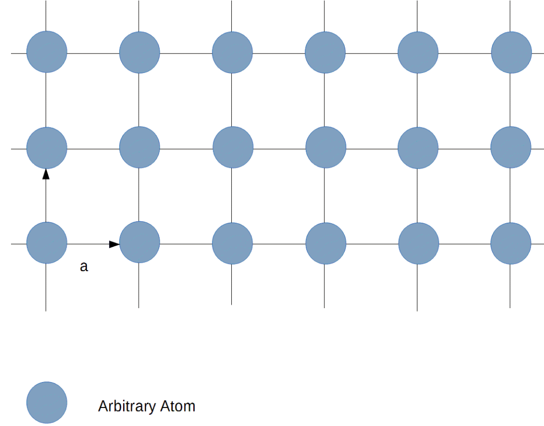

FIGURE 2.2: A 2D illustration of a crystal lattice.

$$\vec{r^{'}} = \vec{r} + v_1\vec{a}_1 + v_2\vec{a}_2 + v_3\vec{a}_3 \quad (2.1)$$

Where $\vec{r}$ and $\vec{r^{'}}$ are points of view from which the atomic arrangement within the lattice is being observed and v_1, v_2, v_3 are arbitrary integers. The mathematical set that contains all the points $r^{'}$ given by every combination of v_1, v_2, v_3 defines the lattice. Given that the atomic arrangement is identical when viewed from either of points r or $r^{'}$, the translational vectors $\vec{a_1}, \vec{a_2}, \vec{a_3}$ are referred to as primitive vectors with $a = 1, a = 2, a = 3$ being the lattice constants pertaining to the distance between individual lattice points. It must be noted that the previous statement is only true for cubic lattices. For the case of non-cubic lattices, $a_1 \neq a_2 \neq a_3$ (Kittel, 2004).

Furthermore, a translational operation can be defined as moving every point in the primitive cell from one lattice point to another while the atomic composition of the cell is kept constant. Such an operation can be expressed as:

$$T = v_1\vec{a_1} + v_2\vec{a_2} + v_3\vec{a_3} \quad (2.2)$$

where T is a translational vector which for different values of v_1, v_2, v_3, connects any two different lattice points (Kittel, 2004).

Therefore, a crystal is nothing more than billions of identical units joined together to form a macroscopic construct. This concept simplifies the study of crystals significantly since in ideal cases the results of studying a single unit can be mathematically expanded to describe the entire crystal.

Different crystals have different primitive cell geometries. The most basic cell structure is the simple cubic structure that constitutes in total of one building block in a cubic configuration (Figure 2.3). However, there is a variety of different configurations in nature known as *Bravais lattices*. Some of the more common ones are depicted in Figure 2.3.

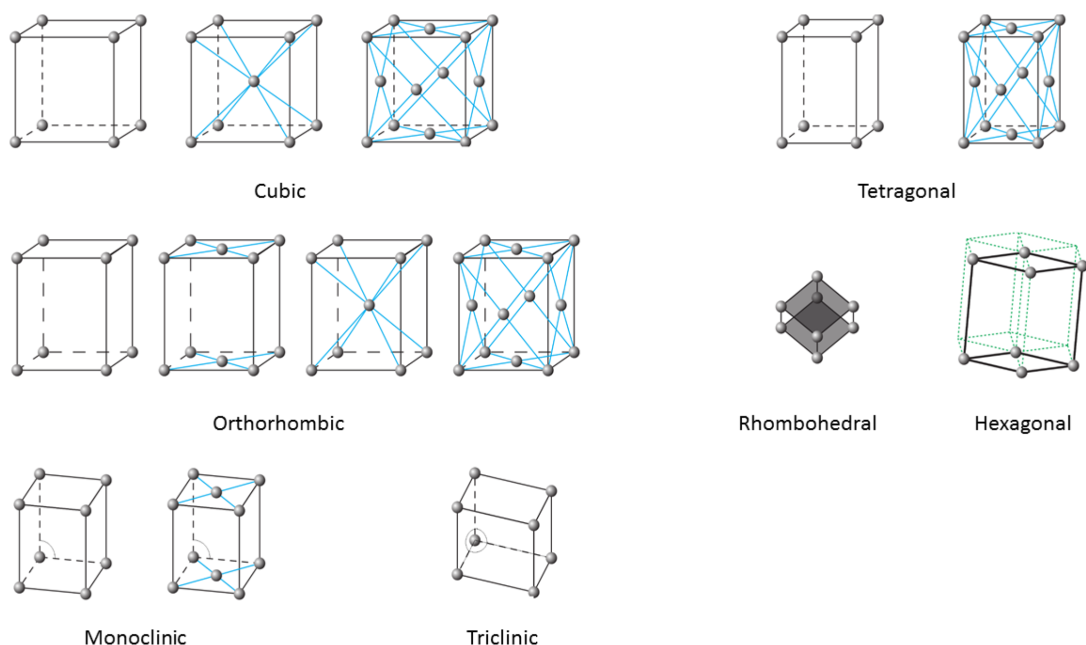

FIGURE 2.3: Various Bravais lattices. Image reproduced under the GNU Free Documentation License from Wikipedia.org

Furthermore, certain hybrid geometries are also possible. Two interpenetrating FCC lattices create a *diamond* or *zinc blende* structure. Well known Semiconductors, having this structure, including silicon, germanium, and gallium-arsenide belong to these two categories (Sze and Ng, 2006).

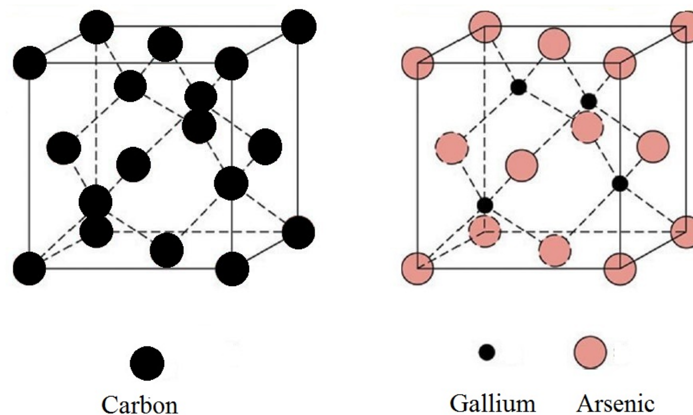

FIGURE 2.4: Diamond and Zinc blende lattices

Miller indices

The study of the volumetric structure of a crystal provides insight into the properties of the solid. For instance, certain physical or electrical attributes of many solids are orientation dependent. This is due to the fact that not all unit cell geometries are symmetrical under all transformation operations. Therefore, it is also important to introduce a method for describing the surfaces, planes, and crystal orientations in mathematical terms (Kittel, 2004).

To describe planes and orientations using the "Miller indices", one must follow a set of steps as follows:

- Find the intercepts of the plane with the primitive axes as a multiple of the lattice constant.
- Find the reciprocal of these numbers and multiplying them by a suitable number to produce three integers.
- Finally, reduce these numbers to the smallest integers h, k, l with the same ratio.

To report the indices corresponding to a plane, the values are enclosed in parenthesis to indicate a group of parallel planes (Kittel, 2004) (Sze and Ng, 2006). Figure 2.5 Demonstrates a number of important planes within a cubic structure.

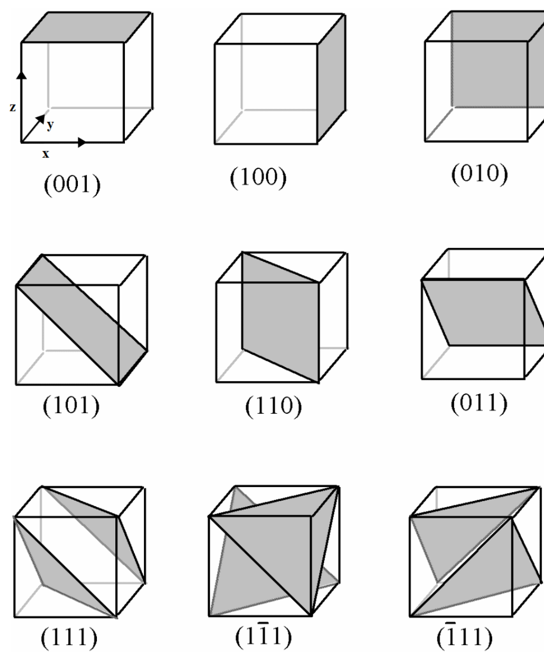

FIGURE 2.5: Crystal planes and their associated Miller indices.

Energy bands in solids

According to quantum theory, electrons in a single atom can occupy discrete energy levels called orbitals (Zettili, 2009). The same concept also applies to electrons in a group of atoms that form a solid. In this case, since electrons are not bound to a single atom but are influenced by multiple ones at the same time, the wave functions corresponding to these electrons overlap, shifting the energy orbitals or states into continuous energy bands since the wave functions are due to the symmetrical potential presented by the atoms, the wave functions should reflect the symmetry of the lattice. Bloch's theorem states that the energy eigenfunctions of electrons in such a periodic potential are given by a function of the form:

$$\psi_k(r) = \exp(ik \cdot \vec{r})u_k(r) \tag{2.3}$$

Where ψ_K is the Bloch wave, $\vec{r}$ is the position, u is a periodic function and k is the crystal wave function. This equation is a solution to Schrodinger's wave equation and defines the potential energy in a crystal lattice(Ashcroft and Mermin, 1976) (Kittel, 2004).

Figure 2.6 shows a plot of potential energy versus the Bloch's wave function for an arbitrary pure crystal lattice consisting of only one type of atom. Regions in the plot where solutions for the wave function exist, represent energy bands, whereas, the area depicted in red is where mathematically, no solution for the wave function exists. This region where no energy levels exist creates a gap that divides the continuity of permissible states into two regions or two separate bands;

one constituting of lower energy states (valence band) while the other contains the higher energy levels (conduction band). The width of this "forbidden" region can be determined by measuring the difference in energy levels of the highest valence state and the lowest conduction state and is called the "band gap" energy of the solid (Kittel, 2004).

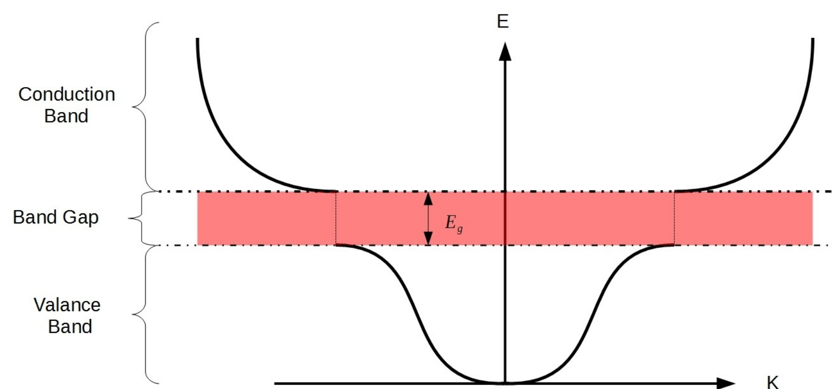

FIGURE 2.6: Plot of potential energy as a function of wave vector k for an arbitrary crystal lattice (After Kittel (2004))

In the presence of impurities or defects in the crystal lattice, certain discrete energy levels appear within the band gap which charge carriers can occupy. These discrete energy levels become fundamentally important when studying semiconductors and the performance of semiconductor-based devices.

The specific configuration of energy bands and band gaps in solids determine their unique electrical characteristics including their electrical conductivity. This can be used to categorize solids into conductors, semiconductors and insulators.

Two defining parameters for determining electrical conductivity of materials are the width of the band gap and the existence of de-localized states that extend

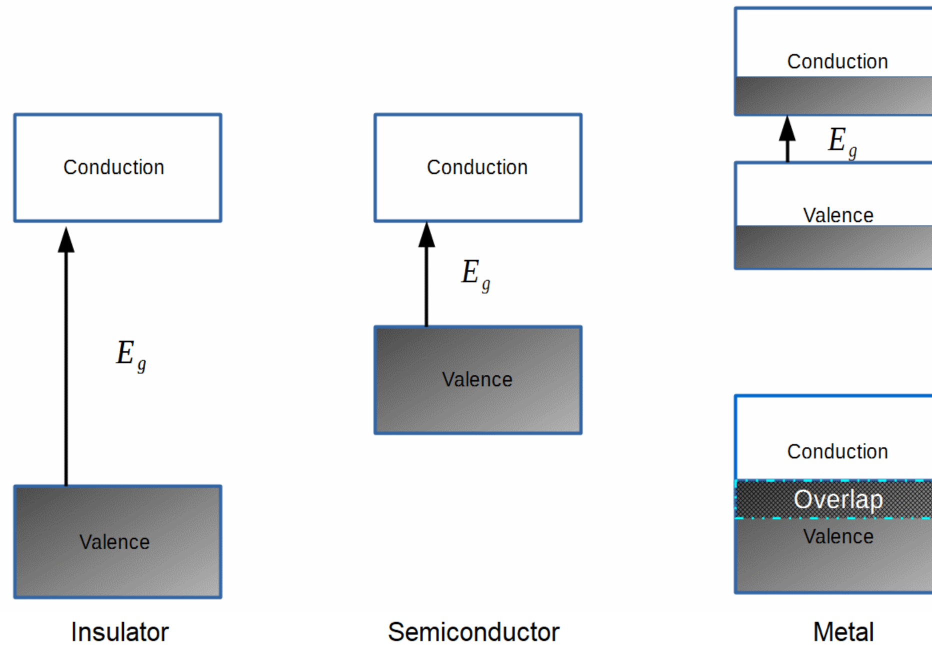

FIGURE 2.7: Energy band configuration of Insulators, Semiconductors, and conductors at 0 K

throughout the material. These states are responsible for transportation of electrons through the lattice but can only do so if they are in a band that is partially filled. If all the states in a band are occupied, there is no net current flow and therefore no conductivity. (Kittel, 2004) (Cutler and Mott, 1969).

2.1.1 Semiconductors

If the band gap of a material is small enough that electrons might be excited across it by thermal energy, it is called a semiconductor. Semiconductors are differentiated from other crystalline materials is their energy band structures and the properties stemming from this difference. The band gap energies associated with semiconductors, have values closer to 1.0 eV compared to band gap energy of insulators which can be relatively high (8.9 eV for SiO_2)(Kittel, 2004).

As mentioned in the previous section and is illustrated in Figure 2.7, in solids, conductivity is dependent upon fulfillment of two requirements, the value of *intrinsic charge carrier concentration* (n_i) and the availability of enough empty states for charge carriers to move through. Considering the case of negative charge carriers (electrons), in semiconductors, the valence band is filled and the only available empty states reside in the conduction band. For conduction to occur, electrons first need to acquire enough energy (usually through thermal or optical excitation) to overcome the band gap. As temperature rises from absolute zero ($T > 0$ K), the likelihood that electrons are able to undergo this transition increases. This constitutes that the conductivity of an ideal semiconductor increases with temperature. Figure 2.8 illustrates this phenomenon for some of the more important semiconductor materials.

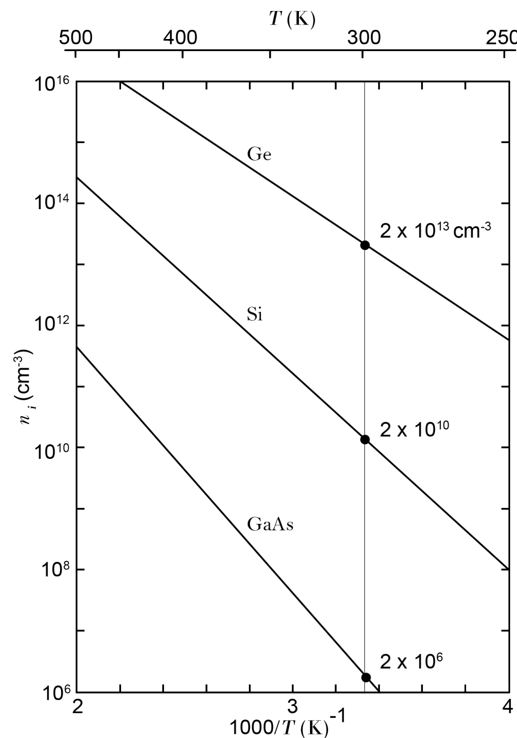

FIGURE 2.8: Temperature dependence of intrinsic carrier concentration in Si, Ge and GaAs. After Streetman (1994).

The carrier concentration is an important characteristic of semiconductors. The case described in the previous paragraph is valid only when dealing with a pure semiconductor free of any impurities or imperfections. In this case, the material is called an *intrinsic semiconductor*. When foreign atoms are added to a semiconductor, they act to alter the carrier concentration by promoting predominance of either negative or positive charge carriers. In this case, the material becomes an *extrinsic semiconductor*. The negative type or n-type semiconductors have an excess of electrons due to the existence of *donors* while in positive or p-type semiconductors holes are the dominant charge carriers created by *acceptor* atoms.

For extrinsic semiconductors, the carrier concentration is not only a function of temperature but also depends on the type of the added dopant and its corresponding concentration ($N_{A,D}$) in the crystal. Figure 2.9 demonstrates this relationship for p-type and n-type GaAs.

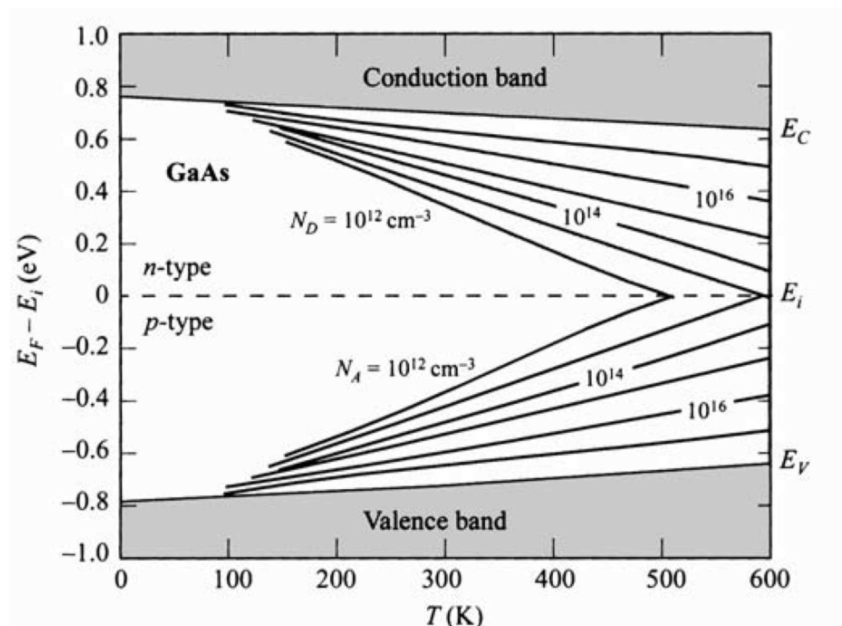

FIGURE 2.9: Carrier concentration dependence on temperature for n-type and p-type GaAs. After Grove (1967)

Semiconductors are also categorized in terms of the alignment of energy bands in momentum space. Referring back to Equation 2.3 it is possible to associate a wave vector $\vec{K}_{C,V}$ in momentum space with both the minimum energy level in the conduction band and the maximum energy state in the valence band. If $\vec{K_C} = \vec{K_V}$, the band gap of the semiconductor is said to be *Direct*. On the other hand, if $\vec{K_C} \neq \vec{K_V}$ the band gap would be *indirect* (Figure 2.10). In the case of a direct bandgap semiconductor, an electron is able to move from the conduction band minima to the valence band maxima by losing energy E_g in the form of emitting a photon. However, in an indirect band gap semiconductor, the same transition requires a change in the momentum of the electron (that is done through an intermediate state) which involves energy and therefore if a photon is emitted in this transition, it would have energy slightly different from E_g (Sze and Ng, 2006).

2.1.2 Semiconductor defects

By stepping away from the picture of an ideal crystalline structure, one realizes that even though these materials can be made very pure, there are always imperfections present in their crystalline structures. These imperfections are called defects. Defects can have a variety of different origins, physical and electrical characteristics. Some are point defects that perturb the periodicity of the crystal in a localized manner, such as antisites, interstitials and di-vacancies. Others are called extended or planar defects, affecting a plane or a region within the crystal, examples of which are dislocations and stacking faults. Furthermore, defects can

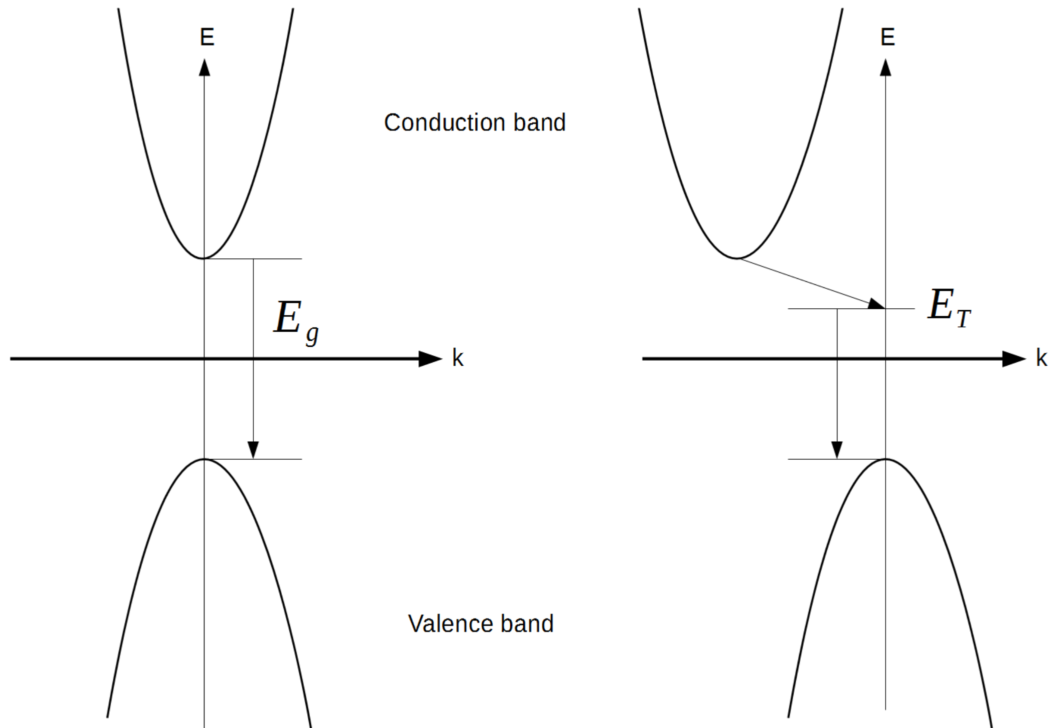

FIGURE 2.10: Direct and indirect carrier transport between the conduction and the valence bands

be categorized into two groups: *Native* defects are those that involve only the constituent atoms of the crystal while *extrinsic* defects are the result of introducing foreign atoms into the lattice.

As a result of the perturbation of the crystalline structure due to the presence of defects, the energy band structure of the material is also influenced. The presence of new states that can be of lower or higher energies compared to those belonging to the intrinsic atoms of the crystal affects the eigenvalues of the Schrodinger's equation used to describe the band structure of the solid. This results in appearance of discrete bound states within the forbidden zone, or the band gap (Streetman, 1994).

Depending on the localization of the defect state, they are classified into "shallow-levels" and "deep levels".

Also, in an intrinsic semiconductor, the Fermi level is situated approximately in the middle of the band gap, doping acts to alter the position of this level. This energy difference is called the *ionization energy* of the defect. Conventionally, the ionization energy of a donor level, E_d is measured relative to the conduction band while for an acceptor, E_a relates to the valence band. Since these energy states are very close to bands edges, the values corresponding to E_d and E_a are very small relative to the band gap energy and are referred to as *shallow levels.* A donor level with an excess electron bound to it is neutral, however, as soon as the electron is released and the level becomes positive. This transition is usually denoted as (0/+). Similarly, different charge states of acceptor levels are denoted as (0/-).

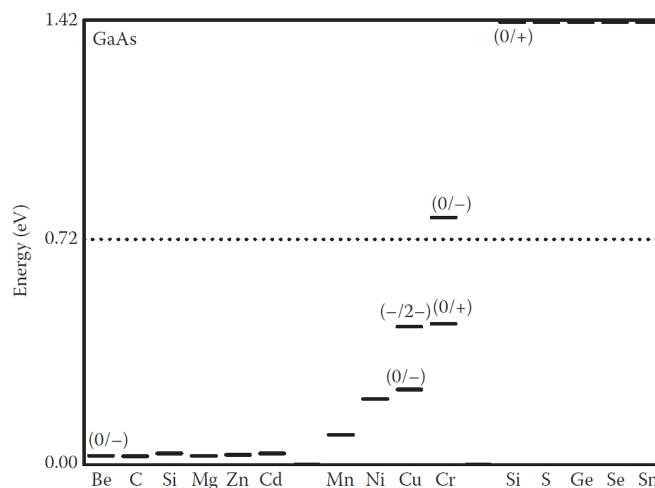

FIGURE 2.11: Shallow-level and deep level defects in n-type GaAs

Generally, the corresponding energy difference of a deep level from band edges is greater than that of a shallow-level. Deep levels are responsible for creating

localized states, where charge carriers are tightly bound. (McCluskey and Haller, 2012)

Figure 2.11 illustrates some of the defects and their charge states in GaAs at room temperature.

Generation-recombination centers and trapping

Generation and recombination processes act to create or destroy electron-hole pairs. Depending on the Fermi level, deep levels in semiconductors act to capture or emit charge carriers and hence promote either the generation or recombination processes to take place. There are only four possible events that can happen between the conduction band, the valence bands, and the trap, all of which are shown in Figure 2.12.

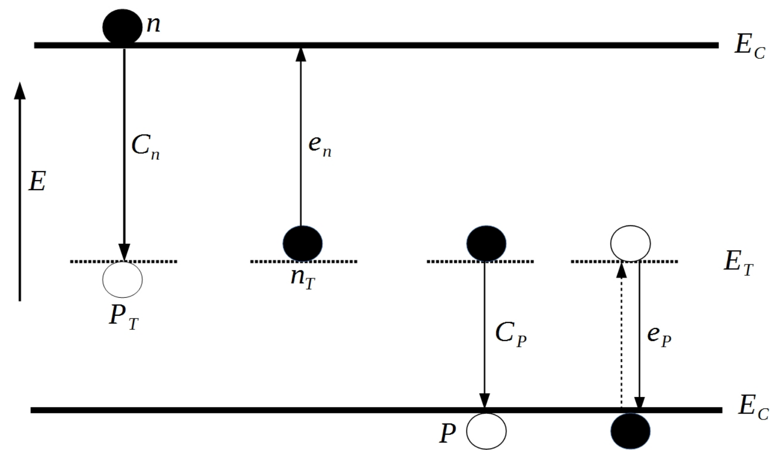

FIGURE 2.12: Generation-Recombination and Trapping events in semiconductors. In the figure: n refers to electrons while P refers to holes. C_n and C_P refer to capture events, e_n and e_p are emission events and P_T and n_T refer to trapped charged carriers.

From left to right; the deep level having energy E_T captures an electron from the conduction band. Now the deep level can either emit the electron back to the conduction band (electron emission) or capture a hole from the valence band. In both cases, the center is now occupied by a hole. It can either emit the hole to or capture an electron from the valence band. If after the initial electron capture by the deep level, it also captures a hole from the valence band, this event is called a *recombination* event. However, if the captured electron is emitted back to the conduction band and a hole is emitted to (or an electron is captured from) the valence band, this event is called a *generation* event. In a diode, under forward bias conditions, the dominant process is recombination which destroys an electron-hole pair, whereas, under reverse bias, generation process takes the lead. When the captured charge carrier is emitted back to the energy band that it was initially captured from, the event is neither recombination nor generation. Thus, it is called a trapping event (Schroder, 2006).

The general expressions describing the probability of capture or emission of a charge carrier are given by (Sze and Ng, 2006).

$$e_n = \sigma_n v_{th,n} \gamma N_C \exp(-\frac{E_C - E_T}{kT}) \tag{2.4}$$

for electrons and :

$$e_p = \frac{\sigma_p v_{th,p} N_V}{\gamma} \exp(-\frac{E_T - E_V}{kT}) \tag{2.5}$$

for holes.

Here σ_n and σ_p are the carrier capture cross sections associated with the defect level, N_C and N_V the density of states in the conduction and the valence bands. v_{th} the thermal velocity of the charge carrier and γ the degeneracy factor. Furthermore, T is temperature and k is the Boltzmann constant.

2.1.3 Gallium arsenide

Physical structure and properties

Gallium arsenide (GaAs) is a prominent member of a group of semiconductors commonly known as group III-V compounds. As is shown in Figure 2.13, it is made up of gallium and arsenic atoms covalently bound together to form a zinc-blend structure. Each gallium atom makes bonds with four arsenic atoms (four nearest neighbors) to form a tetrahedron (Seebauer and Kratzer, 2008).

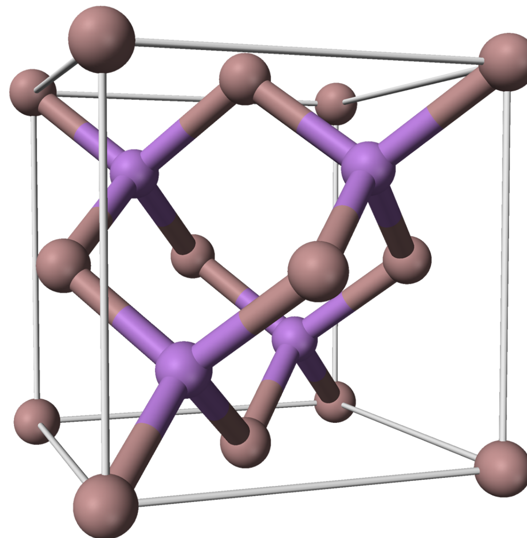

FIGURE 2.13: A GaAs unit cell. It consists of two inter-penetrating FCC structures that form a zinc-blende lattice. Image used under the Public domain license from Wikipedia.org

Electrical Properties

As a semiconductor GaAs is the subject of much attention from both industry and academia, due to its desirable and in some cases unique electrical properties. GaAs is a direct band gap semiconductor with band gap energy equivalent to 1.33 eV at 273 K which makes GaAs a wide band gap semiconductor.

2.1.4 The E2 defect in GaAs

The E2 is an Alpha or Beta irradiation induced defect in GaAs that is stable at room temperature. It is observable in DLTS spectra within the temperature range of 65-85 K, with the DLTS peak point located at $T_{peak} = 78$ K and has an effective activation energy of $E_T = 0.139$ eV and an apparent capture cross section of $\sigma_{na} = 9.3 \times 10^{-14}$ cm^2 (Auret et al., 1993).

In an experiment by Hartnett and Palmer (1997), several of the irradiation induced defects in n-GaAs, including the E2 defect, were investigated by application of uniaxial stress and conventional DLTS. The aim of the study was to obtain information that would be used to determine the symmetry and structure of these defects. The other two defects under study were the E1 and the E3.

The substrate for their samples was epitaxially-grown silicon-doped GaAs with a carrier concentration of 4.5×10^{15} cm^{-3}. These substrates were of 2.0 mm $\times$ 2.0 mm $\times$ 6.0 mm dimensions with the longest side being parallel to the targeted axis. After the substrates were properly cut, an Ohmic contact was made on them

by tin alloying and two Schottky contacts were formed on the other side of the substrate. The Schottky contacts were made of aluminum and were 1.0 mm wide.

The DLTS system was a double-boxcar system mounted onto a beam-line of a Van de Graaff Ion Accelerator. The samples were irradiated over a temperature range of 10-450 K and the DLTS measurements were carried out over the same temperature range. These measurements were performed with and without applying stress to the samples.

To analyze the data, the researchers calculated theoretical DLTS spectra (for both the 0.0 GPa measurements and 0.4 GPa measurements) for a quantitative comparison with the experimental results (Hartnett and Palmer, 1997). Figure 2.14 shows the results of this experiment. The solid lines represent the calculated spectra , while the dots are actual experimental points. The figure demonstrates that the experimental results are in agreement with theoretical calculations. The broadening of the peak under uniaxial stress, applied along (110) orientation is clearly visible.

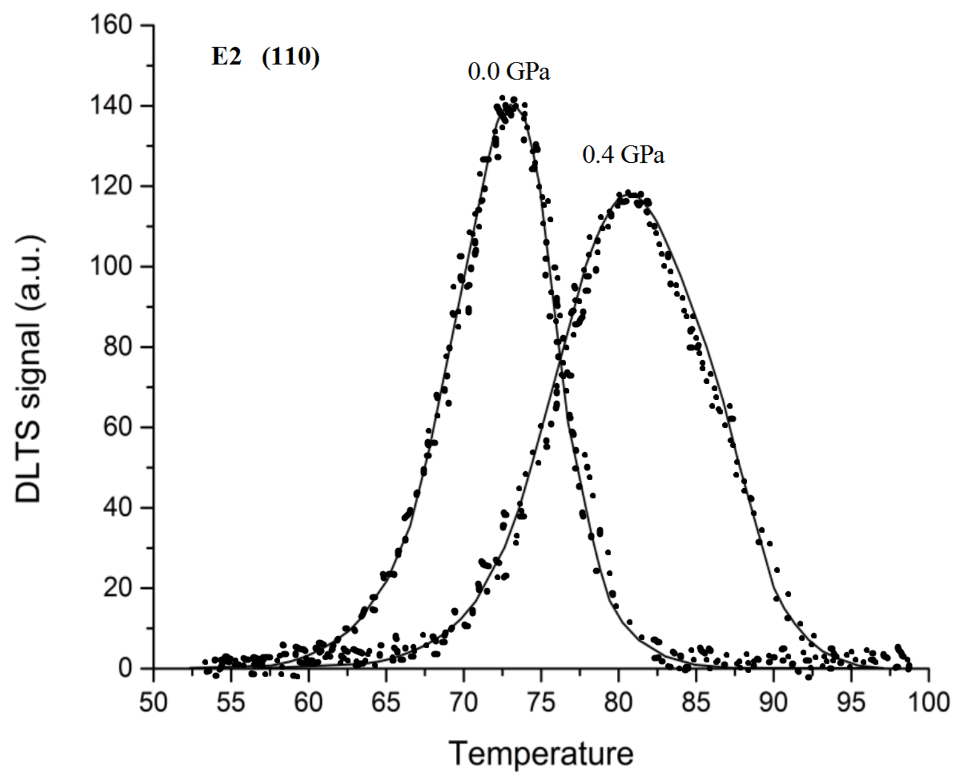

FIGURE 2.14: Conventional DLTS sccan showing broadening of the E2 peak under uniaxial stress along (110) orientation (Hartnett and Palmer, 1997). The Image was reproduced from hard copy version.

2.2 Electronic devices

Numerous electronic devices make use of unique electrical properties of semiconductors for their operation. These semiconductor devices rely on the electronic dynamics present at $p-n$ or metal-semiconductor junctions. The simplest form of a semiconductor device is made from a $p-n$ junction which forms a diode. As the electrons closest to the junction migrate from the n-type to the p-type semiconductor and recombine with the positively charged holes in the latter, a “depletion region” devoid of any charge carriers forms. This depletion region widens or shrinks depending on the direction of the applied potential and acts to either promote or block the flow of current. The same principle also applies to the metal-semiconductor junctions, whereas, in this case, either an n-type or p-type materials is used. Point contact rectifiers and Schottky diodes are examples of devices exploiting this principle.

While principles of operation of all these devices are the same, the type of junction used in each device determines its specific characteristics such as the value of forward voltage drop and switching speed capabilities. For further information on the subject, the reader is encouraged to refer to textbooks e.g by Schroder (2006) and Sze and Ng (2006).

In this study, Schottky diodes are used as the primary semiconductor device for the purpose of characterizing semiconductor defects. Therefore, it is essential that the reader is exposed to a brief description of the underlying electronic dynamics in

metal-semiconductor junctions as it forms the basis for the operation of Schottky diodes.

2.2.1 Metal-semiconductor junction

In 1938, German physicist Walter H. Schottky, following previous research by K. F. Braun, A. H. Wilson, and others, proposed that at the interface where a metal and a semiconductor connect, a potential barrier with possible rectifying properties forms. In the discussion below, a contact to an n-type semiconductor is considered. For p-type material a similar argument holds. The rectifying properties of this potential barrier, also known as the Schottky barrier, depend on the difference between the work function ϕ_m of the metal and that of the semiconductor ϕ_s. The work function is the minimum energy required to remove an electron from a metal or a semiconductor; or the energy difference between the Fermi level and the vacuum level. Figure 2.15 (a,b and c) illustrate ideal cases where $\phi_m < \phi_s$, $\phi_m = \phi_s$, $\phi_m > \phi_s$ respectively and the metal and semiconductor are in intimate contact with each other . This leads to the formation of different types of metal-semiconductor contacts. Here, χ is the energy difference between the conduction band maximum and the vacuum level, i.e. the energy released when an electron is added to the semiconductor, and is called the electron affinity of the semiconductor (Schroder, 2006) (Sze and Ng, 2006).

If $\phi_m > \phi_s$, due to the bending of the semiconductor energy bands, electrons migrate from the semiconductor into the metal and accumulate on the surface of the metal, leaving a region of the semiconductor called the space-charge region,

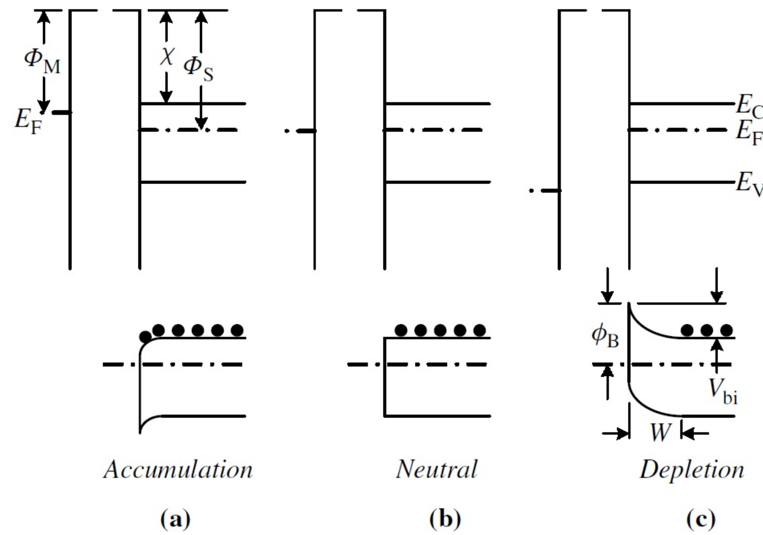

FIGURE 2.15: Metal-Semiconductor Contacts. After Schroder (2006).

devoid of any charge carriers. The accumulation of electrons on the surface of the metal creates a potential barrier at the junction that blocks the passage of electrons from the metal into the semiconductor. This phenomenon is responsible for the rectifying properties observed in metal-semiconductor contact and thus makes the depletion type contact the most important one. The parameter ϕ_B denotes the height of this barrier and can be written as:

$$\phi_B = \phi_m - \chi \tag{2.6}$$

When the junction is biased in the forward direction, the Fermi level, E_F, of the metal rises thus lowering the barrier from the point of view of an electron travelling from the semiconductor to the metal. The exact opposite of this phenomena happens under reverse bias conditions, resulting in electrons flowing from the semiconductor to the metal and encountering a higher barrier. It should also be noted that from the perspective of an electron in the metal, the barrier height

remains constant under either condition.

Even though Equation 2.6 describes an ideal case where there are no separating layers between the metal and the semiconductor, in practice, the formation of an oxide layer is inevitable. The existence of this layer results in the formation of an electrostatic potential difference between the surfaces of the metal and semiconductor that creates an additional potential barrier. However, if this layer is narrow enough, the electrons will have the ability to tunnel through it. Therefore, the effects can be neglected, and Equation 2.6 remains a valid approximation.

Aside from the barrier height, another important parameter in depletion type contacts is the width of the depletion region (indicated by W in Figure 2.4 (c)). This region is the space-charge region created due to the migration of the electrons from the semiconductor to the metal. In the zero bias condition, the width of the depletion region depends on the doping density N_D in such a way that it becomes narrower as the doping density increases and vice versa. At very high doping levels, the barrier becomes narrower and quantum tunneling becomes more probable. Therefore, electrons can tunnel through the barrier instead of having to overcome the potential barrier (Schroder, 2006).

As it was stated earlier, the depletion region is devoid of any charge carriers. However, there are states occupied by electrons at the edge of this region. When the voltage applied to the semiconductor changes, these charges are redistributed. This makes it possible to think of the depletion region and the two charged surfaces as forming a parallel plates capacitor. In this scenario, the capacitance would change depending on the width of the depletion region. By applying forward and

reverse bias pulses, it is possible to increase or decrease the width of this region and change the internal capacitance of the contact.

The capacitance of a parallel plates capacitor can be written as:

$$C = \frac{\kappa \epsilon_0 A}{W}, \tag{2.7}$$

where κ, ε_0 and A respectively denote the dielectric constant, permittivity constant and the area of the junction. W is the width of the insulator. If W is written as:

$$W(V) = \sqrt{\frac{2\kappa\varepsilon_0}{qN_D}(V_{bi} - V - \frac{kT}{q})}, \tag{2.8}$$

and substituted into Equation 2.7; the result will be:

$$\frac{1}{C^2} = \frac{V_{bi} - V - \frac{kT}{q}}{q\kappa\epsilon_0 A^2 N_d}, \tag{2.9}$$

where V_{bi} is the built-in potential-illustrated in Figure 2.15 (c)- and V is the applied bias. Equation 2.9 describes the relationship between the capacitance of the contact and the applied voltage. If the doping density N_D is constant, the plot of $1/C^2$ against V will take the form of a straight line with the slope $-2/(q\kappa\epsilon_0 A^2 N_d)$. However, if N_D is not constant, plotting $1/C^2$ with respect to V and analyzing the slope of the resultant curve is used to determine the doping profile of the contact (Schroder, 2006).

The capacitance of the junction is also sensitive to carriers trapped by deep levels within the depletion region. The relationship between the density of *filled* deep-states and the total density of deep states is given by:

$$e_p n_T = (e_n + e_p) N_T \tag{2.10}$$

Where n_T is the density of filled deep-states and N_T is the total density of deep states. Equation 2.10 can be rewritten as:

$$n_T = (\frac{e_n + e_p}{e_p}) N_T \tag{2.11}$$

Any perturbation that results in changing n_T, contributes towards changing the total charge of the depletion region, thus changing its capacitance.

When a quiescent bias V_R is applied across the junction is momentarily decreased, the width of the depletion region decreases. This allows for previously unoccupied states to start filling at a rate of:

$$\frac{dn_T}{dt} = c_n (N_T - n_T) \tag{2.12}$$

where c_n is the capture rate of defects for electrons. If the duration of the second pulse is long enough, it results in complete filling of the deep level, i.e. $n_T = N_T$. The additional negative charge reduces the capacitance of the junction. After the bias is returned to its quiescent V_R, the captured electrons are thermally emitted over a period resulting in restoration of the original steady state capacitance.

During the emission process, the number of filled states decay exponentially, leading to an *emission transient* that is given by:

$$n_T(t) = N_T e^{(-e_n t)} \tag{2.13}$$

with the emission time constant being:

$$\tau = \frac{1}{e_n} \tag{2.14}$$

The magnitude of the transient is used to determine the concentration of the deep states.

2.3 Deep level transient spectroscopy (DLTS)

DLTS, in its conventional form introduced by D.V. Lang in 1974, is one of the most sensitive and flexible techniques available for characterizing the electrical properties of deep-level defects in semiconductors. Conventional DLTS is used as a method for identifying deep levels in semiconductors.

Assuming that $n_T \ll N_D$, the region of defects emitting, does not change significantly. Therefore, the change in capacitance is described by a decay function as:

$$C(t) = C_\infty + \Delta C e^{-t} \tag{2.15}$$

Using Equations 2.9 and 2.13, the capacitance as a function of time can be written as:

$$C(t) = C_0(1 - \frac{n_T}{2N_D}) \tag{2.16}$$

Then:

$$C(t) = C_0(1 - \frac{N_T}{2N_D}e^{-\frac{t}{\tau_e}}) \tag{2.17}$$

where $C(t)$ is the capacitance as a function of time, C_0 is the steady state capacitance at V_R.

It becomes evident that the decay rate of $C(t)$ is dependent on the time constant τ_e which, using Equations 2.4 and 2.14, is shown to be temperature dependent:

$$\tau_e = \frac{\exp((E_C - E_T)/KT)}{\gamma_n \sigma_n T^2} \tag{2.18}$$

and at higher temperatures, electrons are more easily excited which increases the emission rate. At lower temperatures, the opposite is true. This concept forms the basis for DLTS measurements.

The *DLTS spectrum* is generated by applying an emission rate filter to the capacitance signal, which defines a *rate window* and generates a signal only when the emission time constant is within the rate window. The sample is then repeatedly pulsed while measuring the capacitance of the junction and the temperature is

scanned over a temperature range. This leads to a temperature dependent graph with one or more peaks. The peaks in this graph correspond to deep levels and the temperature at which they emit within the rate window is easily measurable.

Figure 2.16 demonstrates the DLTS cycle and how the change in capacitance of the junction corresponds to the generation of a transient.

- (A) This is the steady-state under the quiescent bias V_R. The deep-level state in the depletion region are empty as there are no charge carriers present to occupy them.
- (B) A filling pulse narrows the depletion region and allows the previously empty deep levels to capture electrons.
- (C) After the filling pulse has ended, the depletion region widens so that it re-encompasses the now occupied states. Since there is more negative charge present in the depletion region, the capacitance of the junction drops to a minimum value.
- (D) The capacitance begins to increase as the electrons are thermally emitted from the deep levels. This process continues until all the occupied states become empty and the capacitance stabilizes near the initial stable state.

This cycle is repeated multiple times and the values averaged to reduce noise. The DLTS temperature scan is repeated with different rate windows, thereby determining the emission rate (emission time constant τ_e) as a function of temperature. Hence, the activation energy E_T, capture cross section σ_n and the density of deep

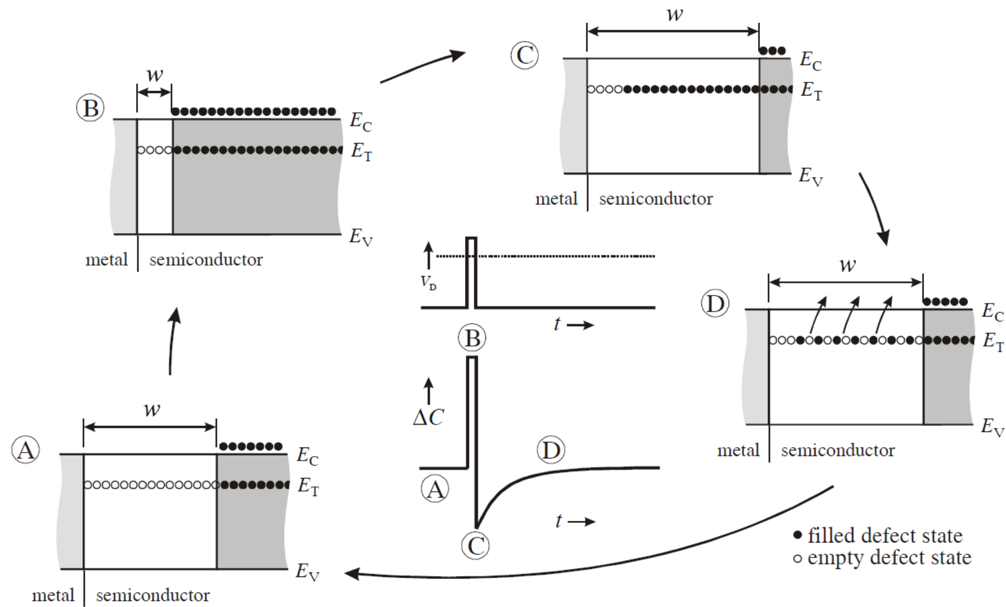

FIGURE 2.16: Schematic illustration of the DLTS cycle. After Miller et al. (1977).

states can be determined. The concentration of deep level may be determined from The change in capacitance (ΔC).

Early DLTS systems made use of analog electronics and data acquisition systems that significantly limited the resolution and capabilities of the technique. However, as more and more advances in computational power and mathematical techniques were made, analog electronics were replaced by digital signal processing. Data acquisition hardware associated with DLTS systems also underwent a significant upgrade which gave rise to digital DLTS systems with higher resolution and faster acquisition speed (Dobaczewski et al., 2004) (Meyer, 2006)(Schroder, 2006).

2.3.1 Laplace DLTS

DLTS transients are raw electrical signals recorded by the hardware and require processing before they can be used as manageable data. These raw signals consist of the capacitance transients engulfed in noise and, therefore, appropriate filters must be used to separate the two. In a conventional DLTS system, such as the one introduced by Lang (Lang, 1974), a double boxcar integrator was used as the linear signal filter.

Later on, the boxcar filter was replaced by *lock-in-amplifier* which poses a more favorable signal to noise ratio than that of a boxcar integrator, resulting in higher resolution and more accurate measurements. However, both of these techniques have resolution limits due to their analog nature. To address this shortcoming, various digital techniques were proposed where the analog input signal is digitized before the averaging step, therefore reducing the signal to noise ratio significantly. These digital techniques are referred to as *computer DLTS*. Since an in-depth discussion regarding the methodology behind these techniques is not directly relevant to this dissertation, readers are urged to refer to references (Schroder, 2006) (Meyer, 2006) (Dobaczewski et al., 2004).

Among the computerized or digital DLTS techniques, the highest resolution can be attributed to inverse Laplace transform DLTS, commonly referred to as *Laplace DLTS* or *LDLTS*. While most digital DLTS systems utilize the previously mentioned correlation technique as their primary signal processing method, in LDLTS

a different approach is taken which, if implemented properly, results in significantly improved resolution.

The main problem regarding processing the input signals arises from the fact that transients are essentially exponential decays, separating closely spaced exponential signals, while filtering out measurement noise, thus requires proper deconvolution algorithms. As mentioned earlier, every signal processing method results in sacrificing either resolution for better signal to noise ratio or vice versa. For instance, the Inverse Laplace transform provides high-resolution output signals suitable for observing fine structures within the spectrum but is very susceptible to noise. However, given the fact that modern instruments and digital data acquisition systems, are capable of reducing the level of measurement noise significantly, the higher resolution achieved by utilizing this algorithm, provides a suitable basis for structural analysis of defects. (Dobaczewski et al., 1994) (Dobaczewski et al., 2004) (Meyer, 2006) (Schroder, 2006).

The technique is based on the assumption that the observed transient consists of the summation of a spectrum of emission rates so that the capacitance transient, $C(t)$, can be written as:

$$C(t) = \int_0^\infty F(s)e^{-st}ds, \tag{2.19}$$

where, $F(s)$ is called the *spectral density function*. Equation 2.19 is the classic definition of Laplace transform of the function $F(s)$. However, in this case, $C(t)$ is a known parameter while $F(s)$ is unknown. Therefore, the aim is to determine

the function $F(s)$ corresponding to the transient $C(t)$ by employing an inverse Laplace transform operation. Since the Laplace transform of every function is unique to that function, this algorithm would effectively provide the means for distinguishing between different transients (different e^{-st} functions) corresponding to different defects within the input signal. In the ideal case, the inverse Laplace transform of the sum of a number of exponential decays will be a number of sharp peaks located at the emission rate constants of the individual exponential decay functions (Dobaczewski et al., 2004).

2.4 Integration of uniaxial stress into Laplace DLTS

So far into the discussion, it has been established that the operation of DLTS as a characterization technique relies on the emission processes involved with a defect under various temperature-related conditions. However, as it was explained in sections 2.1.2, electrical properties of defects fundamentally stem from parameters directly related to their physical structure within the crystal lattice. Therefore, disturbing these parameters and studying the resultant effects on emission rates of defects would lead to further insight into the structure of the defect (Dobaczewski et al., 2004) (Dobaczewski et al., 1995). There are several internal and external methods that can be employed for this purpose, e.g. the introduction of localized internal environments, lattice strain, and external hydrostatic or uniaxial stress.

In the present study, the focus is exclusively on uniaxial stress and its integration into a LDLTS system.

As a result of this integration, LDLTS becomes a structure sensitive technique capable of providing previously unavailable information regarding semiconductor defects. On a case by case basis, this information could lead to determination of symmetry, piezospectroscopic parameters, defect reorientation dynamics and also orientational degeneracy. However, the process of deducing this information from measurements is somewhat complicated.

While the perturbation caused by external stress is only aimed at the defect center, it inevitably affects the entire energy structure of the semiconductor, resulting in observable changes in the positioning of band edges and the width of the band gap. The change in energy level of the bound state corresponding to a deep center with respect to band edges can be written as:

$$\Delta E_{c,v} = E(F, Q_F) + E(e_{c,v}) - E(I, Q_I), \tag{2.20}$$

relative to either the conduction band or the valence band. Here, $E(F, Q_F)$ and $E(I, Q_I)$ are the total energies of the initial and final states of the defect. $E(e_{c,v})$, depending on the subscript, is the energy of an electron at the bottom of the conduction band or a hole at the top of the valance band (Dobaczewski et al., 2004).

In the absence of stress or strain on the defect, the energy level ΔE is determined by equations 2.4 and 2.5. However, a more general formula describing emission

rates is:

$$e_{n,p} = \sigma_{n,p} v_{th} N_C \exp(-\Delta G/kT) \tag{2.21}$$

The term ΔG is the change in Gibbs free energy of the emission which can be expanded according to the thermodynamic relation:

$$G = H - TS \tag{2.22}$$

to give Equation 2.21 the form:

$$e_{n,p} = \sigma_{n,p} v_{th} N_C \gamma \exp(-\Delta H/kT), \tag{2.23}$$

where γ is equal to:

$$\gamma = \exp(\Delta S/k), \tag{2.24}$$

and is called the degeneracy factor. Furthermore, ΔH which is the change in enthalpy can be rewritten as (Dobaczewski et al., 2004):

$$\Delta H = \Delta E + p\Delta V, \tag{2.25}$$

where ΔE is the change in energy of the deep level from the initial to the final state, and $p\Delta V$ denotes the change in the volume of the defect due to pressure.

When there is no pressure on the defect ($p \to 0$), the term $p\Delta V$ is negligible and therefore equation 2.21 can be reduced to the form of equations 2.4 and 2.5. However, in the presence of high pressure due to external stress, the change in

volume influences the change in the energy of the bound state. In this case, ΔV contains structural information about the defect.

In order to acquire structural information from ΔV, the change in volume must first be expressed in terms of stress induced deformation. This is achieved by expressing the effects of the applied stress in terms of partial derivatives of the activation energy with respect to the *stress tensor,* σ_{ij} of the defect as (Dobaczewski et al., 2004)

$$\frac{\partial}{\partial_{ij}}\Delta E = \frac{\partial}{\partial \sigma_{ij}}E(F, Q_F) + \frac{\partial}{\partial \sigma_{ij}}E(e_{c,v}) - \frac{\partial}{\partial \sigma_{ij}}E(I, Q_I) \tag{2.26}$$

Therefore, while effects of external stress on the defect levels and energy band structures can be understood from equation 2.26, it would be impossible to isolate the effects on a specific portion of the term using this approach.

Another approach that would potentially overcome this limitation is the study of the orientational degeneracy of deep levels. Anisotropic defects with low symmetry can often exist at various orientations within a crystal lattice. However, due to the symmetry of the crystal, the defects exhibit the same activation energy E_T regardless of their orientational placement. Hence, they are called orientationally degenerate defects. To lift this degeneracy, an external influence, such as uniaxial stress, that would have differential effects on the defect based on the orientation it is residing in, could be employed. In the context of DLTS studies, the results of this perturbation can be observed as a splitting of the emission rate spectra into separate components. These components, in turn, could provide the necessary

information for determining the point group symmetry that the defect belongs to. Figure 2.17, taken from Coutinho et al. (2003) demonstrates this phenomena for VOH (-/0) defect in silicon.

2.4.1 Determination of symmetry

In physics, symmetry is defined as **a property of a physical system that is unaffected by certain mathematical transformations**. Mathematically, the symmetry associated with a physical system is described using groups. These groups are organized based on the type and the number of symmetry transformations that they encompass. In crystallography, lattice symmetries are represented by *space groups*, while, *point groups* are used to define symmetry of unit cells and

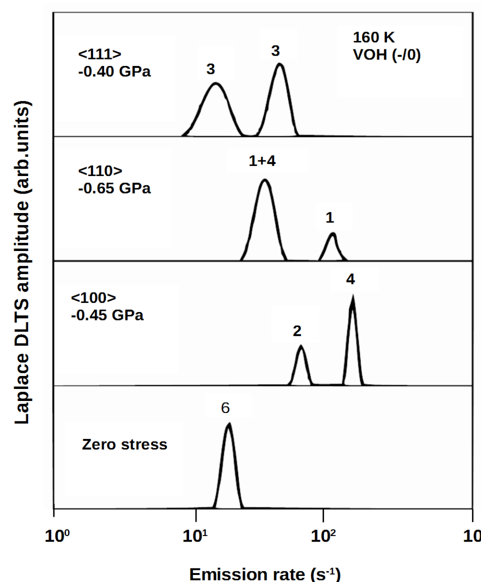

FIGURE 2.17: LDLTS spectra of VOH(2/0) defect at 160 K measured both at zero stress and under uniaxial stress along the three major crystallographic directions. From the splitting pattern, symmetry of the defect was determined to be orthorhombic-I, C-2v. After Coutinho et al. (2003).

point defects. Using the *Shoenflies notation*, these point groups include: (McCluskey and Haller, 2012) (Giacovazzo, 2002).

- Triclinic $(C_1, C_i = S_2)$
- Monoclinic $(C_2, C_s = C_{1h}, C_{2h})$
- Orthorhombic $(D_2 = V, C_{2h}, D_{2h} = V_h)$
- Tetragonal $(C_4, S_4, C_{4h}, D_4, C_{4V}, D_{2d} = V_d, D_{4h})$
- Trigonal $(C_3, S_6 = C_{3i}, D_3, C_{3v}, D_{3d})$
- Hexagonal $(C_6, C_{3h}, c_{6h}, D_6, C_{6v}, D_{3h}, D_{6h})$
- Cubic (T, T_h, O, T_d, O_h)

The number of non-cubic symmetry groups that can be associated with defects in a crystal is limited by the symmetry of the bravais lattice corresponding to that crystal. For instance, hexagonal systems cannot exist in cubic lattices. The possibilities are limited even more, due to the fact that even though certain symmetric systems can theoretically exist in a specific lattice, they are never realized in nature due to energetic stability considerations involved with their generation processes.

Most widely used semiconductors have cubic lattices. Non-cubic defects in these semiconductors can possess any of the following symmetries:

- Tetrahedral (T_d)

- Tetragonal (D_{2d})
- Trigonal (C_{3v})
- Rhombic I (C_{2v})
- Rhombic II (D_2)
- Monoclinic I (C_{1h})
- Monoclinic II (C_2)
- Triclinic (C_1)

When uniaxial stress is applied to a specific center, the effects uniquely depend on its initial symmetry. This information is obtained through observation of shifts and splits in the emission rate spectra, and they include the number of split components, the relative intensity of every component and the rate of shift in emission rate with respect to the magnitude of the stress for every component. To interpret this information, a proper approach is to employ a *piezospectroscopic* analysis of the stress data. However, the following analysis applies to cases where the defect is assumed to be of low symmetry and have no electronic degeneracy.

The number of split components points to the various orientationally degenerate states that can be associated with the center under study. As was implied above, in a cubic lattice, there are some symmetry operations under which the defect center remains invariant and, therefore, degenerate. However, this only applies as long as the cubic symmetry of the lattice is conserved. Mathematically speaking, when a cubic structure is subjected to stress, it deforms and, therefore, assumes a

different structure (with lower symmetry). Under this new structure, the validity of some or all symmetry operations becomes compromised. In this regard, when a cubic lattice is perturbed by external stress, the symmetry operations that were responsible for the orientational degeneracy of defects may no longer have the same effects and therefore, some or all of the orientational placement for a defect will be revealed as a splitting of the emission rate spectra. Now, depending on the number of splits under stress applied along various axes, it would become possible to associate the defect with one of the aforementioned point groups (Dobaczewski et al., 2004) (McGuigan et al., 2000) (Kaplyanskii, 1967).

As was mentioned earlier, the effects of stress on a system can be mathematically described in terms of a stress deformation potential, U_a. For a non-cubic defect in a cubic lattice, this deformation potential can be expressed as:

$$U_a = \sum_{i,j} A_{ij}\sigma_{ij}, \tag{2.27}$$

where A_{ij} is the piezospectroscopic stress tensor values, which are unique for every defect and can in principle be obtained from the slope of $\ln(e_{n,p})$ vs pressure (Dobaczewski et al., 2004) (McGuigan et al., 2000) (Kaplyanskii, 1967).

The bulk stress tensor with respect to the direction of the applied stress and the orientation of the defect is written as:

$$\sigma_{ij} = \vec{\sigma}\cos(\vec{\sigma}, i)\cos(\vec{\sigma}, j), \tag{2.28}$$

where $i, j \in h, k, l$, and the $\cos(\vec{\sigma, i})$ is the cosine of the angle between the stress vector $\vec{\sigma}$ and the defect axis i. Assuming that the applied stress is along the arbitrary orientation of <XYZ>, for different values associated with these variables, the product of Equation 2.27 determines the rate at which the emission rate spectra of the defect shifts as a result of the applied stress (McGuigan et al., 2000). The number of piezospectroscopic terms determines the number of expected split components, and, therefore, the corresponding level of degeneracy that can be associated with a defect of a specific symmetry.

The stress potential associated with non-cubic centers in a cubic crystal are given in Table 2.1.

TABLE 2.1: Stress potential for non-cubic centers. After McGuigan et al. (2000)

Group	Stress potential
T_d	$A_1(\sigma_{xx} + \sigma_{yy} + \sigma_{zz})$
D_{2d}	$A_1\sigma_{zz} + A_2(\sigma_{xx} + \sigma_{yy})$
C_{3v}	$A_1(\sigma_{xx} + \sigma_{yy} + \sigma_{zz}) + 2A_2(\sigma_{xy} + \sigma_{yz} + \sigma_{zx})$
C_{2v}	$A_1\sigma_{zz} + A_2(\sigma_{xx} + \sigma_{yy}) + 2A_3\sigma_{xy}$
D_2	$A_1\sigma_{xx} + A_2\sigma_{yy} + A_3\sigma_{zz}$
C_{1h}	$A_1\sigma_{zz} + A_2(\sigma_{xx} + \sigma_{yy}) + 2A_3\sigma_{xy} + 2A_4(\sigma_{yz} - \sigma_{zx})$
C_2	$A_1\sigma_{zz} + A_2\sigma_{xx} + A_3\sigma_{yy} + 2A_4\sigma_{xy}$
C_1	$A_1\sigma_{zz} + A_2\sigma_{xx} + A_3\sigma_{yy} + 2A_4\sigma_{xy} + 2A\sigma_{yz} + 2A_6\sigma_{zx}$

Table 2.2 demonstrates how the initial symmetry of the center can be determined based on the number of components the emission rate split into as a result of uniaxially applied stress along (100), (110) and (111) directions.

Table 2.2: Number of split components expected from application of uniaxial stress for the three major crystallographic orientations. After Kaplyanskii (1967)

	<100>	<111>	<110>
Tetragonal	2	1	2
Trigonal	1	2	2
Rhombic *I*	2	2	3
Rhombic *II*	3	1	3
Monoclinic *I*	2	3	4
Monoclinic *II*	3	2	4
Triclinic	3	4	6

Chapter 3

Design of the stress-dependent DLTS system

As it was explained in Section 2.4, application of uniaxial stress with LDLTS can be greatly beneficial in the study of semiconductor defects from a structural perspective. However, in practice, developing such a system is accompanied by certain difficulties that must first be addressed properly.

While a LDLTS system could be assembled using commercially available components based on designs previously developed and implemented by researchers such as Dobaczewski et al. (2004), the same approach cannot easily be applied to the assembly of the necessary stress inducing mechanical components. Even though there is a wealth of information available in the literature regarding design and successful integration of uniaxial stress with various defect characterization

techniques, the uniqueness of each experimental technique demands that these mechanical components be designed, machined and constructed in situ.

During a stress dependence study, the sample has to be put under external stress for the duration of the DLTS measurement. Therefore, during this time the setup can be thought of as a static system and as it is characteristic of such a system, equilibrium of forces, proper alignment and lack of static friction between different parts become important points to be considered if the samples are to survive the measurements.

With the previous points in mind, the first step in the design process was to make sure that all the custom components are compatible with the existing components in the system such as the cryostat. This is especially important since, due to the delicate nature of this type of experiment, incompatibilities that could lead to destabilization of the system, would inevitably influence the accuracy and reliability of the results.

Furthermore, the external stress that must be applied to the sample is relatively high and, if not applied correctly, could either interfere with measurements or damage the sample or other parts of the system. Therefore, proper mechanisms for transferring and directing the force onto the sample have to be devised. This can be achieved by making sure that firstly, all the force is maintained within the system and is not applied to the frame or other components as this could be a cause of destabilization. Secondly, all the moving parts have to be properly enclosed to ensure proper alignment. Thirdly, the movement of these parts must be restricted in every direction except along the direction of the applied stress.

Lastly, the interfaces between all the moving parts must be machined completely flat to prevent the creation of stress components along undesired directions. Also, to prevent stress-induced deformation, the type and dimensions of the materials used for each part of the setup has to be appropriate to manage the maximum amount of stress needed during measurements.

In case the applied force causes the sample to slip or break, the system will experience a noticeable shock. If not handled properly, this shock can damage certain components of the system. Therefore, necessary precautions must be taken to prevent this.

Sample preparation is also critical. Conventionally, the samples used in DLTS studies are made out of small and very thin (3 mm $\times$ 5 mm $\times$ 0.5 mm) square pieces of the semiconductor material with appropriate Schottky and ohmic contacts deposited on their front and back surfaces, respectively. Since these measurements are purely electronic characterizations, the physical dimensions should not influence the final results. However, for stress-dependent studies, the sample itself is part of the static system and its dimensions become an important factor. When a thin piece of material is subjected to external stress, it becomes prone to stress deformations such as buckling which results in the introduction of shear stress. In this study, the external stress has to be applied uniaxially to the sample and shear stress must be prevented. While it would be impossible to address this problem in an absolute fashion, one method of reducing the effects of shear stress is by using thicker and shorter samples, i.e. with a greater height to width ratio.

However, in doing so, other challenges arise, including difficulty in handling the samples and sample preparation which will be explained in due time.

3.1 Laplace DLTS setup

3.1.1 Hardware

The main electronic components for a LDLTS system, include a cryostat, a signal generator, a high precision, high-speed capacitance meter, a temperature controller and the necessary means for computerized data acquisition.

Cryostat

The cryostat used in this setup, shown in Figure 3.1, is an OptistatDN2, manufactured by *Oxford Instruments*. This cryostat relies on liquid nitrogen as the cooling agent and can operate over a temperature range from 77 to 500 K. While OptistatDN2 was designed mostly for optical measurements, the fact that it is a top loading cryostat (the samples are loaded into a probe and then inserted into the device), which makes it ideally suited for this application. The top loading feature allows the user to design and use custom-built probes that best suit their application.

FIGURE 3.1: The OptistatDN from Oxford Instruments Inc.

Capacitance meter

The capacitance meter used in this setup is a Boonton 7200, a model specifically recommended by the manufacturer for DLTS measurements due to its high resolution of 0.01 pF, fast response and fast recovery after overload. It is also one of the few models that is completely supported by the *Transient Processor Software* (discussed in Section 3.1.2). The existence of an IEEE-488 digital port makes this model suitable for computerized DLTS systems.

FIGURE 3.2: Boonton 7200 capacitance meter

Temperature controller

As it was discussed in Section 2.2.1, the emission rate of deep-levels is temperature dependent, therefore the ability to accurately record, control and stabilize the temperature of the sample is critical for the accuracy and repeatability of experiments. Equation 2.4 and 2.5 demonstrate that the relationship between the emission rate and temperature is exponential. Therefore, slight variations in temperature can interfere significantly with the results.

For the temperature controller to be able to provide the level of accuracy required by stress measurements, certain parameters must be considered. Firstly, the temperature sensor must be able to provide accurate and reliable readings. Secondly,

the temperature controller must have an analog output that changes in smallest possible increments. Thirdly, the control loop associated with the temperature controller must be fine-tuned and optimized to ensure temperature stability.

Commercially available temperature controllers that are marked as scientific instruments, generally meet the last two requirements to a satisfying level. However, the choice of temperature sensor has to be made by the user depending on their intended application.

Considering the above mentioned criteria, a Model 336 temperature controller by *Lakeshore Cryotronics* was used (Figure 3.3). This device is specifically designed for scientific and cryogenic applications and is also compatible with the *Transient Processor Software*. Just as the case of the capacitance meter, the existence of an IEEE-488 connector makes this device suitable for digital DLTS applications.

FIGURE 3.3: Lakeshore 336 temperature controller

The temperature sensor should preferably be mounted as close to the sample as possible, and must therefore be housed within the sample holder. However, as it will be demonstrated later on, the space available within this component is very limited and would not allow the use of any sensor that is dimensionally more than a few millimeters wide. This limitation can be overcome by using thermocouples.

Aside from their form factor, thermocouples are also able to operate over a wide range of temperatures. However, thermocouples are generally less accurate than other temperature sensors available, and this lack of accuracy directly affects the overall performance of the temperature controller to accurately measure and manage the temperature according to the set preferences. For this reason, thermocouples have to be properly calibrated before use. Otherwise, temperature inaccuracies can become one of the major sources of error in measurements. If not calibrated correctly, even a highly sensitive thermocouple can produce errors in excess of 10 K.

The thermocouple used in this setup is of the type chromel-Au/Fe (0.07 %) which is the preferred type for cryogenic applications due to the wide range of temperatures it can operate at (1.2 K to 610 K) thanks to its relatively high thermoelectric sensitivity at low temperatures. Furthermore, most temperature controllers such as *Lakeshore 336* have built-in calibration curves for this type of thermocouple which drastically reduces the time needed for calibration and optimization and can help reduce the margin of error in measurements.

Force measurements

To measure the applied stress, a compression load cell was used. The unit is a model *LMC302-2K* made by *Omega Engineering Inc.* that was connected to a model *DP25B-S DIN process meter controller*. Figure 3.4 shows the load cell and the process meter controller.

Table 3.1 presents a summary of the characteristics of the two units.

Table 3.1: Features and specifications of the compression load cell and the Process meter controller. Information taken from Omega Engineering Inc. (LMC320 and DP25B-S)

LMC302-2K Compression load cell	DP25B-S Process meter controller
Excitation: 5 V dc, 15 V dc max **Output:** 1 mV/V (nominal) **Accuracy:** ±0.5% FSO (linearity, hysteresis and repeatability combined) **Zero Balance:** ±2% FSO **Deflection:** 0.025 to 0.075 mm **Max Load:** 2000 N **Thermal Effects:** Zero: 0.009% FSO/°C Span: 0.036% FSO/°C **Safe Overload:** 150% of Capacity **Ultimate Overload:** 300% of Capacity **Bridge Resistance:** 350 Ohms minimum **Construction:** Stainless Steel **Electrical:** 1.5 m 4 Conductor Shielded Cable	**Input Ranges:** 0-100 mV, ±50 mV, 0-10 V, ±5 V, 0-20 mA, 4-20 mA **Isolation:** Dielectric strength to 2500V transient per 3mm spacing based on EN 61010 for 260 Vrms or DC working voltage **Input Protection:** Voltage Input = 120 Vrms max; Current Input = 100 mA max **Input Impedance:** 100 Meg ohms for 100 mV or ±50 mV input range; 1 Meg ohm for 10 V or ±5 V input range; 5 ohms for 20 mA current input range **Internal resolution:** 15 bits **Read rate:** 3/sec **Max error process:** ±0.03% of reading, ± 1 count **Step response:** 1 sec **Warm-up to rated accuracy:** 30 min **Load Regulation:** 1.1% **Line Regulation:** 0.02% per Vac **Analogue output (optional):** 0-10 V, 4-20 mA or 0-20 mA; may be assigned to a display range or to setpoint #1, when used as a proportional control output

Figure 3.4: Model DP25B-S DIN process meter controller (left) and Model LMC302-2K force meter (right). Images taken from Omega Engineering Inc. (LMC320 and DP25B-S)

Data acquisition

A digital data acquisition system is responsible for collection and transfer of data from measurement instruments to the computer in charge of data processing. The solution used in this setup is based on the multi-functional DAQ system, designed and manufactured by *National Instruments* . The system is comprised of one NI PCI 6251 internal card, one GPIB-USB connector, one 64-pin I/O cable and a connector block that provides the interface for connecting analog ports to digital ones.

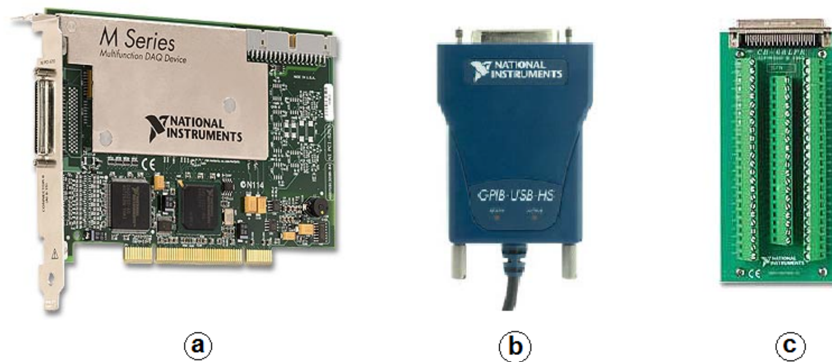

FIGURE 3.5: Various parts of the DAQ system: a) the NI PCI 6251, b) the GPIB-USB and c) the connector block.

The NI PCI 6251 is the heart of the digital DAQ system. It is responsible for converting the analog output of the capacitance meter into digital signals that can be processed using a computer. According to the manufacturer, the conversion process employed by this device increases the resolution of the signal by up to four times. The NI PCI 6251 is capable of high-speed sampling rates of 1.25 MS/s when only a single channel is used. This allows transients with shorter time constants (100 $\mu s)tobemeasured.Additionally, NIPCI6251alsofulfilstheroleofthepulsegeneratorinthis$

The GPIB-USB connector is used as the means for connecting different instruments to the computer for the purposes of automation and instrument control. The connector converts the I/O signals of IEEE-488 ports on devices into USB compatible signals and vice versa, allowing for manual and automatic control of each connected instrument through a computer software.

3.1.2 Software

The software package used in this study for the purposes of hardware control and data analysis was developed at the *Institute of Physics, Polish Academy of Sciences in Warsaw and the Microelectronics and Nanostructure Group, School of Electrical and Electronic Engineering at the University of Manchester.* At the core of the package is the *Transient Processor Software* which is responsible for recording and running the specified signal processing algorithms on the input signals. This package was designed to allow for a wide variety of measurements to take place, including conventional and LDLTS, and also C-V and I-V measurements. Other convenient features of the package include a measurement database program, a defect database which is editable by each user and the stand-alone transient processor utility which can be used to process pre-existing raw data.

There are also shortcomings in the operation and capabilities of the software package, the most important being that the choice of capacitance meters and temperature controllers in any experimental setup are limited to certain makes and models that are supported by the software and most of which are not always readily available.

All in all, the existence of such a well-developed software package, positively contributes towards accuracy and repeatability of defects characterization processes and therefore the efforts of all the scientists and software developers involved must be acknowledged to the fullest.

3.2 Apparatus and setup

The mechanical parts of the setup can be separated into various modules: the probe, stress module and the frame. The probe is based on a previous design by the late Professor L. Dobaczewski, *Polish Academy of Sciences*. The design was improved upon and adjusted to work with our existing cryostat.

3.2.1 The probe

As mentioned previously, the top loading feature of the OptistatDN2 allows for the use of specialized probes and inserts. Taking advantage of this feature, a special probe compatible with stress measurements was designed and built. As with any other part of the system, a modular design approach was adopted in developing the probe to ensure easy maintenance and upgradability of the components at later stages. Figure 3.6 demonstrates different parts of the probe and how they are assembled.

Sample holder and enclosure

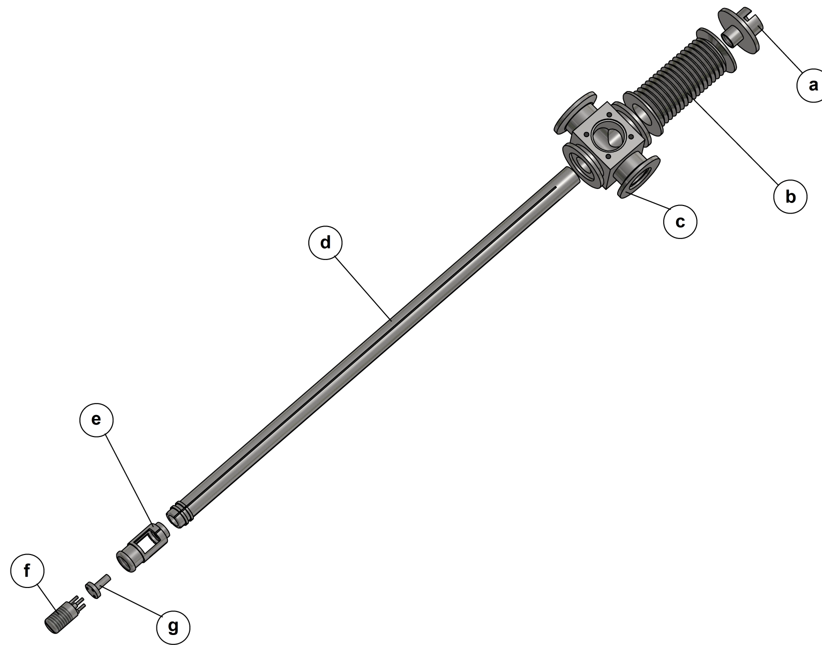

FIGURE 3.6: Various components of the stress probe: a) Force sensor housing. b) Bellows. c) Connector block. d) Body of the probe. e) sample holder housing. f) Anvil. g) Hammer (electrical components are not shown).

The sample holder resides at the bottom of the probe. In more ways than one, the sample holder can be considered the most important part of the design. Not only is it responsible for stabilizing the sample before and during measurements, but it is also part of the mechanism that transfers the external stress to it. Furthermore, since there are electrical connections going to and around the sample, the sample holder and its enclosure must be big enough to house those connections yet small enough to fit into the cryostat. The ease and the speed with which samples are mounted and dismounted are also among the important factors that influenced the design process. The sample holder and its enclosure as illustrated in Figures 3.7 and 3.8 were designed and built with all the aforementioned criteria in mind.

The sample holder itself consists of a hammer and an anvil that, while holding the sample in place, they also act to transfer the external stress to the sample. While

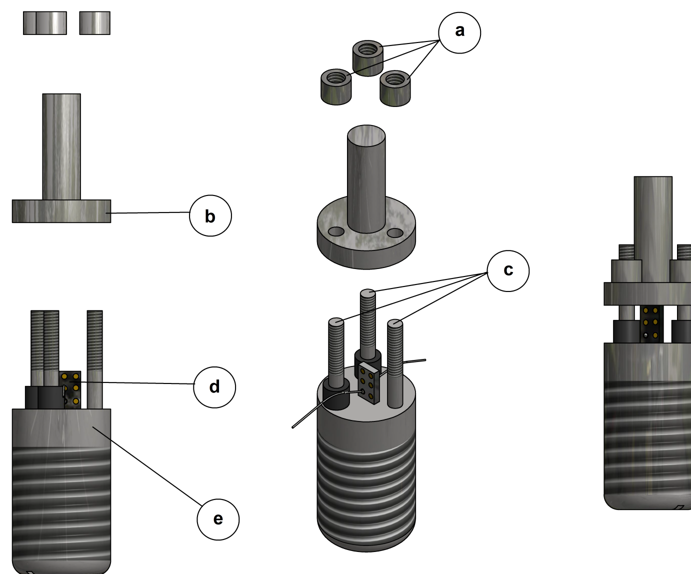

FIGURE 3.7: Sample holder. a) Nuts. b) Hammer. c) guide rods. d) Sample. e) Anvil.

the sample is mounted, the guide rods on the anvil and the accompanying nuts, act to restrict the movement of the hammer to only downward vertical direction. This ensures the stability of the sample when stress is applied. As can be seen in Figure 3.9, when a sample is mounted and the hammer is secured in place, the sample holder can easily be inserted into the enclosure.

The sample holder enclosure houses the sample holder, the internal heater and thermocouple that are respectively responsible for heating and measuring the temperature of the sample in real time and also the coaxial wires that connect the sample to BNC connectors at the top of the probe.

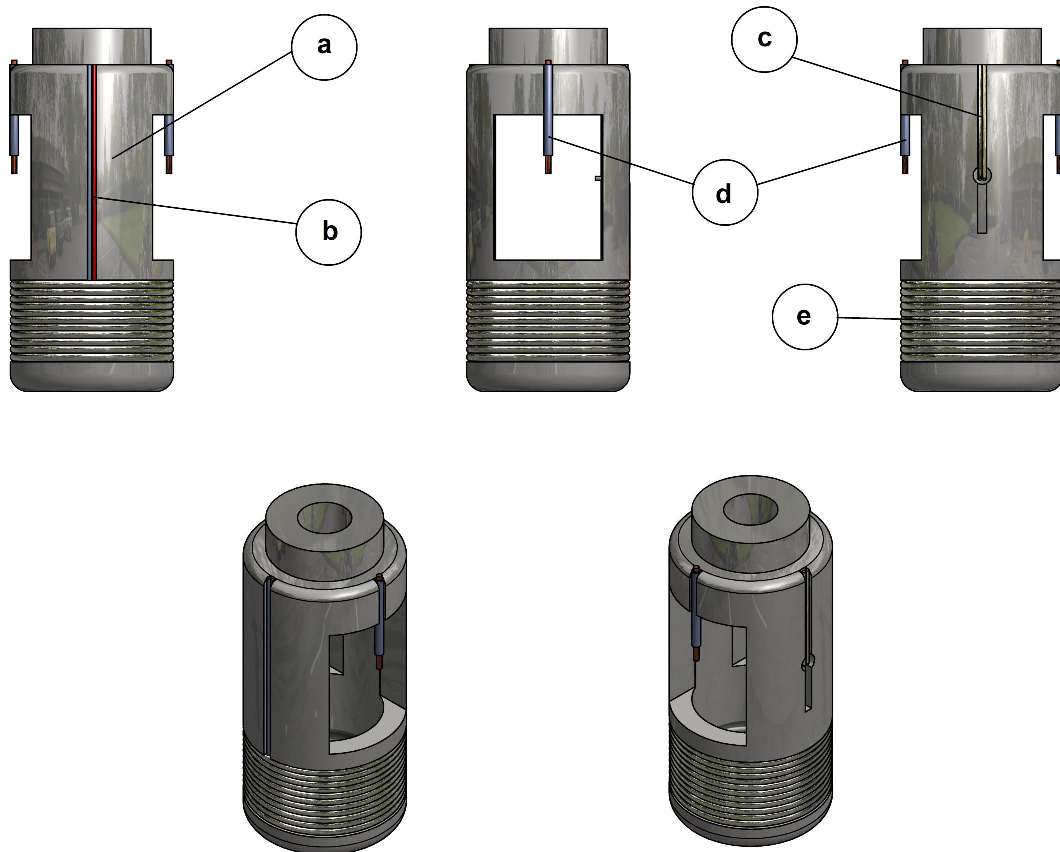

FIGURE 3.8: Sample holder enclosure. a) Body of the enclosure. b) heater wires. c) Thermocouple wires. d) Coaxial wires. e) Heater strip.

FIGURE 3.9: A demonstration of how samples are mounted into the sample holder and electrical connections are made.

Neck of the probe

The neck of the probe is made out of a hollow stainless steel tube that is connected to the sample holder housing at one end and the connector housing at the other. A stainless steel rod runs through the middle of this hollow tube and is the medium through which mechanical stress is transferred from the stress module to the hammer and then the sample. On the outer surface of the tube, there are four lengthwise grooves, illustrated in Figure 3.10, which house the wires that connect the sample, the thermocouple and the heater to the connectors in the connector block. These grooves are made not only to make the design tidier but also to prevent wires from fraying over time due to friction as the probe is taken in and out of the cryostat.

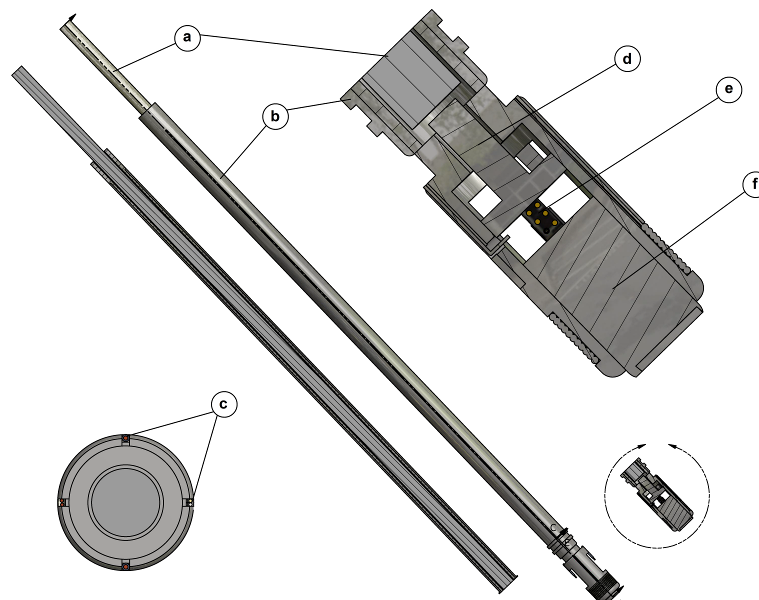

FIGURE 3.10: neck of the probe. a) Stainless steel rod. b) Hollow tube. c) Grooves where wires are fitted. d) Hammer. e) Sample. f) Anvil.

Connector block

The square part at the top of the probe is the housing for all the electrical connectors that connect the sample to other external instruments. Also from the bottom, it is the connecting junction between the cryostat and the probe, and from the top, it connects the probe to the stress module.

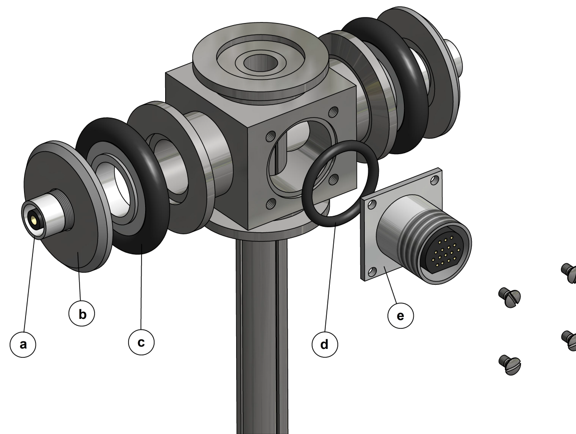

Figure 3.11: Connector housing. a) BNC connector. b) Blank QF flange converted to house the BNC connectors. c-d) O-ring. e) circular MIL-DTL-5015 connector.

Bellows and pressure sensor housing

Bellows allow for mechanical interactions to take place between a closed off system and the outside environment. This unique feature makes it possible to interact with the sample and apply mechanical stress while keeping the sample chamber under high vacuum. However, the use of bellows in this way could be problematic as it is a part that is prone to buckling under stress. Since the stability of the sample depends heavily on the smooth operation of all the mechanical parts, certain measures have to be taken to ensure that no buckling occurs. The conventional method to achieve this end is to place the bellows in a cylinder with an inner

diameter slightly wider than the outer diameter of the bellows. However, the use of such a method would lead to the introduction of an overcomplicated design that would compromise the modularity of the probe. To rectify this problem, a specially designed fastener was developed which will be explained later on.

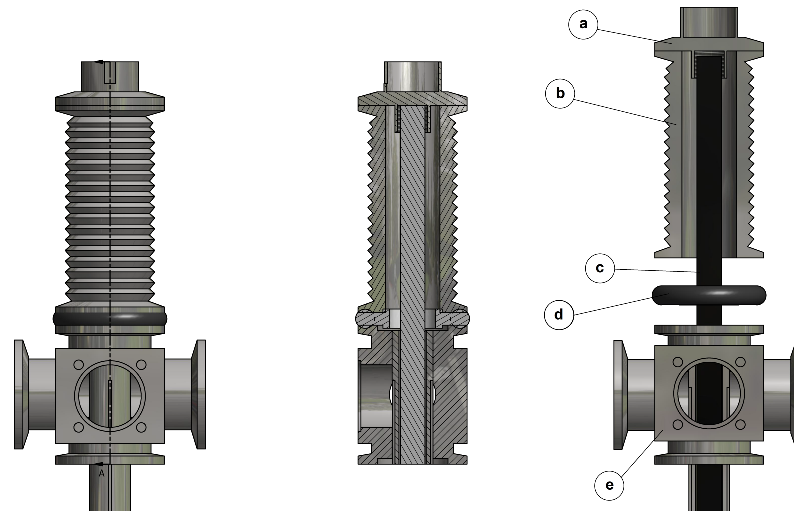

FIGURE 3.12: a) Force sensor housing. b)Bellows. c) Stainless steel rod. d) O-ring. e) connector block.

3.2.2 Stress applying module

The stress module consists of four main parts. A hydraulic system, a spring, plunger and housing.

Hydraulics

The stress probe is compatible with a number of different mechanisms through which external pressure can be applied. Depending on the application, and with some slight modifications, the user can choose to use free weights, levers, screw

jacks, pneumatics or other mechanical means. Here the stress module was designed to operate based on hydraulics. While hydraulic systems are generally more complex, they have certain advantages over their mechanical counterparts. Some of the advantages are:

- A single hydraulic system can be easily adjusted to produce the exact amount of stress required by specific experiments and does not require additional parts (weights, longer or shorter levers, etc.) to achieve this once it's fully setup.
- A wide variety of different hydraulic systems are readily available off the shelf, whereas mechanical systems need to be custom build that would make the end result more financially costly.
- Due to the smooth operation of hydraulic jacks, the chance of disturbing the balance of the system and the sample, in particular, is much lower due to low amount of stored energy.

The hydraulic system in this setup consists of a hydraulic cylinder and a manual hydraulic pump. As demonstrated in Figure 3.18 The pump is positioned away from the system so that when it is operated no direct physical contact is made with the rest of the system.

Spring and housing

Another component in the stress module is the spring and its housing as shown in Figure 3.13. The spring is added to the module to compensate for the constant

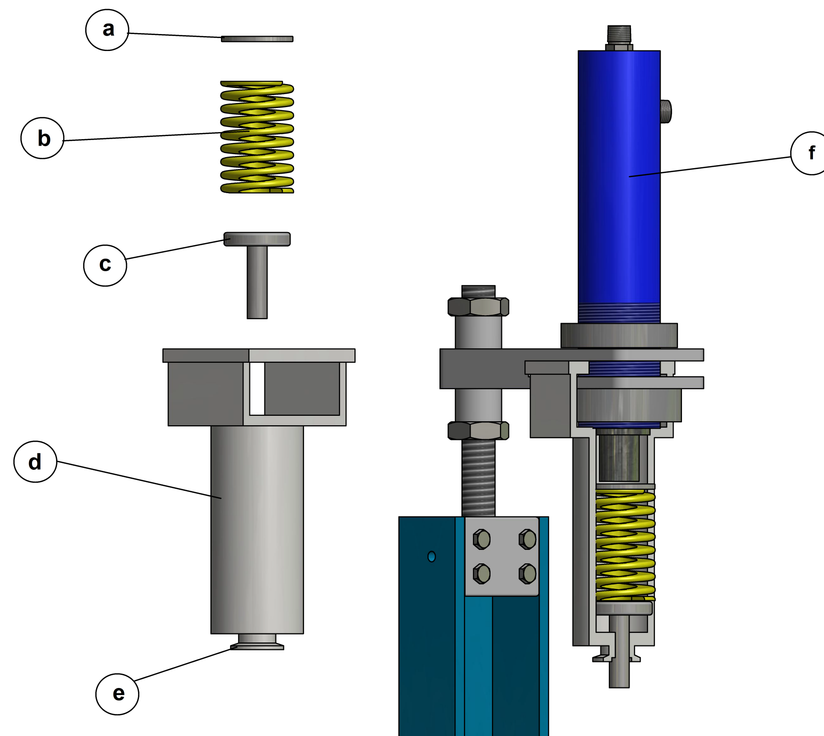

Figure 3.13: Stress module components. a) steel disk. b) Spring. c) Pusher. d) Spring enclosure. e) QF flange. f) Hydraulic cylinder.

stroke distance of the hydraulic jack. This allows the user to better control and adjust the amount of stress that is being put on the sample. Depending on the stiffness of the spring and its maximum deformation height, it is possible to set the system to operate within a minimum and a maximum pressure range.

Electrical connections

During measurements at low temperatures, a vacuum must be maintained within the cryostat, therefore all the electrical connections going from the sample holder to the outside, have to go through hermetically sealed connectors.

There are two main electrical leads that are connected to the sample, one on the

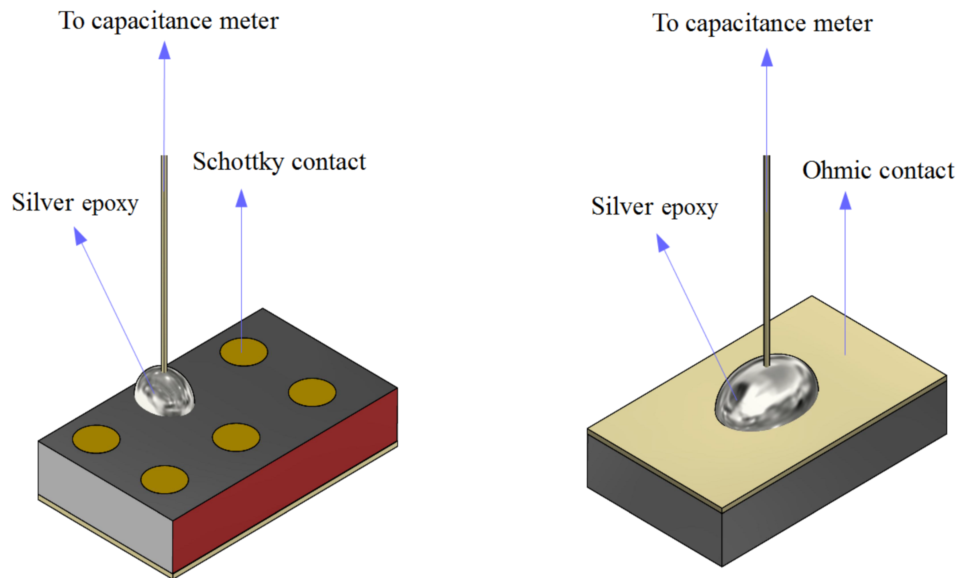

FIGURE 3.14: A representaiton of how a sample looks after the wire bonding process.

Schottky side and the other on the ohmic. Due to the delicate nature of the Schottky contacts and space limitation within the sample holder, conventional electrical probes such as beryllium-copper wires and pogo pins, cannot be used. The use of such methods for establishing electrical connections could lead to dislocation of the sample under stress or damaging the Schottky contact due to friction between the surface of the contact and the probe, both of which could jeopardize the measurements. Therefore, the method of choice for connecting samples to the rest of the circuitry, is a process known as *wire bonding*. Wire bonding is the process of attaching ultra-thin electrical wires to contacts, using permanent attachment methods such as conductive adhesive or ultrasonic soldering. Here, single drops of a silver-based conductive epoxy and gold wires were used for this purpose. Figure 3.14 shows how a sample will look after the wire bonding process.

After the completion of the wire bonding process, the sample is connected to the

circuitry by attaching the free ends of the gold wires to a pair of coaxial cables that are then connected to the input of the capacitance meter.

Other electrical connections that are necessary to complete the device are thermocouple wires and heater wires which are connected to the temperature controller through a circular MIL-DTL-5015 connector.

Clamps and fasteners

Fasteners are parts that keep the system together. They are not only responsible for connecting different parts of the system to each other, but also the stability of the device and the integrity and quality of the vacuum within the sample chamber, depend on them.

For high vacuum applications, specifically for systems that are modular, it is conventional to use standard flanges at the junctions where different parts meet. However, since there are a wide variety of different types of flanges available, certain criteria must be considered before choosing one. Firstly, the type of flanges used must be compatible with the existing parts of the system such as the cryostat. Secondly, the flanges and the fasteners that go with them must be robust enough to withstand the external stress without deforming. Thirdly, for junctions that need to be taken apart on a regular basis, using flanges and fasteners that do not rely on any permanent or semi-permanent attachment methods, is necessary.

Considering these criteria, the flange type that was chosen for this project is the *Quick Release* flange, or QF for short. QF type flanges, shown in Figure 3.15, are suitable for high vacuum applications and are convenient to work with. As

demonstrated in Figure 3.15, the appropriate fastener used with these flanges is a special type of clamp. These clamps are usually made out of aluminum or stainless steel.

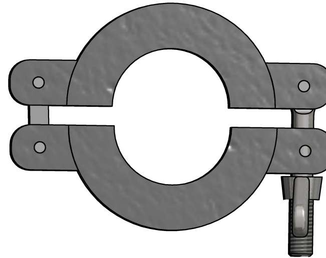

FIGURE 3.15: QF or KF clamp.

The setup demanded that one special fastener be designed for connecting the stress module to the probe. As it can be seen in Figure 3.16, this component can be thought of as two QF clamps attached to each other via two hollow semi-cylinders. The role of this special clamp is to ensure that all the generated stress is maintained within the stress module and the probe and that no excessive pressure is exerted on the cryostat or to the stand. Furthermore, it also acts as an enclosure for the bellows at the top of the probe to prevent it from buckling or dislodging under stress.

Frame and final assembly

Figure 3.17 demonstrates various parts of the stand while Figure 3.18 demonstrates how all the parts of the mechanical system are assembled.

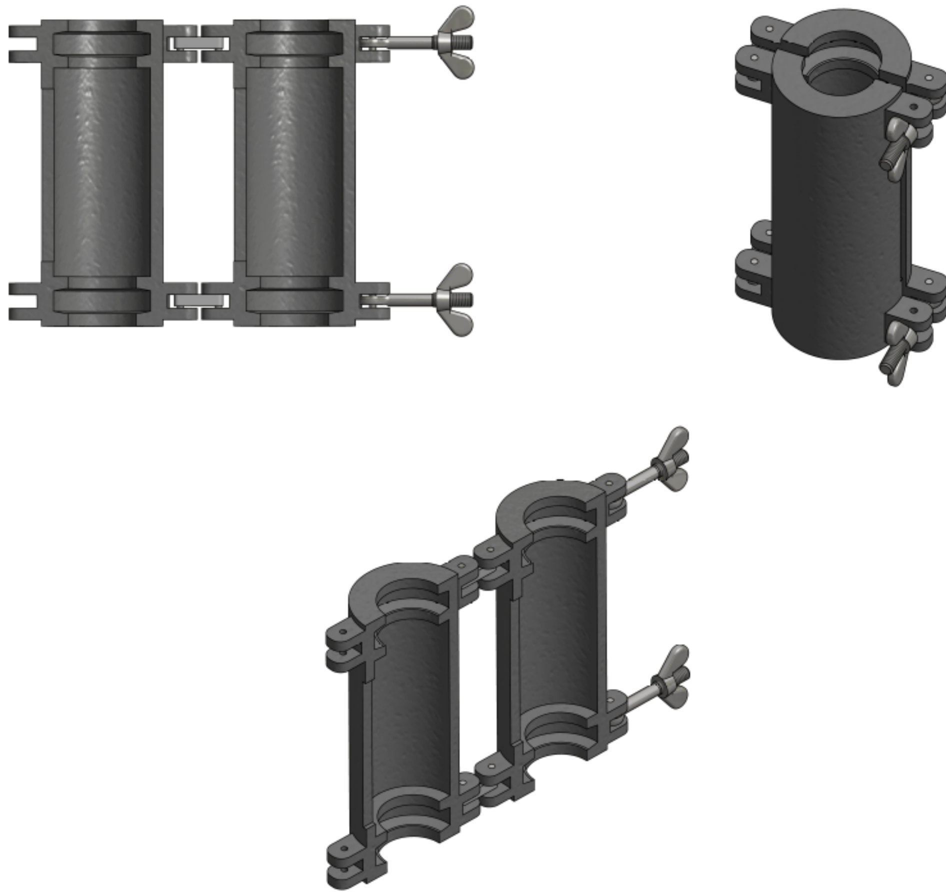

FIGURE 3.16: The special clamp that connects the probe to the stress module.

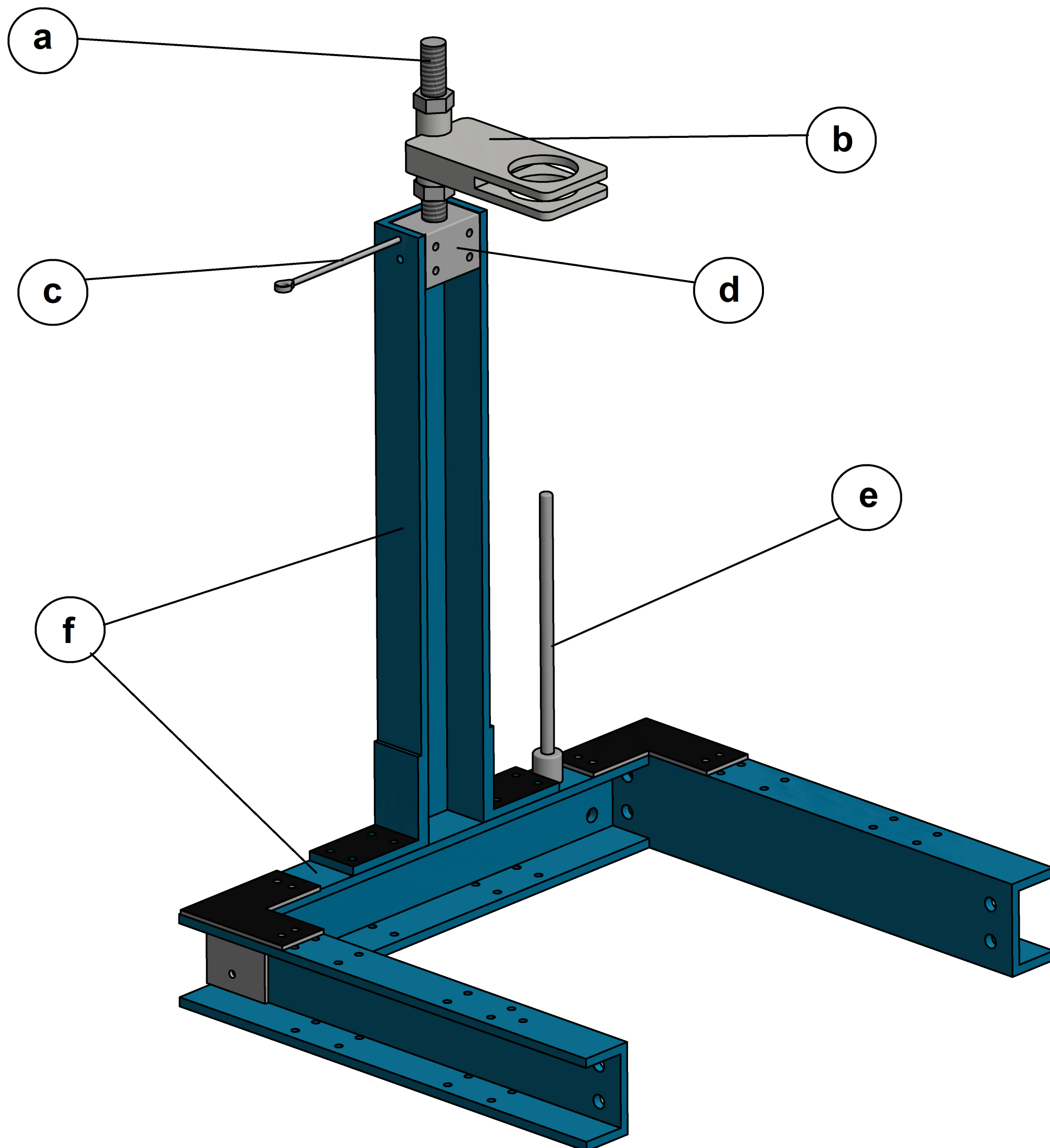

FIGURE 3.17: Stand. a) Threaded rod and nuts for adjusting the height of the hydraulic cylinder. b) special holder for holding both the hydraulic cylinder and the spring housing. c) Steel rod for holding liquid nitrogen reservoir. d) steel block for attaching the threaded rod to the frame. e) steel rod for attaching extra utilities. f) steel beams forming the frame.

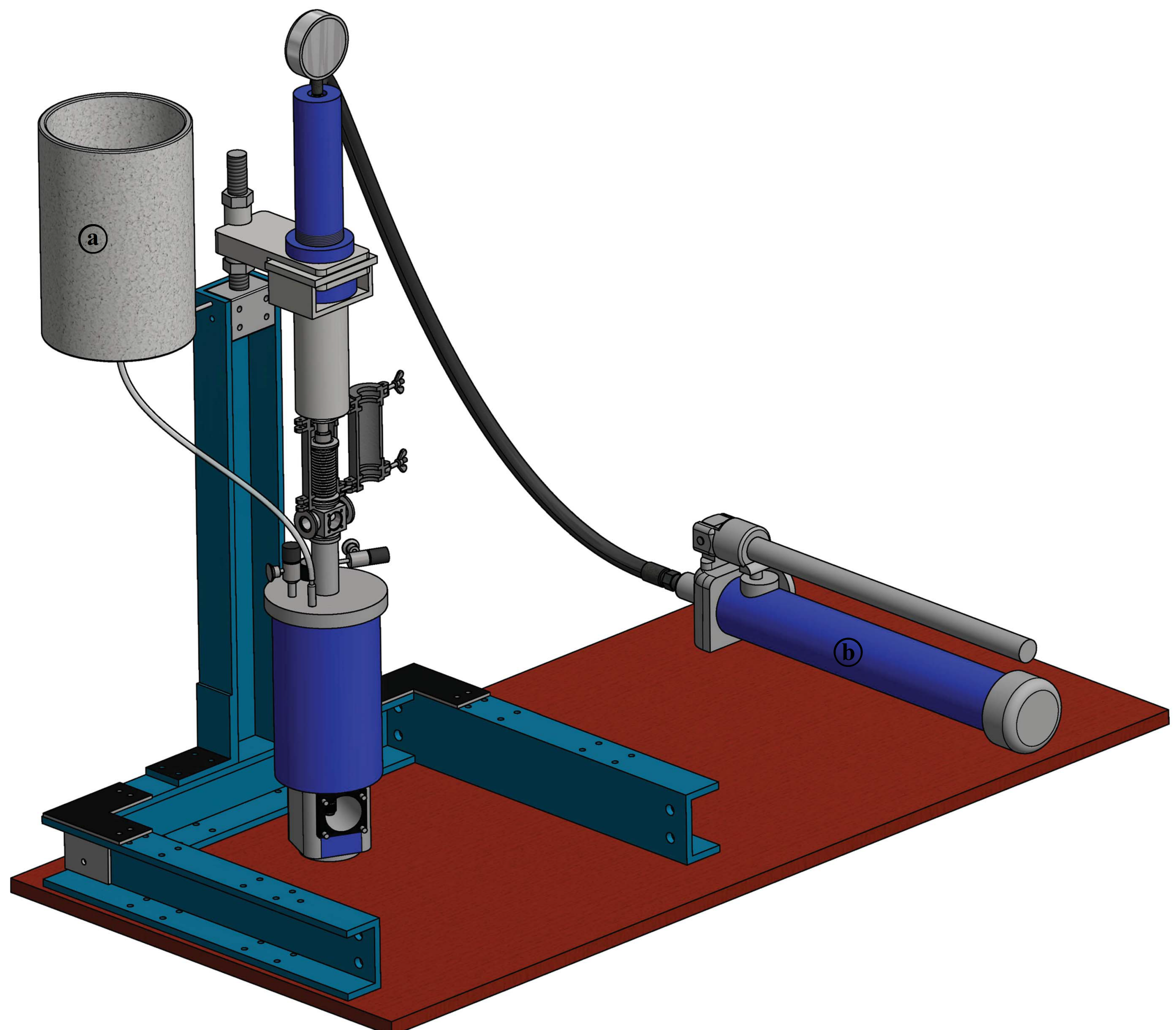

FIGURE 3.18: Complete mechanical components of the system. a) liquid nitrogen reservoir. b) Hydraulic hand pump.

Chapter 4

Experimental methods

4.1 Metal-semiconductor device fabrication

As it was discussed in Chapter 2, The operation of DLTS relies on the properties of metal-semiconductor contacts, specifically, Schottky barrier diodes. Therefore, to be able to characterize defects using DLTS, the material under study has to be made part of such a device. In general, these devices are prepared in the same fashion, however, depending on the material the sample preparation procedures are slightly different. Materials come in the form of wafers with various diameters, thicknesses and surface orientations. Therefore, the first step in preparing samples in cutting small parts of these wafers according to the requirements. For conventional and L-DLTS studies the surface and edge orientations and even the relative size of the sample are of little importance. However, for stress-dependent studies, these factors become fundamentally important. Normally, wafers are manufactured so that their surface orientation is (100) or (111). From such a wafer,

samples can be extracted so that their sides are along either [100] or [110]. This produces a limitation since, in order to draw definitive conclusions from stress dependence measurements, stress applied along major orientations must be studied. Ideally, a wafer with surface orientation of (110) is required, from which samples with all other major orientations can be extracted. Nevertheless, as it is quite difficult and somewhat expensive to secure such a wafer, the author was content to using (100) wafers for the sole purpose of demonstrating that the designed system operates properly and as planned.

4.1.1 Preparing the substrate

Gallium arsenide is one the few semiconductors that is easy to work with regards to preparation. It can be cleaved along various orientation lines and due to its softness, edges can be sanded using fine grit sandpaper in order to eliminate any rough or jagged edges that might lead to cracking when stress is applied. Therefore, it is a suitable material for testing the operation of the designed system.

Rectangular samples with dimensions 3.25 mm $\times$ 5.0 mm $\times$ 0.5 mm were cut from a silicon-doped (n-type), epitaxially-grown wafer with doping density of 1.1×10^{15} cm^{-3}, supplied by Spire LLC. The surface orientation of the wafer was reported to be (100).

These rectangular pieces were extracted according to Figure 4.1 by cleaving. As can be seen, both the long and short edges of the sample are perpendicular to the (110) axis and relative to each other with a minimal deviation.

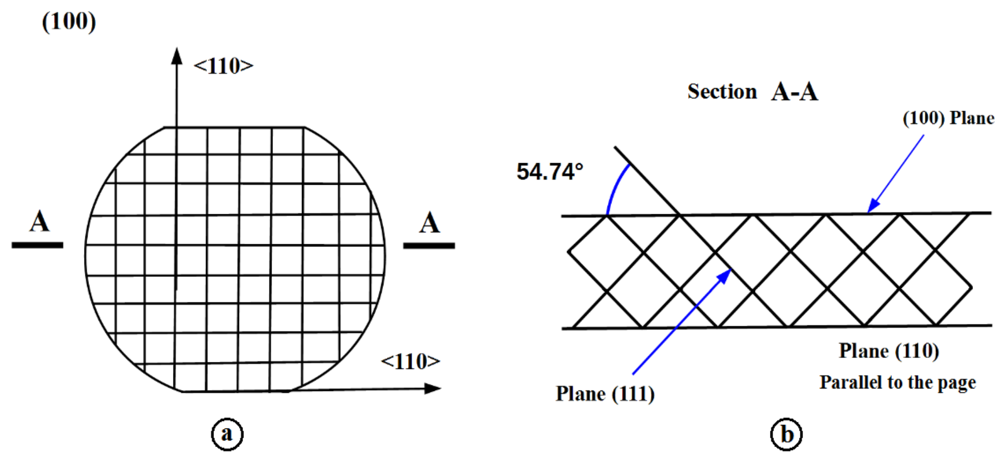

FIGURE 4.1: A wafer with (100) surface orientation. The lines in the figure indicate cleavage lines a), cross sectional view of the wafer showing the (100) and (110) planes b).

4.1.2 Cleaning procedure

Before metal-semiconductor contacts can be deposited onto the substrates, a meticulous cleaning procedure has to be followed to clean the surfaces of any contaminants and also etch these surfaces, ensuring that once metals are deposited, they are in intimate contact with the semiconductor substrate.

Of the two primary etching procedures, namely, dry etching and wet etching, the latter was used in this experiment. Wet etching has the advantage of producing the least amount of surface damage and therefore does not induce the creation of new defects.

In wet etching, each material requires the use of certain chemicals and procedures. The cleaning procedure for GaAs as explained by Baca et al. (1997) and Goodman (1994) is as follows:

Degreasing

1. Substrates were agitated in trichloroethene for 3 minutes
2. Substrates were agitated in isopropanol for 3 minutes
3. Substrates were given three consecutive rinses in de-ionized water to remove the isopropanol.

Etching

1. First etching process was carried out by dipping the substrates in boiling solution of $H_2O : H_2O_2 : NH_4OH$ with the ratio 100: 1: 3 for 30 seconds.
2. Substrates were then given a fourth rinse in de-ionized water.
3. Second etching process was carried out by dipping the substrates in 10 ml of 38% aqueous solution of HCl for 2 minutes.
4. After a final rinse in de-ionized water substrates were blow dried using nitrogen gas.

4.1.3 Schottky and ohmic contacts

Ohmic contact

After the cleaning procedure, the samples were ready for deposition of the ohmic contact. Au based alloys are the most commonly used contacts for GaAs due to their excellent contact resistivity (Baca et al., 1997). In this study the Ni/AuGe/Ni contact was used. To start the deposition process, samples were secured in a special

sample holder and placed in the vacuum chamber of a resistive deposition system. The chamber was evacuated down to a pressure of 1×10^{-7} mbar. Firstly, a 6 nm layer of Ni was deposited on the n^+ surface of the substrate followed by an 80 nm layer of Au:Ge and finally a second 30 nm layer of Ni. The metal-semiconductor contact was then annealed at 450°C in an Ar atmosphere for 2 minutes.

Schottky contact

Before depositing the Schottky contacts, the substrates were put through the previously explained cleaning procedure for ohmic contacts omitting the etching step. After the cleaning, substrates were secured to a special sample holder and placed in the same vacuum system as used for ohmic contacts. A layer of high purity Au was deposited through a metal mask onto the free surface of the substrate, forming circular Schottky contacts with 0.6 mm in diameter. No annealing was performed after this step.

A cross sectional view of the sample after the ohmic and Schottky contacts were created can be seen in Figure 4.2.

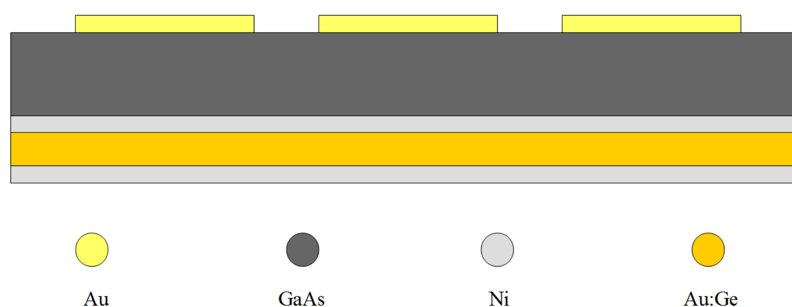

FIGURE 4.2: Cross sectional view of the Schottky and ohmic contacts on a GaAs substrate. The thicknesses of the contacts are exaggerated.

4.2 Defect introduction by beta particles

After a suitable sample was created, it was subjected to beta particle irradiation using a ^{90}Sr radionuclide. Electrons emitted from this source have energy levels in the range of 100- 2000 keV and the flux associated with our source is 6×10^9 cm^{-2}s^{-1}. The sample was placed underneath the source so that the side with the Schottky contacts was exposed to the incoming radiation. The distance between the surface of the sample and the source was less than 0.3 mm. The sample was irradiated for 3.5 hours at room temperature (297 K).

4.3 Characterization techniques

4.3.1 IV/CV measurements

Current-voltage (I-V) and capacitance-voltage (C-V) measurements are standard characterization techniques that provide important information regarding the properties of Schottky barrier diodes. Information such as ideality factor (n), barrier height (ϕ_{iv}) and series resistance of the device can be determined from I-V measurements while carrier concentration is determined by C-V measurements. The I-V/C-V station consists of a computer, running *LabVIEW*, an HP4140B DC/AC pA meter and voltage source, and an HP4149A impedance analyzer. The sample is positioned in a dark environment and is connected to the aforementioned devices via adjustable probes. Figure 4.3 demonstrates how the probes are connected to the sample.

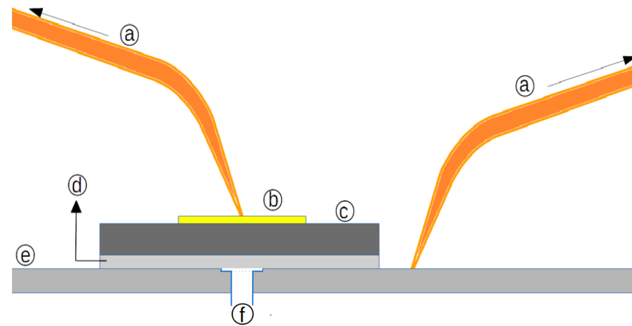

Figure 4.3: Representation of the sample and how it is set up in the I-V/C-V station, showing the the probes (a), the Schottky contact (b), the substrate (c), the ohmic contact (d), conductive surface (e), the Vacuum pump intake (f). The purpose of the vacuum pump is to secure the sample in place while the probe is being connected to the Schottky contact.

4.3.2 DLTS measurements

Both the conventional and LDLTS measurements were carried out by utilizing the same hardware. The design and function of the digital DLTS system are described fully by Meyer (2006). The system consists of:

- A closed-cycle helium-cooled cryostat that houses the sample and allows for precise temperature control during measurements.
- A vacuum pump for evacuation of the sample chamber.
- A temperature controller (Lakeshore 332) that monitors and adjusts the temperature of the sample.
- A computer running *LabVIEW* and the *Transient Processor* software.
- A *National Instrument* data acquisition (DAQ) card with built-in pulse generation functionality, an I/O block and a *GPIB* with an IEEE 488 and USB connections.

- A capacitance meter (Boonton 7200) that monitors the change in capacitance of the diode during emission of electrons from traps.
- A capacitor selection box that allows the use of smaller measurement scales.

The arrangement of these instruments can be seen in Figure 4.4.

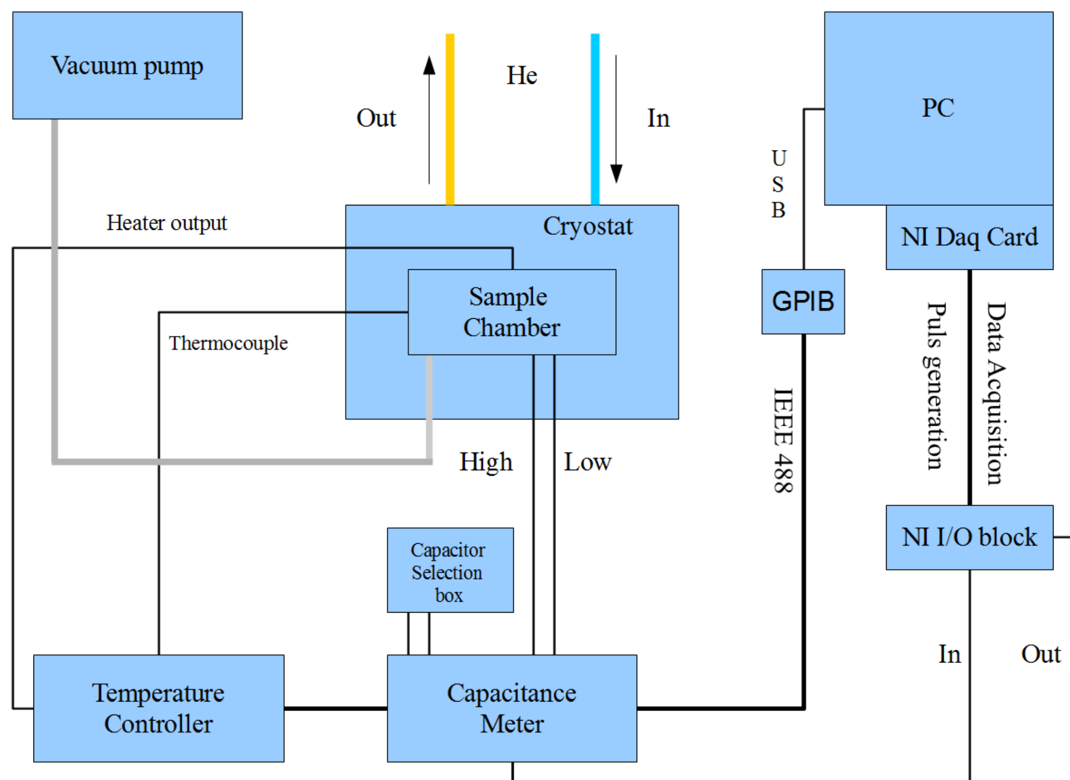

FIGURE 4.4: Schematic diagram of a DLTS system.

4.3.2.1 Determining the presence of the E2 defect using conventional DLTS

Conventional DLTS measurements were used to demonstrate the presence of the E2 defect after the 3.5-hour irradiation of the sample. For this measurement, the rate window was selected to be between 80 s^{-1} and 200 s^{-1}. The temperature

range was set to 25-300 K. The reverse bias condition was selected to be -2 V and the capacitance measurements were performed in the 2 pF scale.

4.3.2.2 Electrical characterization of the E2 defect using Laplace DLTS

Activation energy

A series of LDLTS measurements were taken to determine the activation energy and the electric field dependence of the E2 defect. The activation energy of the defect (E_T) is determined through observation of the temperature dependence of the emission rate of the defect at constant bias conditions. Using this data, an Arrhenius plot (ln of emission rate as a function of $1/T$) can be drawn and the energy can be calculated from it.

Electric field dependence

The electric field dependence of the defect is determined through observation of the enhancement of the emission rate as a function of the magnitude of the applied field. This is an isothermal measurement and the electric field experienced by the defect is the field in the depletion region due to the reverse bias V_R. By increasing the magnitude of this electric field (i.e. by increasing the reverse bias), an enhancement of the emission rate from the defect is observed as a shift in the position of the peak(s) in the LDLTS spectrum. The level of enhancement as a function of the magnitude of the electric field can then be used to determine the shape of the well (indicating the charge state of the defect involved) as well as the dominant mechanism by which charge carriers are emitted from a trap.

The electric field is not homogeneous across the depletion region and changes from a maximum value at the junction to a minimum value at the depletion region edge resulting in otherwise identical deep levels in this region to experience different fields. Since the magnitude of the electric field determines the level of enhancement of the emission rate of the defect, the deep levels experiencing higher fields will have faster emission rates and vice versa. This, in turn, results in broadening of the peak associated with a single defect. If present, this effect can interfere with the validity of the results obtained from uniaxial-stress DLTS measurements and therefore must be minimized. Figure 5.5 demonstrates how the magnitude of the electric field can cause broadening of a peak.

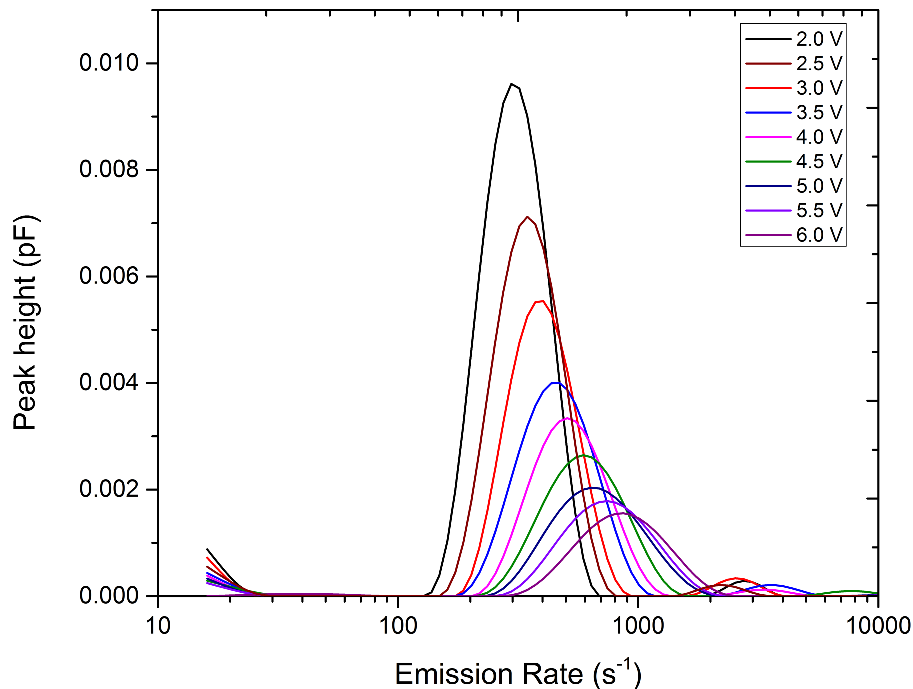

FIGURE 4.5: Electric field dependence of the E2 defect in GaAs. The rightwards shift and the broadening of the peaks as a function of the magnitude of the electric field. Measurement conditions: T = 270 K, second pulse bias = −0.2 V, first and second pulse widths = 1 ms, sampling rate = 91 kHz, number of samples = 4000, number of scans = 6000.

To minimize the effects of this phenomena, the initial reverse bias V_R, must be set to the lowest possible value, thereby, narrowing the depletion region and reducing the electric field gradient across the region. Furthermore, it is possible to observe the emission process from an ever narrower section of the depletion region. This can be accomplished by applying two different filling pulses and subtracting the measured signals from each other. If the two pulse voltages are only slightly different, the resulting signal will show only a very narrow section of the depletion region, across which the magnitude of the applied electric field can be considered to be constant (Dobaczewski et al., 1994).

In our experiments, the reverse bias V_R was set to -0.5 V and the filling pulse was set to 0.49 V. The secondary filling pulse was set to -0.3 V to further narrow the measured section of the depletion region.

4.4 Uniaxial-stress dependent DLTS

The design and function of the stress inducing and measurement part of the uniaxial-stress DLTS system are presented in Chapter 3. The DLTS part of the system is similar to the details given in Section 4.3.2 with one significant difference: The cryostat used in the uniaxial-stress DLTS system is a liquid-nitrogen-cooled cryostat capable of operating in the temperature range of 78 - 500 K. For practical reasons concerning the use of such cryostats, the measurement temperature was chosen to be 78 K where the E2 defect is measurable, but no heating or temperature controlling loops were needed.

Before samples were mounted onto the sample holder, the wire bonding process, discussed in Section 3.2.1, was performed. Figure 4.6 demonstrates the procedure. After thin gold wires were bonded to both the ohmic and Schottky contacts, the sample was placed in the sample holder of the system.

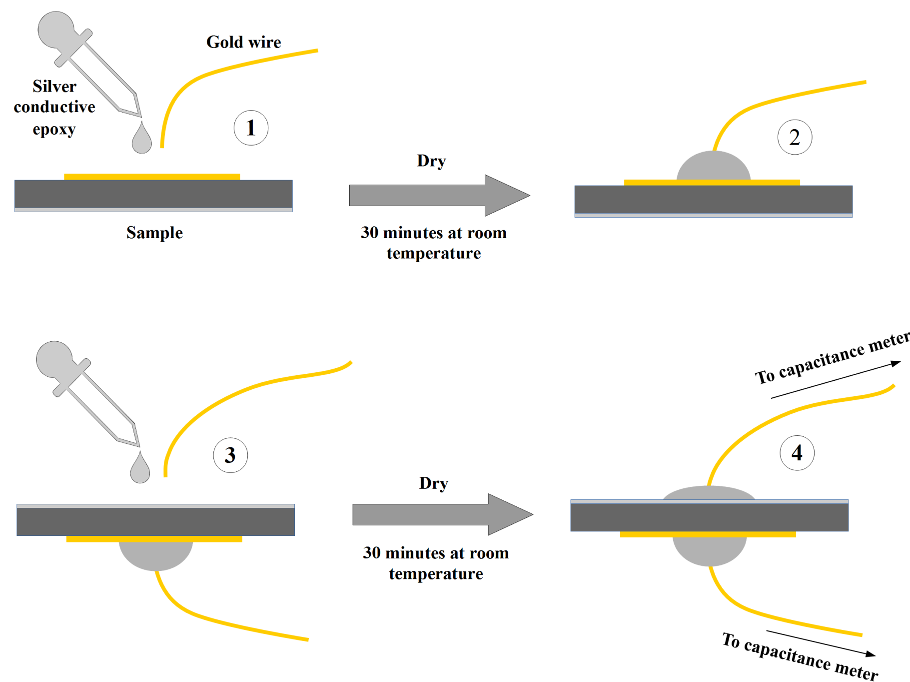

FIGURE 4.6: Demonstration of the wire bonding process.

To reduce the friction between the metallic parts of the sample holder and the edges of the sample, thin cardboard pieces were placed on either side of the sample, cushioning and protecting them against cracking. The thickness of the cardboard was experimentally chosen so there would be minimal interference with the heat transfer between the sample holder and the sample while still provided proper protection.

The sample holder was then placed in its enclosure and the probe was inserted into the sample chamber of the cryostat. With the probe in place, other mechanical

and electrical connections were attached and the cryostat was filled with liquid nitrogen. When the temperature stabilized at 77 $\pm$ 2.88 K, multiple measurements were taken with the sample under 0 N and subsequently at 20 $\pm$ 0.16 N, 40 $\pm$ 0.16 N, 60 $\pm$ 0.16 N, 80 $\pm$ 0.16 N, 100 $\pm$ 0.16 N, 120 $\pm$ 0.16 N, 140 $\pm$ 0.16 N, 160 $\pm$ 0.16 N, 180 $\pm$ 0.16 N, 210 $\pm$ 0.16 N, 240 $\pm$ 0.16 N, 300 $\pm$ 0.16 N. Considering the sizes and shape of the sample and the surface under stress, these values correspond to 0.012 $\pm 9.8 \times 10^{-5}$ GPa, 0.025 $\pm 9.8 \times 10^{-5}$ GPa, 0.037 $\pm 9.8 \times 10^{-5}$ GPa, 0.049 $\pm 9.8 \times 10^{-5}$ GPa, 0.061 $\pm 9.8 \times 10^{-5}$ GPa, 0.074 $\pm 9.8 \times 10^{-5}$ GPa, 0.086 $\pm 9.8 \times 10^{-5}$ GPa, 0.098 $\pm 9.8 \times 10^{-5}$ GPa, 0.11 $\pm 9.8 \times 10^{-5}$ GPa, 0.13 $\pm 9.8 \times 10^{-5}$ GPa, 0.15 $\pm 9.8 \times 10^{-5}$ GPa, 0.18 $\pm 9.8 \times 10^{-5}$ GPa respectively.

Chapter 5

Results and discussions

The aim of this chapter is to present and discuss the operation of the uniaxial-stress DLTS system by comparing the results obtained with a similar study by Hartnett and Palmer (1997). In order to determine whether the results are directly related to the applied uniaxial stress or are brought about by other effects, a series of tests were performed before and after the stress measurements on the sample. Firstly, it was necessary to make sure that the sample as a diode had the proper properties for this type of measurements. Hence, the I-V and C-V measurements presented in Section 5.1.

Secondly, a conventional DLTS scan was performed to determine the existence and density of the E2 defect after irradiation by beta particles. After identifying the E2 peak in the DLTS spectra, we proceeded to perform LDLTS scans over a range of temperatures to obtain the *DLTS signature* of the defect (activation energy and the apparent capture cross section) and matched the results to previously

published data. This was an extra step to ensure that the defect under study was in fact the E2 defect. These results are presented in section 5.2.

Furthermore, since the emission rate of a defect can be influenced by the electric field applied across the sample due to the a reverse bias, it was necessary to perform an electric field dependence study of the defect at the exact same temperature where the stress measurements were to take place. The results are presented in Section 5.3 in the form of an emission rate enhancement plot.

5.1 I-V and C-V

To determine the device characteristics of our diode, general I-V and C-V measurements were performed on the sample, after it was irradiated. The results of the room-temperature I-V and C-V measurements for the Au Schottky contacts are shown in Figure 5.2. Table 5.1, demonstrates the important I-V characteristics of the SBD.

As stated in Table 5.1, the ideality factor of the Schottky barrier diode, n, was determined to be 1.07, slightly deviant from unity but still acceptable for DLTS measurements. The series resistance R_s was also acceptable for DLTS measurements (the resistance of the capacitor that was larger than the series resistance of the sample). The saturation current I_s and the Schottky barrier heigh ϕ_{IV} both had optimal values.

Figure 5.3 shows a conventional DLTS scan of the sample after irradiation with electrons. The scan was performed over a temperature range of 20 to 300 K where

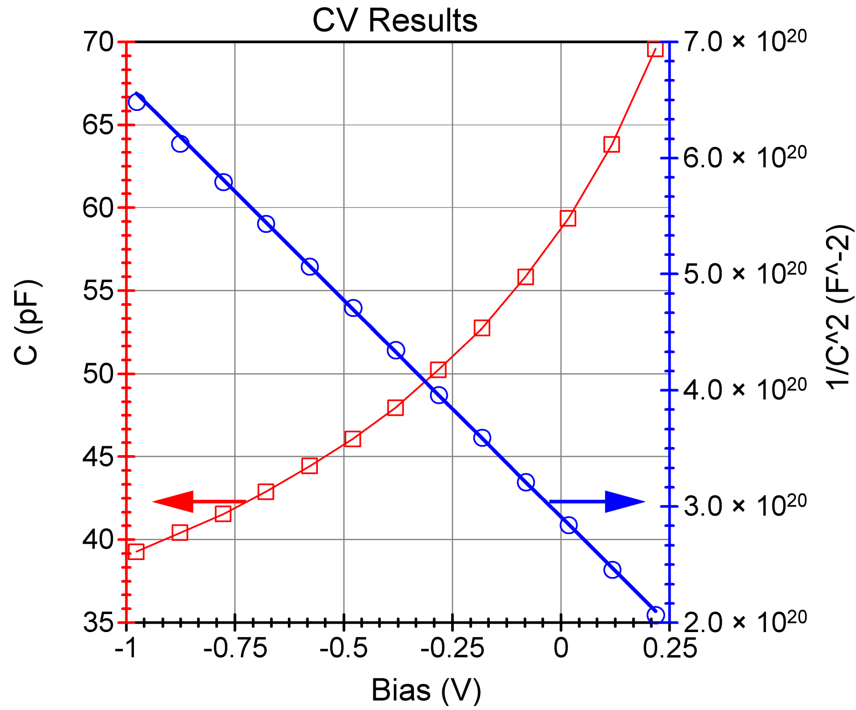

FIGURE 5.1: The C-V graphs of the SBD.

Free carrier concentration, N_D (cm^{-3})	1.1 x 10^{15} cm^{-3}
C-V barrier height, ϕ_{CV} (eV)	1.003 eV
V_{bi}, (V)	0.755 V

TABLE 5.1: Important I-V characteristics of the SBD.

Ideality factor, (n)	1.07
Saturation current, I_s (A)	4.28 x 10^{-12} A
Schottky barrier height, ϕ_{IV} (eV)	0.880 eV
Series resistance, R_S (Ω)	38 Ω

TABLE 5.2: C-V characteristics of the SBD.

three electron traps, including the E2 defect, are visible. The measurement was performed under the following conditions: V_R = -2 V. Second pulse bias = −0.5 V. Rate window = 80 s^{-1}. First and second pulse width = 1 ms. The T_P (the temperature at which the DLTS peak is observed for a defect) values for E1, E2 and E3 were measured at 32 K, 74.5 K and 204 K respectively.

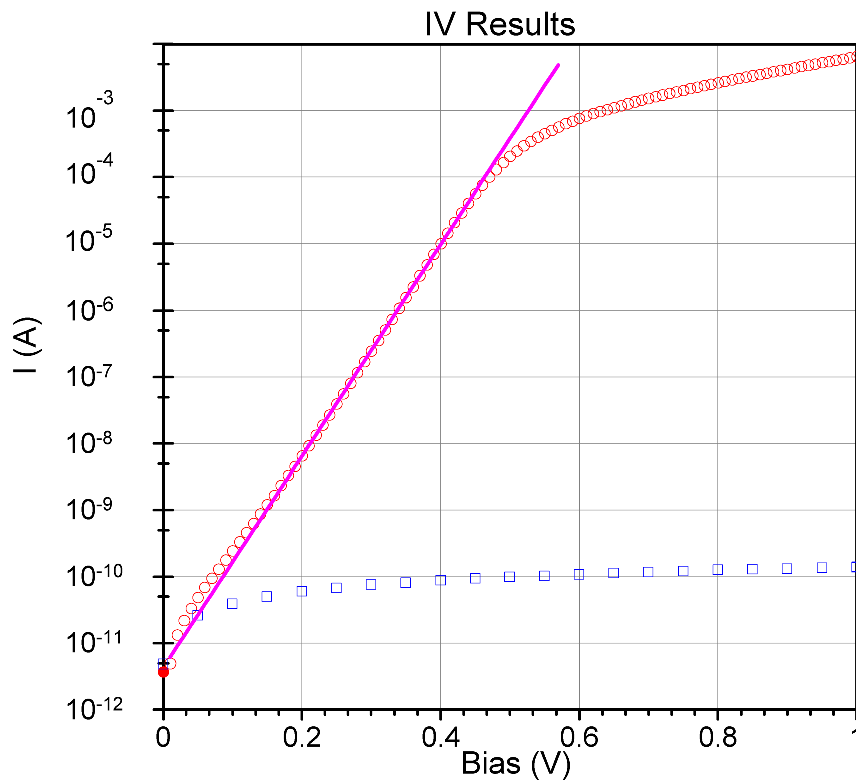

FIGURE 5.2: The I-V graphs of the SBD.

5.2 Activation energy

Using the data from a series of LDLTS scans that were performed over a temperature range of 72 - 88 K, an Arrhenius graph of $\log[T^2/e]$ as a function of $1000/T$ was plotted. From the Arrhenius plot, the activation energy of the E2 defect was calculated to be $E_T = 0.136 \pm 0.001$ eV below the conduction band. The result was in agreement with the previously published values for this defect (Auret et al., 1993) (Pons and Bourgoin, 1985).

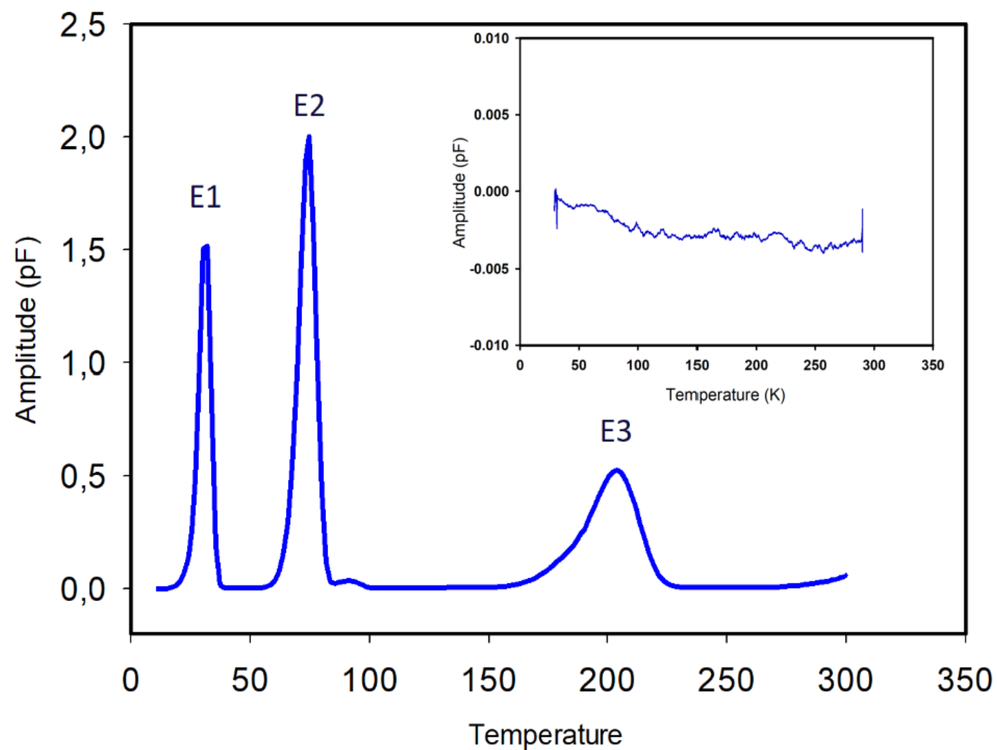

FIGURE 5.3: A conventional DLTS scan showing the dominant electron traps in the sample. The sample was irradiated for 3.5 hours with MeV electrons. Measurements were performed in the reference DLTS system that utilizes a helium-cooled cryostat. Measurement conditions: $V_R = -2$ V. First pulse bias $= -0.5$ V. Rate window = 80 s^{-1}. First and second pulse width = 1 ms. The inset graph illustrates the spectrum prior to irradiation. Note that the scale for the amplitude of the inset graph is selected to be between -0.01 pF and 0.01 pF.

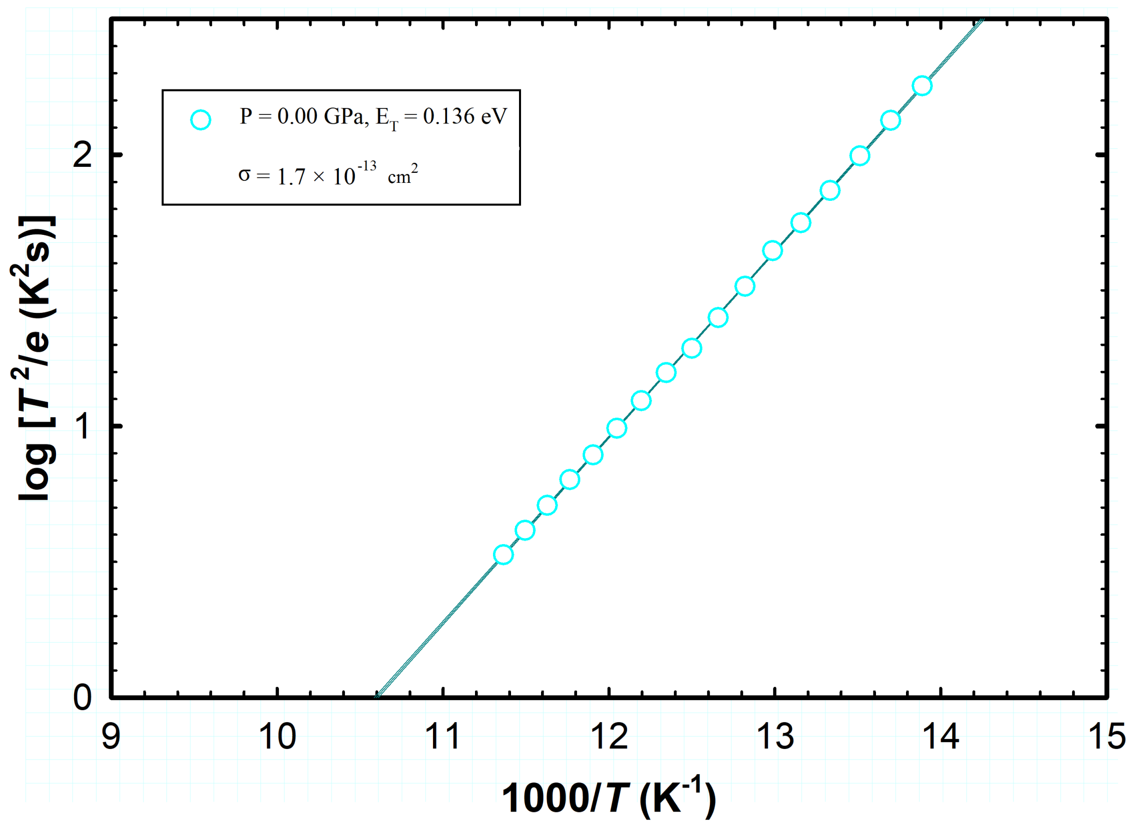

FIGURE 5.4: Arrhenius plot for the E2 defect. These measurements were performed in the reference DLTS system. LDLTS measurement conditions: T = 77 ± 1 K, $V_R = -2$ V, first pulse bias = −0.5 V, second pulse bias = −0.2 V, first and second pulse widths = 1 ms, sampling rate = 90 kHz, number of samples = 5000, number of scans = 4000.

5.3 Electric field dependence

The electric field dependence of the E2 defect was investigated using Laplace DLTS. The scans were performed at a constant temperature of $T = 78$ K while the electric field was gradually increased with each scan. The electric field was applied to the sample in the form of a reverse bias. Figure 5.5 demonstrates the effects of the electric field on the emission rate of the E2 defect. There is a noticeable rightwards shift in the position of the peaks as well as considerable broadening of the peak. This enhancement of the emission rate is proportional to the magnitude of the applied field. The rightwards shift indicates that as the magnitude of the field increased, there was an increase in the emission rate of the defect. The broadening of the peak was discussed in Section 4.3.2.2.

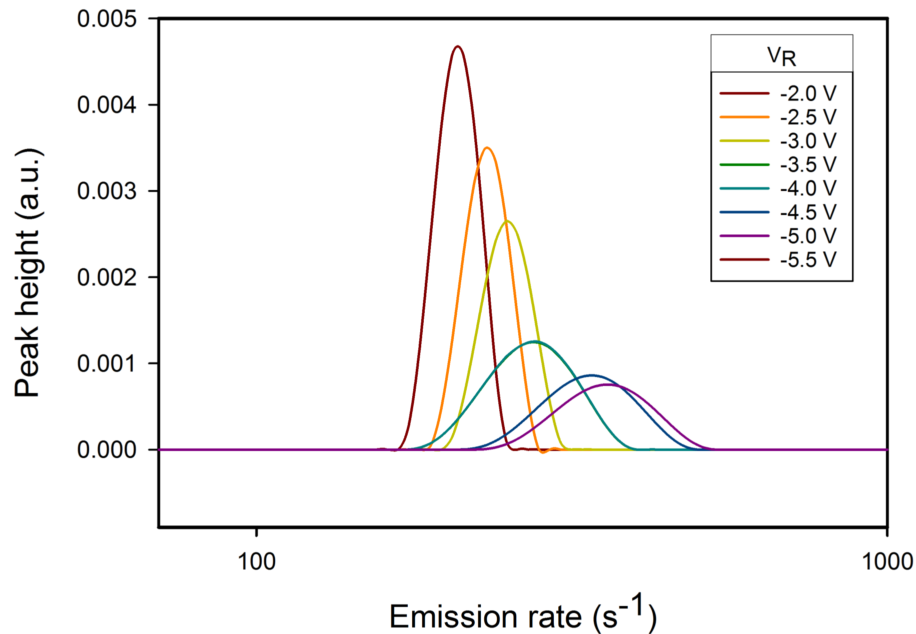

FIGURE 5.5: Broadening of the emission rate peak of the E2 defect due to electric field effect. LDLTS measurement conditions: T = 78 K, $V_R = -2$ V, filling pulse = +2 V, second pulse bias = −0.2 V, first and second pulse widths = 1 ms, sampling rate = 77 kHz, number of samples = 4000, number of scans = 4000.

5.4 Uniaxial-stress measurements

Figure 5.6 shows the LDLTS spectrum of the sample under variable uniaxial stress along the (110) orientation and at 77 K. From the figure, it can be observed that as the magnitude of the uniaxial stress increases, the peak begins to broaden and eventually splits into two peaks. There is also a slight leftwards shift in the position of each peak compared to the initial position (when no stress is applied to the sample). This shift suggests a decrease in the emission rate as a function of the applied stress. Figure 5.7 shows the transition from 0.000 GPa to 0.18 GPa. From 0.000 to 0.03 GPa there is little to no broadening and only a slight shift in the position of the peak is visible. From 0.05 to 0.07 GPa both the leftwards shift and considerable broadening is observable. From 0.12 to 0.18 GPa, the broadening of the peak is dominant with little leftwards shift. and at 0.18 GPa the splitting of the peak into two components is seen.

As it was discussed in Section 5.3, applying a large enough electric field to the junction can result in observation of shifts and broadening of the emission rate spectra of a defect. However, results of our stress-dependent studies show a significant difference between the two. While the emission rate of the defect increases as a function of the magnitude of the electric field, under uniaxial stress the emission rate decreased. Therefore, it is safe to assume that the effects observed under uniaxial stress, are solely stress-dependent and not influenced by electric field effects.

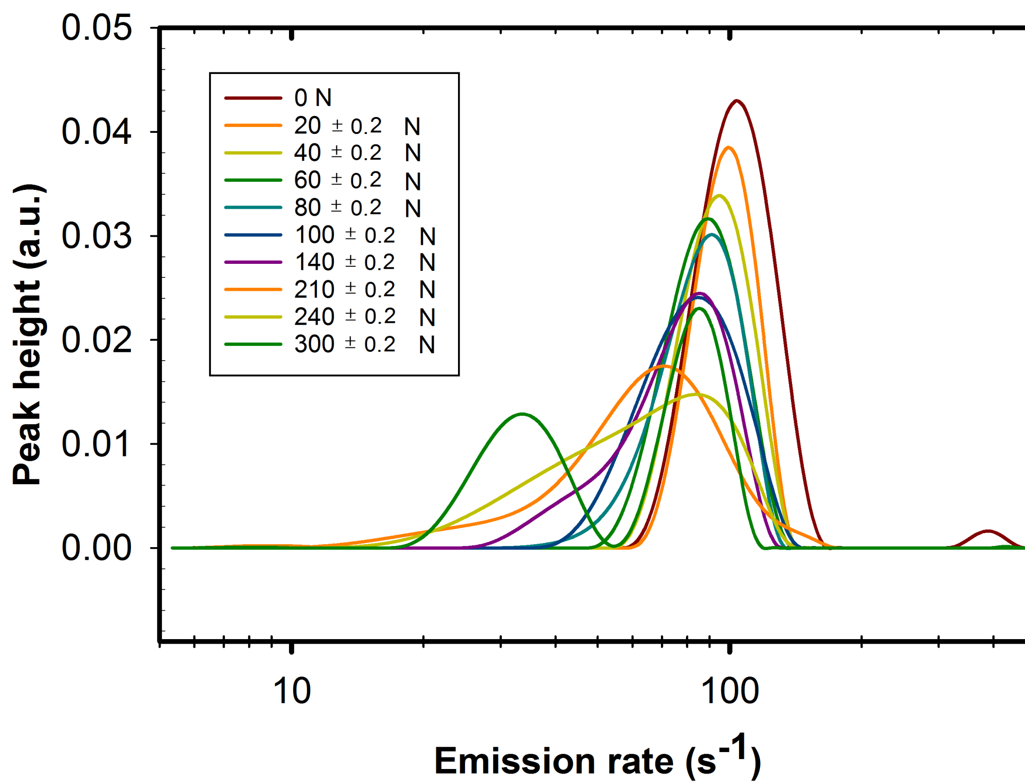

FIGURE 5.6: Splitting of the emission rate of E2 under uniaxial-stress along the [110] orientation. LDLTS measurement conditions: T = 77 ± 1 K, $V_R = -0.5$ V, filling pulse = +0.5 V, second pulse bias = −0.3 V, first and second pulse widths = 1 ms, sampling rate = 96 kHz, number of samples = 10000, number of scans = 3000. The regularization parameters for resolving the inverse Laplace transform were automatically chosen by the Laplace transient Processor.

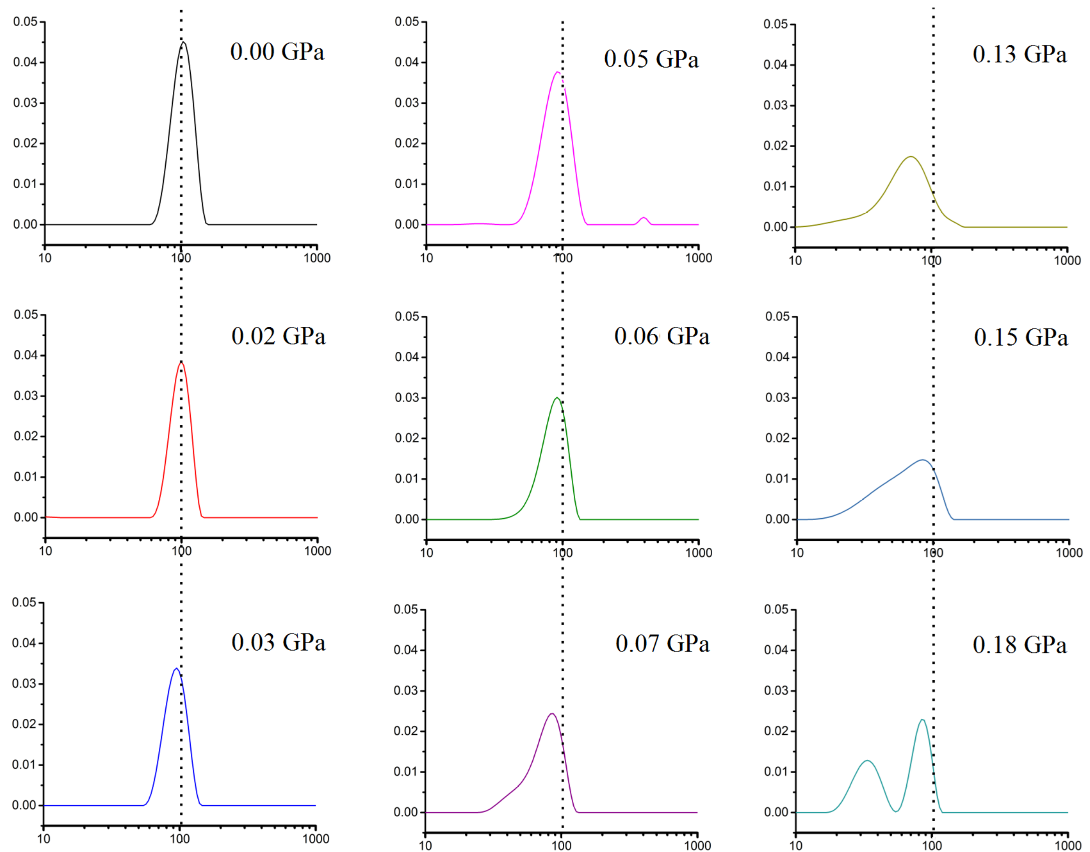

FIGURE 5.7: Individual curves from Figure 5.6, Showing the progression of the emission rate peak splitting under uniaxial stress. The horizontal axes determines the emission rate (s^-1), while the vertical axes is the DLTS signal (a.u.).

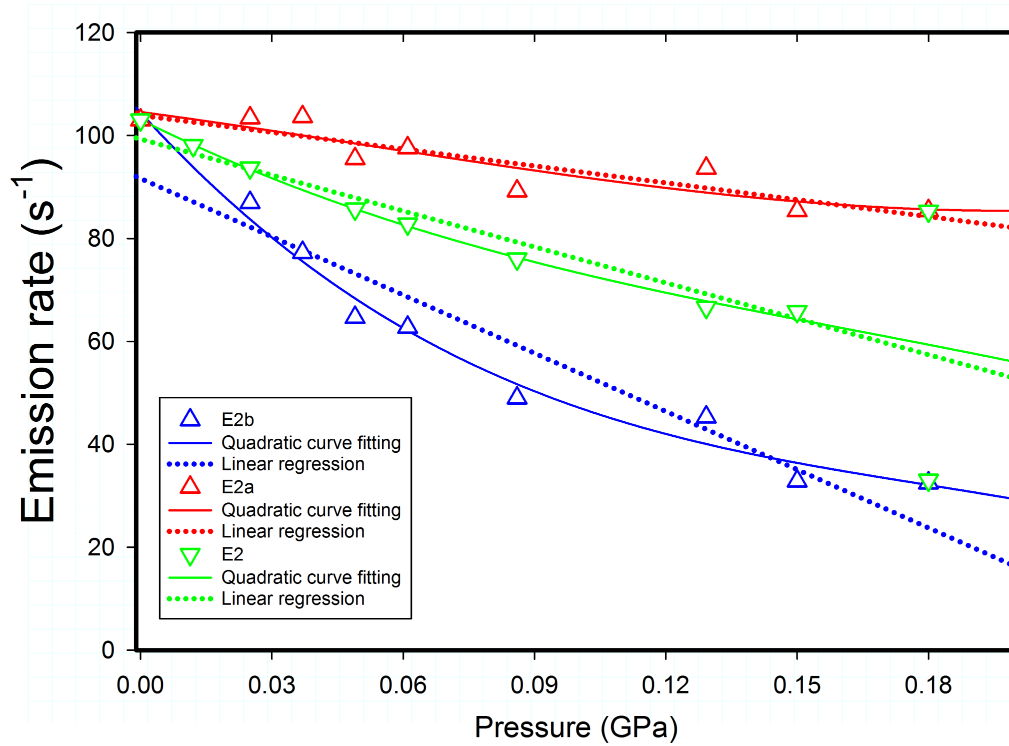

FIGURE 5.8: Plot of emission rate as a function of applied pressure at T= 77 K. The data in green is obtained from the data in Figure 5.6, however, for the blue and red plots the regularization parameters were manually set in order to better separate the peaks corresponding to each component (the blue and red points).

In order to determine the change in energy as a function of the applied stress, the following equation was used (Londos and Pavelka, 1990):

$$\Delta E = kT \ln \left(e_n / e_n(P)\right) \tag{5.1}$$

Where, e_n is the emission rate of the defect under zero stress and $e_n(P)$ is the emission rate under pressure P.

From Figures 5.8 and 5.9, it can be concluded that if optimal parameters are chosen for resolving the inverse Laplace transform, LDLTS can be used to detect minute changes in the properties of the defect when such information is critical.

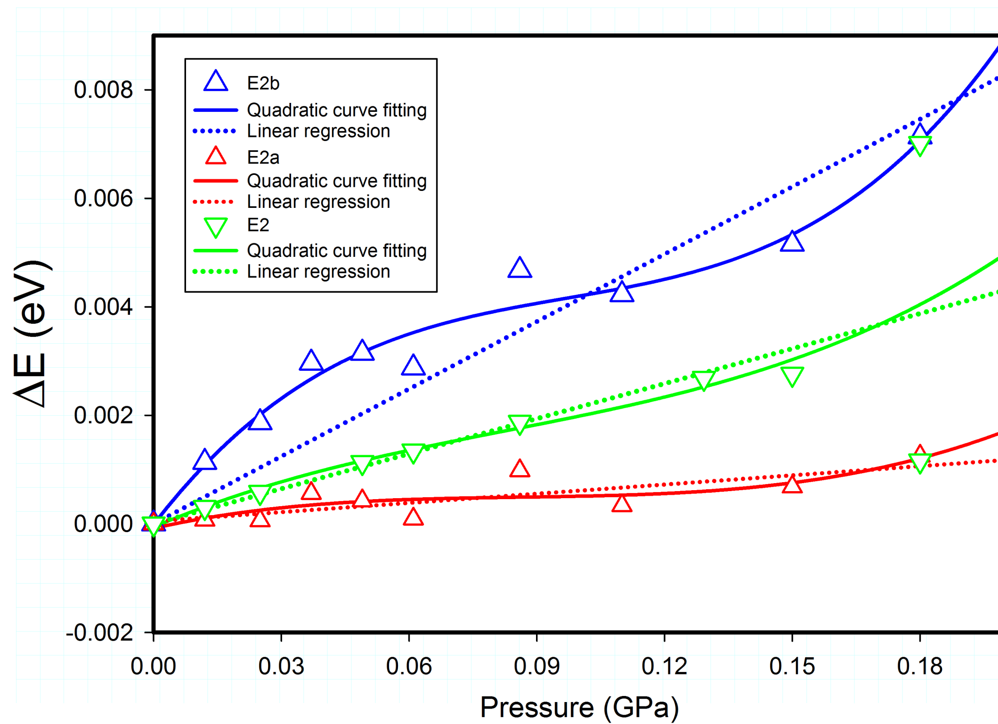

FIGURE 5.9: Plot of ΔE as a function of pressure. Similar to Figure 5.8, the green data points correspond to the data presented in Figure 5.6. The blue and red data points correspond to the effects of the applied pressure on individual components.

Furthermore, it can be seen that the stress dependence of the E2 defect might be non-linear. However, in order to draw such conclusion, we must consider the fact that both the emission rate and the calculated ΔE are temperature dependent and therefore small discrepancies in temperature measurements may drastically affect both graphs.

In any case, Figures 5.8 and 5.9 show that our system is capable of performing measurements even at low levels of stress which can be beneficial when working with soft or brittle semiconductor samples.

5.4.1 Arrhenius plots

Figure 5.10 shows the data points measured at 77 K. Here, the capture cross section for all the lines are predetermined and its value is set to 1.7×10^{-13} cm^2 which us the value measured under zero-stress conditions. From the figure it can be seen that the value of the emission rate of the unstressed sample in the stress DLTS system differed from those measured in the reference DLTS system. While using the stress DLTS system, measurements at 77 K were done by submerging the sample and the sample holder in liquid nitrogen. It is therefore unlikely that this shift is due to a temperature difference between the two systems. One reason for why there is a difference between what the stress system measures compared to the other system, is that even under "zero stress" conditions, there is some stress on the sample. This will be discussed further in the "Discussion" section.

Figure 3.7 shows the sample holder and how a sample is placed inside of it. The mechanism for securing the sample relies on applying pressure to the sample by the hammer, therefore, the sample is already under some pressure before stress measurements are performed. This can explain why there is a difference between the position of the point compared to when the sample is measured in the reference DLTS system where no additional force is needed to secure it in place. Therefore, the results obtained in the reference DLTS system were assumed to be the correct zero-stress results. However, the change in the final answers was less than the error margin.

In Figure 5.11 the Arrhenius plots of the E2 defect under 0.18 GPa and 0.00

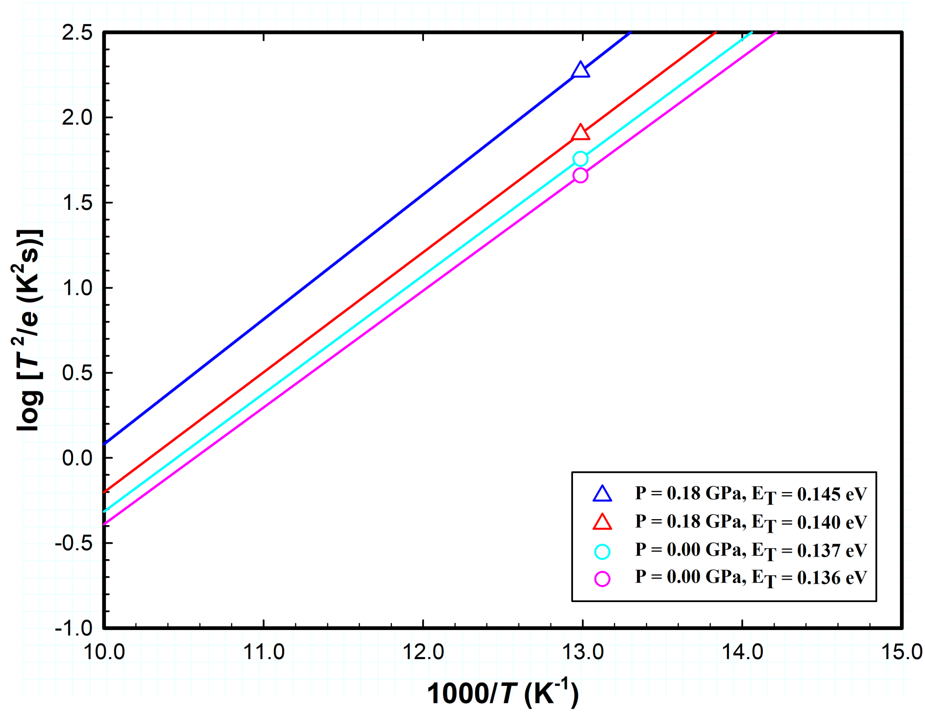

FIGURE 5.10: Arrhenius plot of the two components of the E2 defect under 0.18 GPa uniaxial stress along the [110] orientation. LDLTS measurement conditions: $V_R = -0.5$ V, filling pulse = +0.5 V, second pulse bias = −0.3 V, first and second pulse widths = 1 ms, sampling rate = 96 kHz, number of samples = 10000, number of scans = 3000. Emission rates under zero-stress conditions were measured using both the reference DLTS system (pink) and the stress DLTS system (cyan).

GPa, as measured by two systems, are shown. Here the values obtained for the activation energies of the two stress-induced components are different from the previous case where only single points were used. However, here the capture cross sections were calculated from the Arrhenius plot and as it can be seen in Table 5.3, while the values of the capture cross sections are of the same order of magnitude, they differ significantly from each other.

Figure 5.12 shows the case when the capture cross sections are all set to be 1.7×10^{-13} cm^2, the value obtained using the reference DLTS system. In this case, the activation energies are in close agreement with the previous case when only

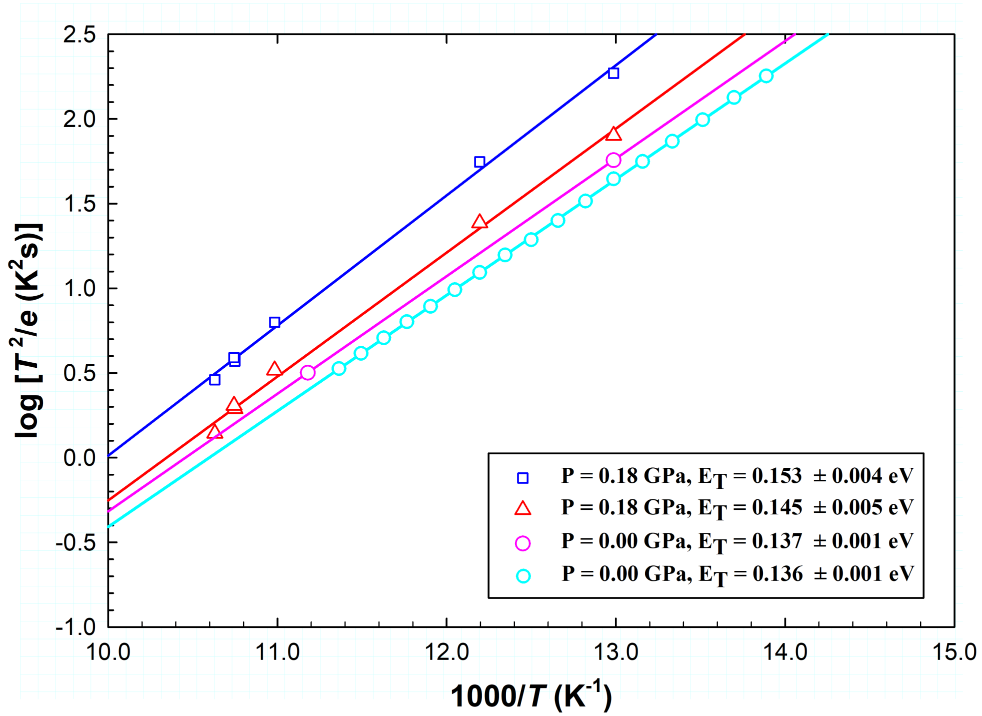

FIGURE 5.11: Arrhenius plot of the E2 defect under 0.18 GPa uniaxial stress along the [110] orientation. The plot shows the two components, $E2_a$ and $E2_b$, as well as measurements under zero stress from two different systems. LDLTS measurement conditions: $V_R = -0.5$ V, second pulse bias $= -0.3$ V, first and second pulse widths = 1 ms, sampling rate = 96 kHz, number of samples = 10000, number of scans = 3000.

the data points at 77 K were considered. However, the error associated with the current measurements are higher and can be attributed to less than ideal temperature stability during measurements.

Following the same approach, if σ is set to be 7.0×10^{-14}, which is the value reported by Hartnett and Palmer (1997), the energies decrease even more and the results can be seen in Table 5.4.

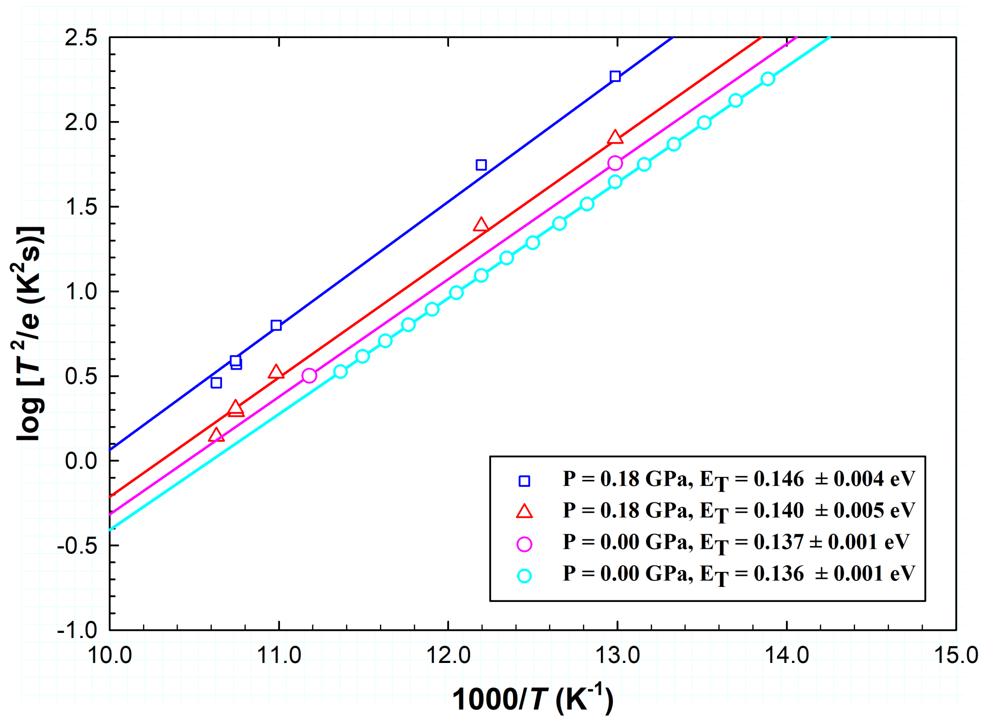

FIGURE 5.12: Arrhenius plot of the two components of the E2 defect under 0.18 GPa uniaxial stress along the [110] orientation. The capture cross sections were predetermined to be 1.7×10^{-13} cm^2. LDLTS measurement conditions: $V_R = -0.5$ V, second pulse bias $= -0.3$ V, first and second pulse widths $= 1$ ms, sampling rate $= 96$ kHz, number of samples $= 10000$, number of scans $= 3000$.

5.4.2 Discussion

From Figures 5.10, 5.11 and 5.12, it is evident that the emission rate of the E2 defect responds to high uniaxial stress by splitting into two components which is in agreement with the study by Hartnett and Palmer (1997).

In Figure 5.10, there is a difference in the value of the emission rate obtained by the two DLTS systems. The emission rate measured by the stress DLTS system shows a slightly higher value compared to the reference DLTS system for the unstressed sample. Since, it is very plausible to assume that the temperature difference between the two measurements was less than 1 K, the only possible reason would involve the sample being already under minute amounts of stress prior to measurements in the stress DLTS system.

As can be seen in Figure 3.7, The mechanism for securing the sample in the sample holder relies on applying pressure to it from both sides. While the mass of the hammer plus the amount of force needed to ensure the sample is stabilized is very small, it is likely that it is large enough to affect further measurements.

In order to test the validity of the previous statement, we can use Equation 5.1. Here, e_n is the emission rate of the defect as measured by the non-stress DLTS system and $e_n(P)$ is the corresponding value for the zero stress measurement in the stress DLTS system. Considering ideal temperature stability during these measurement, the values are: $T = 77$ K, $e_n = 130.068$ s^{-1} and $e_n(P) = 103.523$ s^{-1}. Therefore, $\Delta E = 0.001$ eV which is in agreement with the results from the Arrhenius plot in Figure 5.10. So, although the amount of initial stress (δP)

can vary from measurement to measurement, if the temperature is determined accurately, the initial conditions with regards to stress can be determined and accounted for without the need for direct measurements.

5.4.3 Activation energies and capture cross sections

Table 5.3 summarizes the results of our measurements as they were carried out by two DLTS systems. Here the E2* refers to the measurements under δP amount of stress. Table 5.4 summarizes the results of the study by Hartnett and Palmer (1997). From the two tables, it can be seen that there are differences between the two studies with regards to the values of the activation energies and the apparent capture cross sections.

In their study, under $P = 0.4$ GPa of uniaxial stress, the stress dependence of each component can be determined to be $\Delta E_a/P = 0.020 \pm 0.002$ eV.GPa^{-1} and $\Delta E_b/P = 0.050 \pm 0.002$ eV.GPa^{-1}. Where as in our study, from figure 5.11 for $P = 0.18$ GPa, the corresponding values are $\Delta E_a/P = 0.050 \pm 0.005$ eV.GPa^{-1} and $\Delta E_b/P = 0.085 \pm 0.004$ eV.GPa^{-1}. Furthermore, selecting E2* as the reference for calculating ΔE, the values are: $\Delta E_a/P = 0.044 \pm 0.005$ eV.GPa^{-1} and $\Delta E_b/P = 0.080 \pm 0.004$ eV.GPa^{-1}. These results are obtained under the assumption that the pressure dependence is linear and the two studies agree within the error margin.

In our measurements, while the capture cross sections of the two components of the stressed defect are of the same order of magnitude, they differ from each other

and the unstressed E2 defect as well as from the value reported by Hartnett and Palmer (1997). Given that the apparent capture cross sections were extracted from the Arrhenius plot in Figure 5.4, the error resulting from data fitting was taken into account showing that the uncertainty in the data recorded in the stress DLTS system is much larger than that recorded in the reference system. There was not sufficient evidence to show that the capture cross-sections of the two defects differ from each other or from the unstressed defect.

While uniaxial and hydrostatic stress can affect the pre-exponential factors in equation 2.13 by influencing the effective density of states (Londos and Pavelka, 1990), there are no established theories as to whether or not the capture cross section can be affected as well (Dobaczewski et al., 1995). Therefore, without direct measurement of the real capture cross section of the defect under uniaxial stress, definitive conclusions cannot be drawn. However, it seems common practice in many uniaxial and hydrostatic studies((Hartnett and Palmer, 1997) (Londos and Pavelka, 1990) (Dobaczewski et al., 1995)) to assume that the capture cross section is not stress dependent. In this respect, as a method for further analysis of our data, we proceeded to adopt the same methodology.

Table 5.5 summarizes the values obtained after assuming a fixed capture cross section. From the table, it is clear that when the capture cross section is selected to be 1.7×10^{-13} cm^2, $\Delta E_a/P = 0.022 \pm 0.003$ eV.GPa^{-1} and $\Delta E_b/P = 0.053 \pm 0.002$ eV.GPa^{-1}. Similarly, if the capture cross section is chosen to be 7.0×10^{-14} cm^2, $\Delta E_a/P = 0.028 \pm 0.003$ eV.GPa^{-1}, $\Delta E_b/P = 0.053 \pm 0.002$ eV.GPa^{-1}. It is believed that the most reliable results should be obtained when using the capture

cross section determined in the reference DLTS system, i.e. 1.7×10^{-13} cm^2 as this value was directly measured by us and therefore is the most justifiable value to use.

There is therefore no conclusive evidence that the capture cross section is significantly influenced by uniaxial stress.

TABLE 5.3: Summary of the results obtained by our stress DLTS system for the E2 defect.

Designation	Applied Stress (GPa)	E_T (eV)	σ_a (cm2)	Orientation	Irradiation Type	Irradiation Energy (MeV)	Irradiation Time (h)	Population (%)
E2	0.00	0.136±0.001	$1.7(\pm0.05)\times10^{-13}$	[110]	β	2.0	3.5	100
E2*	δP	0.137±0.001	$1.7(\pm0.05)\times10^{-13}$	[110]	β	2.0	3.5	100
E2a	0.18	0.145±0.005	$3.6(\pm 0.4)\times10^{-13}$	[110]	β	2.0	3.5	45.2 ± 0.2
E2b	0.18	0.152±0.004	$4.6(\pm 2.9)\times10^{-13}$	[110]	β	2.0	3.5	54.8 ± 0.5

Tables 5.3, 5.4 and 5.5 summarize the results obtained by our system compared with the results of the study conducted by Hartnett and Palmer (1997). Aside from the energy values and capture cross sections, the other difference between the two sets of data is the population associated with each stress induced component. Our data numerically falls within the margin of error of the values reported by Hartnett and Palmer (1997), however, they were obtained from the Transient

TABLE 5.4: Summary of the results obtained by Hartnett and Palmer (1997) for the E2 defect.

Designation	Applied Stress (GPa)	E_T (eV)	σ_a (cm2)	Orientation	Irradiation Type	Irradiation Energy (MeV)	Irradiation Time (h)	Population (%)
E2	0.0	0.140±0.002	7×10^{-14}	[110]	α	1.0	-	100
E2a	0.4	0.148±0.002	7×10^{-14}	[110]	α	1.0	-	50 ± 5
E2b	0.4	0.160±0.002	7×10^{-14}	[110]	α	1.0	-	50 ± 5

processor software. Since LDLTS has inherently higher resolution, we were able to obtain more accurate values.

As it can be seen in Table 5.3, the E2a and E2b do not have equal populations and the difference is greater than the error margins suggested by the Laplace inversion. The component with the lower DLTS activation energy (E2a) has a smaller population compared to the the one with higher DLTS activation energy (E2b). Hartnett and Palmer (1997) reported the populations as being 50 ± 5 for both components, our results therefore fall in their error margin. At first glance, a 1:1 ratio of the peaks would be expected, but the deviation may be explained by the defect reorienting itself towards the lower energy configuration. A more detailed study on reorientation energy of defects was done by Coutinho et al. (2003).

Assuming an energy difference ΔE_{orient} between the two orientations and that populations have reached equilibrium conditions, using Bolzmann distribution we

can calculate the difference in energy for both cases.

$$\frac{N_b}{N_a} = \exp\left(\frac{\Delta E_{orient}}{kT}\right) \tag{5.2}$$

Where N_a and N_b are populations for E2a and E2b respectively, k is the Bolzmann constant and T is the temperature.

Using the values presented in Table 5.3 for N_a and N_b for T = 77 K, a value of ΔE_{orient} of 0.001 eV is obtained.

TABLE 5.5: Summary of the results, comparing various cases where the capture cross sections are either predetermined or not as well as when the true initial energy level under δP stress level was used as the reference value for ΔE calculations.

σ_a (cm^2)	E_T (eV)				ΔE (eV)		P (GPa)	$\Delta E/P$ (eV/ GPa)	
σ_a	*E2*	*E2**	*E2a*	*E2b*	*ΔEa*	*ΔEb*	*P*	*Ea*	*Eb*
Variable	0.136±0.0001	0.138±0.001	0.145±0.005	0.152±0.004	0.009±0.005 0.008±0.005†	0.016±0.004 0.015±0.004†	0.18	0.050±0.005 0.044±0.005†	0.085±0.004 0.080±0.004†
1.7×10^{-13}	0.136±0.001	0.137±0.001	0.140±0.007	0.146±0.006	0.004±0.007 0.003±0.007†	0.010±0.006 0.009±0.006†	0.18	0.022±0.003 0.017±0.003†	0.053±0.002 0.048±0.002†
7.0×10^{-14}	0.129±0.001	0.131±0.002	0.134±0.003	0.139±0.002	0.005±0.003 0.003±0.003†	0.010±0.002 0.008±0.002†	0.18	0.028±0.003 0.017±0.003†	0.053±0.002 0.043±0.002†
†† 7.0×10^{-14}	0.140±0.002	----	0.148±0.002	0.160±0.002	0.008±0.002	0.020±0.002	0.40	0.020±0.002	0.050±0.002

† Results when E2* is chosen as the reference value for zero stress case.

†† The data obtained from Hartnett and Palmer

5.5 Shortcomings and sources of error

As is the case for any measurement techniques and instruments, there are shortcomings with regards to the scope of measurements that are achievable by this system. Also, due to high sensitivity of LDLTS, sources of error can have considerable effects on the accuracy of the acquired data.

5.5.1 Sources of error

The major source of error in our measurements was temperature stability. Since emission rate of a defect is temperature dependent, factors that affect accurate temperature stabilization and reading can contribute towards errors in measurements. These factors include:

- Thermal conductivity of the materials used for the construction of the sample holder that affects heat transfer between the sample and the cold junction. Due to mechanical considerations, the sample holder and its constituents were made from stainless steel which at low temperatures is not a good thermal conductor.

- The measurement error associated with the chromel Au/Fe(0.007) thermocouple that was used in this project was calculated to be as high as ± 2.9 K.

- There are issues with temperature stabilization when the system operates close to the lowest temperature limit of the system. In this case, the minimum achievable temperature was 77 K.

- Another contributing factor to the temperature stability issue is that the contact surfaces between the sample and the sample holder are very small. Also, Since the sample is vertically balanced and only makes limited contact with the hammer and the anvil, depending on the distance of the SBD under study from the contacting surfaces, heat transfer can be affected even more.

- Finally, in section 5.4.3, the effects of the sample being pre-stressed on measurements was discussed. This phenomena is a result of the mounting process and the overall design of the sample holder.

To address these issues, one possible solution is to redesign the sample holder to ensure optimum heat transfer to and from the sample as well as eliminate the possibility of pre-stressing the sample. Figure 5.13 shows a schematic of an optimized sample holder. From the figure it can be seen that there are major differences between the previous model and the new sample holder. These changes include:

- The new sample holder contains a two part copper core that makes contact with the heat exchanger of a cryostat at the bottom and is responsible for transferring heat between the cryostat and the sample.

- The design of the hammer and the anvil are completely different from the previous model. This was done to provide better access to the sample as well as make loading samples easier and faster.

- In this model, the Ohmic side of the sample is able to make contact with the copper core for more efficient heat transfer and is electrically isolated from the core using a sapphire piece. The positive pressure from a spring loaded probe on the SBD side of the sample (not included in the figure) will ensure continuous contact between the sample and the sapphire piece.

- Since, in the new design, there is more free space around the sample, it will be possible to use different types of temperature sensors whereas previously the options were limited to thin thermocouple wires.

- The fact that in the new design the two stress inducing surfaces are not utilized to secure the sample in place, provides that there will be no stress applied to the sample other than the amount applied by the hydraulic cylinder. Hence, eliminating the effects of pre-stress associated with the current sample holder.

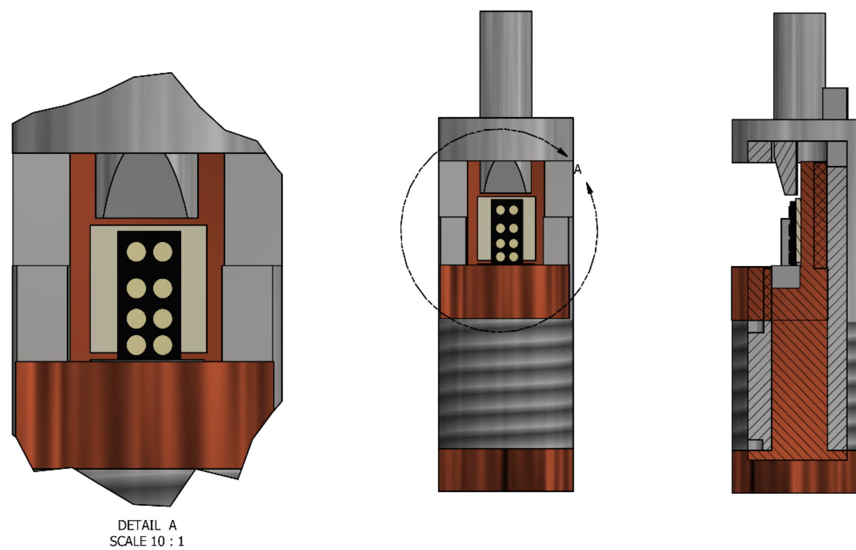

FIGURE 5.13: Schematic illustration of an optimized sample holder. The design incorporates a stainless steel outer shell to ensure stability under high pressure while a copper core and contact surface is used to improve heat transfer to the sample.

5.5.2 Shortcomings

- One measurement limiting factor is the temperature range. Since it was more practical to use a top loading cryostat and the only available one was a liquid nitrogen-cooled system, the minimum temperatures at which measurements can take place is limited to 77 K . This can be considered a significant shortcoming of this system as many important and recently discovered defects in Si, Ge and GaAs are only observable at lower temperatures.

  This can be addressed by using commercially available, top loading, liquid helium or helium-cycle cryostats.

- Another shortcoming of the system lies with the nature of stress dependent measurements. Every material has a specific range of elasticity which determines how much the material can be stressed or strained before permanent deformation or breakage occurs. In the case of stress dependent studies, This factor limits the maximum amount of stress that can be applied to the sample. Therefore, limiting characterization to the defects whose stress-dependent change in emission rate falls within the measurable range of LDLTS.

- Another shortcoming of the system comes from what is known as ”fatigue limit” of a material. When a single sample undergoes multiple stress dependent measurements at maximum possible amounts of stress, over time, the sample can permanently deform. This deformation affects the crystalline structure of the solid, therefore altering the structure (and other properties)

of most of the defects in the sample. This means that the accuracy of measurements will progressively lower after multiple cycles as the defect under study can be in a different configuration relative to its original state. This can be a major contributor towards obtaining false or inaccurate data.

The simplest method to overcome this issue is to avoid using a single sample for characterizing different defects, thus preventing the sample from going through too many stress cycles. However, when using multiple samples, it is important to consider:

1. It is more favourable to make samples out of a single wafer.
2. Samples must be identical with regards to their physical properties (dimensions, angles of edges, ...).
3. When a single sample is used for multiple measurements, post stress effects must be studied and accounted for in subsequent measurements.

Another possible solution is to avoid stressing the samples to the maximum possible levels but rather relying on the high resolution of the LDLTS to characterize samples at lower stress levels.

Finally, samples can be annealed at appropriate temperatures in order to restore their crystalline structure. However, this process can also result in elimination of the defect centres as well. Therefore, re-introduction of defects may be required after each annealing.

Chapter 6

Summary and conclusions

In summary, the goal of this project, which was to design and build a working uniaxial-stress LDLTS system, was achieved. As was discussed in Chapter 3, The mechanical portion of the system consists of custom-made as well as commercially available components and it was developed to be compatible with an Oxford Instruments' OptistatDN liquid nitrogen cooled cryostat. The appropriate amount of stress is applied to the sample through a hydraulic cylinder and the pressure can be adjusted and controlled using a manual hydraulic pump and a force sensor. The hydraulics allow for a considerable range of pressures to be applied to the sample and allow the sample to remain under stress for long periods of time while high resolution LDLTS measurements are being performed.

In Chapter 5, the first set of measurements under uniaxial stress of up to 0.18 GPa was performed and the results were presented.

The functionality of the system was investigated by replicating some of the results obtained in a similar study regarding the E2 defect in GaAs by Hartnett and Palmer (1997). It was shown that the system operates as designed with only difficulty being temperature stabilization at low temperatures. However, it can be concluded that the results agree qualitatively as well as quantitatively with the those presented by Hartnett and Palmer (1997).

In our study, we showed that under $P = 0.18$ GPa of force applied along the [110] axes results in splitting of the emission rate spectra of the E2 defect into two components. The energy difference between the two components at $T =$ 77 K, was measured to be $E2b - E2a = 0.007$ eV. It was also shown that for the two components $\Delta E2a/P = 0.022\pm$ 0.003 eV.GPa^{-1} and $\Delta E2b/P = 0.053\pm0.002$ eV.GPa^{-1} as well as $\Delta E2a/P = 0.017 \pm 0.003$ eV.GPa^{-1} and $\Delta E2b/P = 0.048 \pm 0.002$ eV.GPa^{-1}, when the pre-stress effects of mounting the sample were considered. In both cases the results are in agreement with those reported by Hartnett and Palmer (1997).

It was also established that although the capture cross sections of the two components differ from one another when determined from the Arrhenius plot in Figure 5.10, the uncertainty in the recorded data by the stress DLTS system was too great to allow for accurate conclusions.

Also, in our study the higher resolution of LDLTS resulted in more accurate determination of the populations associated with the stress-induced components of the E2 defect. We showed that the populations are not identical and this difference may be the result of reorientation of some of the defects under stress.

Subsequently, using Bolzmann distribution, we determined the $\Delta E_{orient} = 0.001$ eV.

Furthermore, although our system is capable of applying very high uniaxial stress, due to high resolution of LDLTS (as opposed to conventional DLTS which was used Hartnett and Palmer (1997) study), the same observations were made at lower pressures and without damaging the sample. Therefore it can be concluded that our system can be used to study stress induced effects in softer materials as well as conventional semiconductors.

6.1 Future work

As the first step in improving the performance of the system, it will be necessary to address the temperature stabilization issues. The new design for the sample holder that was discussed in Section 5.4.3, would be a suitable solution for this problem and therefore, implementing it into the system will be the first step in undertaking future measurements using the system.

Also, it will be beneficial to be able to use the system in conjunction with a helium-cycle cryostat, similar to the one used in this work as the reference system, in order to be able to perform measurements over a wider range of temperatures. However, with the current temperature range of the system, it already allows for characterization of numerous defects in a number of semiconductor materials which will provide experimental proof for various identities that are theoretically proposed for these defects.

Once the temperature stabilization is properly addressed, The next step will be to acquire suitable samples so that stress measurements can be performed from various orientations. For this purpose, ideal samples must be extracted from a wafer with [110] surface orientation from which the other two major orientations can be extracted. This will allow for proper identification experiments for determining the configuration and the structure of defects which is the primary reason for developing the stress DLTS system.

Furthermore,an interesting experiments would be to experiment on the dependence of the capture cross section of defects on the applied stress. This can be achieved using the stress system along with a fast pulse interface that would be able to apply very short filling pulses to the sample in order to determine the true capture cross sections as the sample is stressed. Other future research ideas are numerical modelling and population studies.

Bibliography

Ashcroft, N. W. and Mermin, N. D. (1976). *Solid State Physics*. Holt, Rinehart and Winston. https://books.google.com/books?id=1C9HAQAAIAAJ{&}pgis=1

Auret, F. D., Goodman, S. A., Myburg, G., and Meyer, W. E. (1993). Electrical characterization of defects introduced in n-GaAs by alpha and beta irradiation from radionuclides. *Applied Physics A Solids and Surfaces*, 56(6):547–553.

Baca, A., Ren, F., Zolper, J., Briggs, R., and Pearton, S. (1997). A survey of ohmic contacts to III-V compound semiconductors. *Thin Solid Films*, 308-309:599–606.

Coutinho, J., Andersen, O., Dobaczewski, L., Bonde Nielsen, K., Peaker, A. R., Jones, R., Öberg, S., and Briddon, P. R. (2003). Effect of stress on the energy levels of the vacancy-oxygen-hydrogen complex in Si. *Physical Review B*, 68(18):184106.

Cutler, M. and Mott, N. F. (1969). Observation of anderson localization in an electron gas. *Phys. Rev.*, 181:1336–1340.

Dobaczewski, L., Hawkins, I. D., and Peaker, A. R. (1995). Laplace transform deep level transient spectroscopy: new insight into defect microscopy. *Materials Science and Technology*, 11(10):1071–1073.

Dobaczewski, L., Kaczor, P., Hawkins, I. D., and Peaker, A. R. (1994). Laplace transform deep-level transient spectroscopic studies of defects in semiconductors. *Journal of Applied Physics*, 76(1):194.

Dobaczewski, L., Peaker, A. R., and Bonde Nielsen, K. (2004). Laplace-transform deep-level spectroscopy: The technique and its applications to the study of point defects in semiconductors. *Journal of Applied Physics*, 96(9):4689–4728.

Giacovazzo, C. (2002). *Fundamentals of Crystallography*. Oxford University Press. https://books.google.com/books?id=77pUdgxcar0C&pgis=1

Grove, A. (1967). *Physics and Technology of Semiconductor Devices*. John Wiley and sons, 1st edition edition. https://books.google.com/books?id=77pUdgxcar0C/&pgis=1

Hartnett, S. and Palmer, D. (1997). Uniaxial-stress symmetry studies on the e1, e2 and e3 irradiation-induced defects in gallium arsenide. In *Defects in Semiconductors 19*, volume 258 of *Materials Science Forum*, pages 1027–1032. Trans Tech Publications.

Kaplyanskii, A. A. (1967). Noncubic centers in cubic crystals and their spectra in external fields. *Le Journal de Physique Colloques*, 28(C4):C4–39–C4–48.

Kittel, C. (2004). *Introduction to Solid State Physics*, volume 11. Wiley, https://books.google.com/books?id=kym4QgAACAAJ&pgis=1.

Lang, D. V. (1974). Deep-level transient spectroscopy: A new method to characterize traps in semiconductors. *Journal of Applied Physics*, 45(7):3023.

Londos, C. A. and Pavelka, T. (1990). DLTS investigation of deep levels in bulk gaas under uniaxial stress. *Semiconductor Science and Technology*, 5(11):1100.

Łukasiak, L. and Jakubowski, A. (2010). History of semiconductors. *Journal of Telecommunications and information technology*, pages 3–9.

McCluskey, M. D. and Haller, E. E. (2012). *Dopants and Defects in Semiconductors*. CRC Press. https://books.google.com/books?id=fV8k6YMxf-MC{&}pgis=1

McGuigan, K. G., McGlynn, E., O'Cairbre, F., Love, J., and Henry, M. O. (2000). Piezo-spectroscopic induced perturbations for defects in cubic crystals under uniaxial stress applied along arbitrary low-symmetry crystal directions. *Journal of Physics: Condensed Matter*, 12(31):7055–7068.

Meyer, W. E. (2006). Digital DLTS studies on radiation induced defects in Si, GaAs and GaN. (Ph.D Thesis, University of Pretoria).

Miller, G. L., Lang, D. V., and Kimerling, L. C. (1977). Capacitance transient spectroscopy. *Annual Review of Materials Science*, 7(1):377–448.

Pons, D. and Bourgoin, J. C. (1985). Irradiation-induced defects in GaAs. *Journal of Physics C: Solid State Physics*, 18(20):3839–3871.

Sarkar, T., Mailloux, R., Oliner, A. A., Salazar-Palma, M., and Sengupta, D. L. (2006). History of wireless. Hoboken. https://books.google.co.za/books?id=NBLEAA6QKYkC&printsec=frontcover&dq=History+of+Wireless&hl=en&sa=X&ved=0ahUKEwiQlcu8zL_eAhVCLMAKHfmGAOkQ6AEIKTAA#v=onepage&q=History

Schroder, D. (2006). *Semiconductor Material and Device Characterization*. Wiley - IEEE. Wiley. https://books.google.co.za/books?id=OX2cHKJWCKgC

Seebauer, E. G. and Kratzer, M. C. (2008). *Charged Semiconductor Defects: Structure, Thermodynamics and Diffusion*. Springer Science & Business Media.

Smith, Z. A. and Taylor, K. D. (2008). *Renewable and alternative energy resources: a reference handbook*. ABC-CLIO. https://books.google.co.za/books?id=OlA-fN3Bd4QC&lpg=PP1&dq=Renewable

Streetman,B.(1994). *Solid State Electronic Devices*. Prentice-Hall international editions. Prentice-Hall. https://books.google.co.za/books?id=VmnDQwAACAAJ

Sze, S. and Ng, K. (2006). *Physics of Semiconductor Devices*. Wiley. https://books.google.co.za/books?id=o4unkmHBHb8C

Zallen, R. (2008). *The Physics of Amorphous Solids*. Physics textbook. Wiley. https://books.google.co.za/books?id=fHoJn0P_XwYC

Zettili, N. (2009). *Quantum Mechanics: Concepts and Applications*. Wiley. https://books.google.co.za/books?id=6jXlpJCSz98C